Aluminium based micro mirrors exposed to UV laser light – in situ performance and degradation

Von der Fakultät für Mathematik, Naturwissenschaften und Informatik
der Brandenburgischen Technischen Universität Cottbus
zur Erlangung des akademischen Grades
Doktor der Ingenieurwissenschaften
(Dr.-Ing.)
genehmigte Dissertation
vorgelegt von

Dipl. Ing.(FH), M. Eng.
Alexander Mai

geboren am 08. März 1980 in Altdöbern

Gutachter: Prof. Dr. Harald Schenk
Gutachter: Prof. Dr. Dieter Schmeißer
Gutachter: Prof. Dr. Hubert Lakner

Tag der mündlichen Prüfung: 12.09.2014

Abstract

The present thesis characterises aluminium based micro mirrors exposed to UV laser light. Such micro mirrors, used in highly integrated spatial light modulators, can for example be used as programmable masks in DUV micro lithography. Therefore they are sensitive to any performance loss arising from material degradation or changes in the mirror curvature. The key question addressed in this thesis is the investigation of the in situ curvature change, which means characterisation during a real laser irradiation. For this purpose a measuring station was designed, combining a phase-shift interferometer, an optical microscope and the laser irradiation of the sample at 248nm. The Phase-shift interferometry technique used is a very sensitive contactless optical measurement principle, which allows a resolution of the sample surface in the single-digit nanometer range.

A multitude of irradiation tests were performed to describe the change of mirror curvature as a function of different irradiation parameters such as the pulse energy, the laser repetition rate or the ambient atmosphere. The most significant effect was detected by the variation of the applied pulse energy, which was in the range of 10^{-5}J/cm^2 to 10^{-2}J/cm^2. A general conclusion was that a minimum energy of 10^{-5}J/cm^2 at a repetition rate of 1kHz is required to detect any laser induced change of the mirror curvature. At higher energy levels two characteristic behaviours can be distinguished. Up to a level of 10^{-3}J/cm^2 the mirrors show a permanent concave bowing in the range of λ/100. A further increase of the pulse energy causes an accumulating bowing in the opposite direction (convex) of λ/10 within some ten million laser pulses. However this convex bowing partially relaxes after the irradiation is stopped.

Another aspect of the thesis was the determination of laser induced material degradation. For this purpose irradiated mirrors were investigated by means of different devices and analytical techniques such as atomic force microscopy (AFM), reflectometry and transmission electron microscopy (TEM). The AFM analysis showed a slight increase of surface roughness and a directional change of the grain size. As a result of the TEM analysis it turned out that arrangement and shape of the grains seems not to have changed. But after the irradiation the growth of a porous oxide layer up to 20nm on the upper mirror surface was noticed.

Finally different hypotheses are proposed to explain the mechanisms behind the observed concave and convex bowing at particular pulse energies. In this connection it is assumed that the mirrors at pulse energies larger than 10^{-3}J/cm^2 do not show a static bowing at all. It is rather assumed that the mirror bow oscillates with the laser repetition rate.

Zusammenfassung

Die vorliegende Arbeit behandelt die Charakterisierung Aluminium-basierter Mikrospiegel unter UV-Laserbestrahlung. Eben solche Mikrospiegel werden in hochintegrierten räumlichen Lichtmodulatoren verwendet und z.B. als programmierbare Masken in der DUV- Mikrolithographie eingesetzt. Entsprechend empfindlich verhalten sie sich gegenüber Verlusten ihrer Funktionseigenschaften z.B. durch Degradation des Spiegelmaterials oder Änderungen der Spiegeltopographie. Die Kernfrage dieser Arbeit ist die Untersuchung der in situ Krümmungsänderung unter Laserbestrahlung. Zu diesem Zweck wurde ein Messplatz entworfen. Dieser kombiniert ein phasenschiebendes Interferometer (PSI) mit optischem Mikroskop und Laserbestrahlung bei 248nm. PSI ist ein sehr empfindliches optisches Messprinzip und ermöglicht die Auflösung der untersuchten Oberfläche im einstelligen Nanometerbereich.

Eine Vielzahl von Bestrahlungstests wurde durchgeführt, um die Krümmungsänderung der Spiegel in Abhängigkeit verschiedener Bestrahlungsparameter zu untersuchen. Der größte Effekt wurde bei der Variation der Laserpulsenergie (im Bereich 10^{-5}J/cm^2-10^{-2}J/cm^2) beobachtet. Hierbei hat sich gezeigt, das erste Änderungen der Krümmung bei Werten von 10^{-5}J/cm^2 detektiert wurden. Bei höheren Pulsenergien können zwei typische Verhaltensweisen unterschieden werden. Bis zu 10^{-3}J/cm^2 zeigen die Spiegel eine permanente konkave Krümmungsänderung von λ/100. Die weitere Erhöhung der Pulsenergie führt jedoch zu einer Änderung in entgegengesetzter Richtung (konvex). Diese summiert sich innerhalb einiger 10 Millionen Pulse zu Werten von λ/10 auf. Außerdem zeigt diese konvexe Krümmungsänderung eine teilweise Relaxation nach Beendigung der Bestrahlung.

Ein weiterer Aspekt der Arbeit war die Bestimmung möglicher laserinduzierter Alterung des Spiegelmaterials. Zu diesem Zweck sind bestrahlte und unbestrahlte Spiegel mittels verschiedener analytischer Techniken untersucht worden. Hierzu gehörten die Rasterkraftmikroskopie (AFM), die Reflektometrie und die Transmissionselektronenmikroskopie (TEM). Die AFM Messungen zeigten eine geringfügige Erhöhung der Oberflächenrauheit und eine richtungsabhängige Änderung der Korngröße. Die TEM Analysen haben gezeigt, dass sowohl Anordnung und Form der Körner keine deutliche Änderung aufweisen. Jedoch wurde bei bestrahlten Proben eine porösen Oxidschicht von bis zu 20nm auf der oberen Spiegelfläche detektiert.

Abschließend wurden verschiedene Hypothesen aufgestellt, um die Mechanismen der beobachteten konkaven und konvexen Krümmungsänderung zu erklären. In diesem Zusammenhang wird angenommen, dass Spiegel bei Pulsenergien oberhalb 10^{-3}J/cm^2 an sich keine statische Verkrümmung aufweisen. Vieles spricht für eine dynamische Änderung (Oszillation) der Krümmung mit der Laserwiederholrate.

List of Abbreviations

AFM	-	Atomic force microscope
BF	-	bright field (modus)
CCD	-	Charge-coupled Device
CMOS	-	Complementary metal–oxide–semiconductor
cw (mode)	-	continuous wave (laser mode)
DF	-	dark field (modus)
DLPTM	-	Digital Light Processing
DMDTM	-	Digital Micromirror Device
DRAM	-	Dynamic Random Access Memory
DUV	-	Deep ultra violet
EDX	-	Energy-dispersive X-ray spectroscopy
FIB	-	Focused ion beam
FWHM	-	Full width half maximum
LMIS	-	Liquid metal ion source
MEMS	-	Micro-electro-mechanical-systems
MOEMS	-	Micro-opto-electro-mechanical-systems
NIR	-	Near infrared spectral region (~780nm – 2500nm)
OPD	-	Optical path difference
PSI	-	Phase shift interferometry
SEM	-	Scanning electron microscope
SLM	-	Spatial light modulator
SRAM	-	Static random-access memory
VIS	-	Visible spectral region (~380nm – 780nm)
VOA	-	Variable optical attenuator
wd	-	working distance
TEM	-	Transmission electron microscopy
UV	-	ultra violet

Formula symbols

			unit
a	-	grating pitch/ mirror pitch	m
a	-	mirror edge length in x	m
A	-	absorption of an optical media	-
A_{th}	-	cross section of a heat conducting element	m^2
$A'_{ill.}$	-	aperture of the illuminating device	-
$A_{imag.}$	-	aperture of the imaging device	-
b	-	mirror edge length in y	m
B	-	bending stiffness for an undamped plate	Nm
c	-	specific heat capacity	J/(K*kg)
C	-	electric capacitance	A*s/V
C_{th}	-	thermal capacitance/ thermal mass	J/K
d	-	diameter	m
d_n	-	nominal mirror tilt	m
D_s	-	laser spot diameter	m
E	-	Young's modulus	N/m^2
$f'_{col.}$	-	focal distance of the collimation lens	m
$f'_{obj.}$	-	focal distance of the objective	m
f'_F	-	focal distance of the Fourier lens	m
$f_{m,n}$	-	eigenfrequency of an undamped plate	1/s
f'_p	-	focal distance of the projection lens	m
f'_{tl}	-	focal distance of the tube lens	m
h	-	sample thickness	m
H(x, y)	-	surface height (x, y)	m
ΔH_{min}	-	minimum step height of the interferometer	m
ΔH_{max}	-	maximum allowed step height of the interferometer	m
HH'	-	position of the principal planes	-
l	-	length of a heat conducting element	m
I_0	-	laser intensity	W/m^2

I_0	-	incident intensity	-
I_r	-	reflected intensity	-
k	-	extinction coefficient = imaginary part of the complex index of refraction	-
k_T	-	thermal conductivity	W/(K*m)
l_{th}	-	thermal diffusion depth	m
m	-	order of the diffraction maxima	-
m	-	slope	-
m	-	eigenfunction/ mode in x	-
n	-	complex index of refraction	-
n	-	real part of the complex index of refraction	-
n	-	number of reflections (heat wave on sample boundaries)	-
n	-	eigenfunction/ mode in y	-
NA	-	numerical aperture	-
$NA_{im.}$	-	numerical aperture of the imaging beam path	-
$NA_{ill.}$	-	numerical aperture of the illuminating beam path	-
Q	-	charge	As
R	-	ohmic resistance	V/A
R	-	reflectance	-
Ra	-	surface roughness - arithmetic average of detected data	m
Rq	-	surface roughness - root mean square of detected data	m
Rmax	-	surface roughness - maximum value of detected data	m
R_{th}	-	thermal resistance	K/W
t	-	time	s
t_r	-	rise time	s
T	-	temperature	K
ΔT	-	thermal gradient	K
T_0	-	initial temperature	K
U	-	voltage	V
U_0	-	detected voltage at room temperature	V
U_T	-	detected voltage at particular temperature	V
$\dot{W}$	-	heat source inside the sample	W
z	-	(sample) observation depth	m

α	-	absorption coefficient	1/m
γ	-	incidence angle on the single mirror	°
$\Gamma_M^{'}$	-	total magnification of the optical microscope	-
φ	-	phase shift between object and reference beam	-
$\varphi(x,y)$		wavefront phase	modulo 2π
$\Delta\varphi$	-	phase-shift between different fringe patterns	-
θ	-	incidence angle of measuring beam path	°
θ’	-	reflection angle of measuring beam path	°
ϑ	-	temperature	°C
κ	-	absorption index	-
κ_{th}	-	thermal diffusivity	m^2/s
λ	-	optical wavelength	m
μ	-	Poisson’s number	-
ρ	-	density	kg/m^3
ρ	-	reflectance	-
τ	-	time constant of exponential decay	s
τ	-	falling time	s
τ_p	-	laser pulse duration	s
Φ_e	-	radiant flux	W
ω_p	-	plasma frequency	1/s

1 Introduction

1.1 Motivation

The integration of micro-optics with micro-electro-mechanical systems (MEMS) created a new field of microsystems, termed Micro-opto-electro-mechanical-systems (MOEMS). The fundamental types of light manipulation either by reflection, refraction or diffraction result in the rough classification of micro optic actuators in micro mirror devices, tunable lenses und gratings. Based on these fundamental types of actuators it is possible to design very complex and sophisticated devices e.g. in the field of fibre-optical networking. Other relevant applications are projectors and light modulators based on highly integrated micro mirror devices or micro scanners [1].

The Fraunhofer IPMS develops arrays of tiltable micro mirrors which are e.g. used as spatial light modulators (SLMs) for pattern generation in DUV micro lithography [2, 3]. The present thesis is about the characterization of SLMs during an exposure with UV laser light. The characterization of MEMS and MOEMS generally contains a complex procedure of performance and durability tests. Irradiation tests with excimer lasers that last the whole lifetime of such devices are very expensive. For this reason, the duration of the performed irradiation tests within this thesis was limited to a fraction of the intended lifetime. Hence the investigations were rather focused on performance than on lifetime tests. Performance and reliability of a SLM contains different parameters like the stability or drift of the headed displacement angle, the mirror topography including the mirror curvature (bow) and roughness and the degradation of mirror, actuator and underlying electronics. The experiments were focused on the investigation of the effect of UV laser light on the micro mirror topography. The thesis' main objective was the investigation of the single mirror bow change induced by the laser exposure. Furthermore it was aimed to identify degradation mechanisms responsible for the observed in situ bow change.

The flatness of each single mirror is amongst others a characteristic property of a SLM. Due to its effect on image resolution and contrast of the generated patterns it is a property of major interest. The performed experiment is especially interesting for new applications requiring a laser fluence of some ten mJ/cm^2. In the past experimental investigations of SLM topography under laser exposure have been carried out in a separate step following the exposure [4]. But

depending on the delay between irradiation of the sample and detection of the topography occasionally there was a significant uncertainty in the detected data. From this it followed a fundamental requirement on the thesis, to do the characterization during a real laser irradiation. The new approach of an in situ measurement allows an inspection of the SLM simultaneously to its normal operation. Furthermore the experiment enables a better way to investigate the effect of different parameters (such as laser fluence, laser wavelength, laser repetition rate and purging gas) on the single mirror topography. It needs to be mentioned that all samples which were irradiated during this thesis have never been designed for such intense demands. Especially the applied energy level was orders of magnitudes higher than the initially intended application. The intense load on the sample were chosen to activate an obvious sample reaction and to investigate possible limitations of new applications.

The characterization of MEMS is a very complex field. Therefor the thesis includes diverse topics of partially different scientific fields:

- MEMS and laser induced degradation in general
- Interaction of laser light with metal
- Key question: laser induced change of the mirror topography
- Design of an appropriate measurement station
- Investigation of the bow change at varying irradiation parameters
- Investigation of laser induced degradation and damage

This mixture of issues finally resulted in a separation of the thesis in the following 5 topics:

Chapter 1: SLM – introduction

Chapter 1 introduces the SLM technology, the imaging principle and the motivation of the in situ bow measurement. Furthermore an inside into the topics of radiation induced degradation effects of micro optical devices and the interaction of laser light with metals is provided.

Chapter 2: Design and characterization of the phase-shift interferometer

At the beginning of this topic requirements and boundary conditions on the measurement principle are defined. Different measurement principles are discussed and the decision for a certain principle is made. In a next step a measurement station is designed which combines a

phase-shift interferometer, an optical microscope and the laser exposure of the sample. Finally the interferometer is characterized and the measurement error is discussed in detail.

Chapter 3: Laser irradiation of SLMs at 248nm

In chapter 3 irradiation tests are carried out and the resulting single mirror bow change is detected. This procedure includes a multitude of tests to get an idea of the general device behaviour at different laser fluences. Furthermore the effect of different laser parameters on the bow change is investigated.

Chapter 4: Investigation of laser-induced degradation

In chapter 4 the possible UV-laser induced degradation of the aluminium based mirror material is investigated. For this purpose irradiated mirrors and samples with an unstructured layer of the mirror material are investigated by means of different Micro- and Nano-analytical techniques such as AFM, reflectometry and TEM.

Chapter 5: Discussion of the observed bow change and degradation mechanisms

In chapter 5 the fundamentally observed device behaviour is discussed. Here the discussion distinguishes between the bow change during and after the laser exposure and tries to identify the physical mechanisms responsible for the particular behaviour at lower and higher laser fluences.

1.2 Spatial light modulators

A SLM is a device which provides a space-resolved modulation of intensity or phase of the incident light. Within the domain of SLM – technology there are different criteria that distinguish fundamental types of devices. A first distinction is e.g. made between passive and active devices. Both cases allow an independent control of each pixel. But passive devices use a fixed wiring between each pixel and the external supply electronics. Therefore they are limited in the number of logical pixels due to the number of bonds that can be placed on the device. Active devices allow the arrangement of several million logical pixels on one chip but require a sophisticated integration of a CMOS circuitry for each pixel, see e.g. [2], [5]. Other categories are related to the type of the element deflection with tilting mirrors on the one and piston-type mirrors on the other hand (see fig. 1). In addition, devices are distinguished in groups with either digital or analog deflection [6].

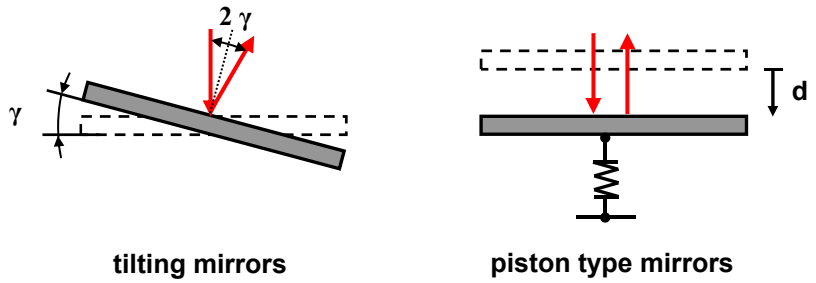

Fig. 1: SLMs -fundamental types of deflection a) tilting mirrors and b) piston type mirrors

1.2.1 Development of the light modulator technology

Starting in 1977 Texas Instruments developed a spatial light modulating technology evolving to a bi-stable or digital micro mirror device in 1987 [7]. The device is an optical MEMS consisting of thousands of tiltable micro mirrors, individually controlled by underlying CMOS electronics. Currently the mirrors can be deflected either to a +12° or -12° position, depending on the binary state of the SRAM cell underneath. According to this, light is either guided to an absorber or participates in the imaging process. Levels of gray are realized by varying the deflection time of a certain pixel during the refresh cycle of the entire matrix. The pixel architecture of the Digital Micromirror Device (DMD™) from 1997 is presented in fig. 2 and

shows the separation of the optical (mirror) from the mechanical plane (yoke and torsion flexures) which are connected with a post. First of all, the DMD™ is used in digital projection display systems. But there are several other applications e.g. in optical metrology, lithography, fibre optical networking or spectroscopy [7].

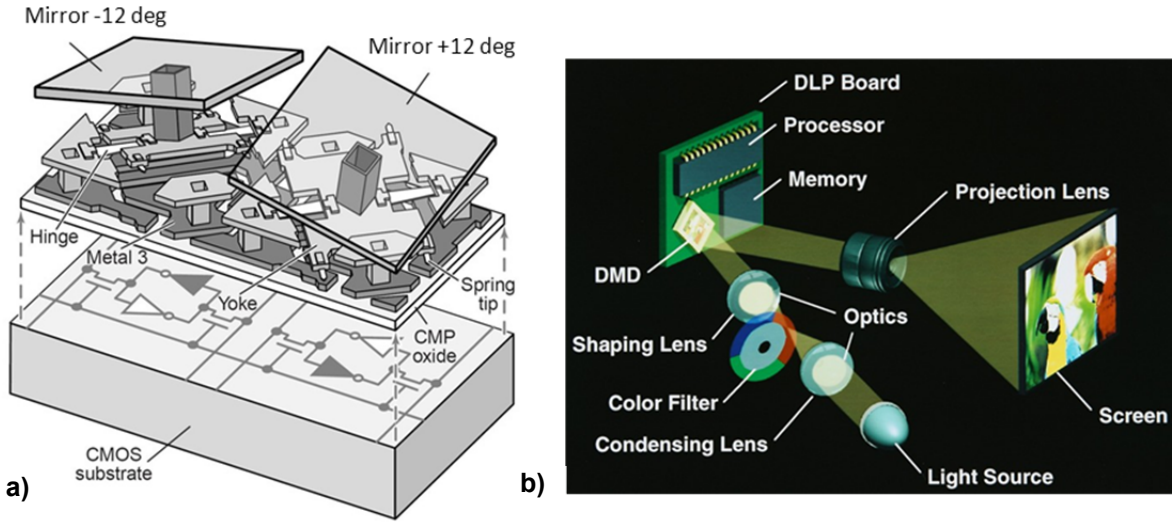

Fig. 2: a) Pixel architecture of the Digital Micromirror Device (DMD™) in the late 1990s [8], b) configuration of the DLP Projection system: white light source, shaping optics, rotating color filter, the DMD™ and a projection lens [9]

1.2.2 IPMS-SLM based on arrays of piston-type mirrors

Spatial light modulators based on arrays of piston type mirrors allow a pure phase modulation of the incident wave front. The space-resolved modulation of the optical path length is realized by an electrostatically actuated piston-like deflection of the mirror plates. Typically applications are herewith in the area of adaptive optics e.g. in ophthalmology, microscopy or astronomy where a correction of the imaging wave front is useful.

The wavefront correction in a telescope for the purpose of resolution improvement is shown schematically in fig.3. A telescope collects the light coming from a celestial body. Wave front distortions generated by turbulences or irregularities in the atmosphere are corrected by an adaptive optics device e.g. a deformable mirror or a piston-type mirror array. For this purpose the light is send to a wave front sensor (often using the the Shack-Hartmann principle) and the aberrations are detected in real-time. A PC converts the aberrations into an appropriate deflec-

tion of the mirror device. The distorted wave front is corrected in a feedback loop also in real-time. For determination of the optical aberrations the wave front sensor either analysis the light from the observed celestial body itself or from a so-called guide star which needs to be situated close to the observed object. Small objects are considered as point sources and the wave front distortion is identified by the analyse of the object's point spread function. Also possible is the generation of an artificial guide star by laser light (laser guide star). The corrected wave front is finally send to an image detector and the object is observed in higher contrast and resolution [71, 72].

Further applications of piston-type mirror arrays are laser pulse shaping including a modification of the pulse shape, reduction of the pulse length or the generation of pulse trains. [10, 11, 6].

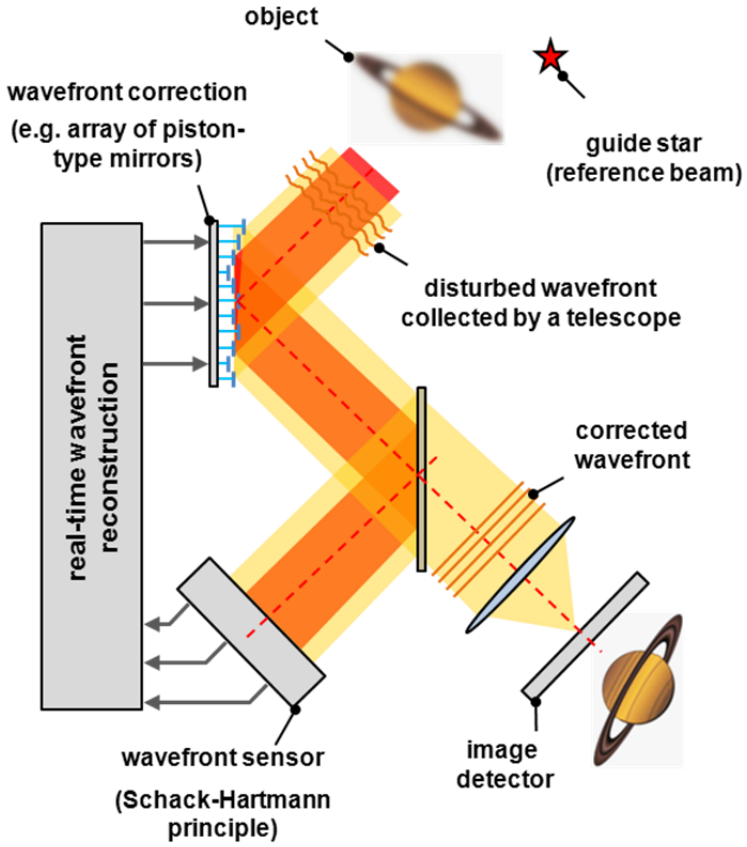

Fig. 3: Adaptive optics in astronomy - compensation of wavefront distortions by use of a pure phase-shifting mirror device e.g. in an adaptive optics telescope [71]

A single pixel of the piston type based IPMS SLM has dimensions of 40µm*40µm and its design is shown in fig. 4a. 240*200 square-shaped mirror plates are suspended over an air gap with an underlying address electrode by means of four cantilever beams and support post. For the electrostatic actuation a voltage is applied between mirrors and address electrodes. The

electric field causes a piston-like deflection of the mirror plates towards the underlying electrodes and results in a pure phase shift [11].

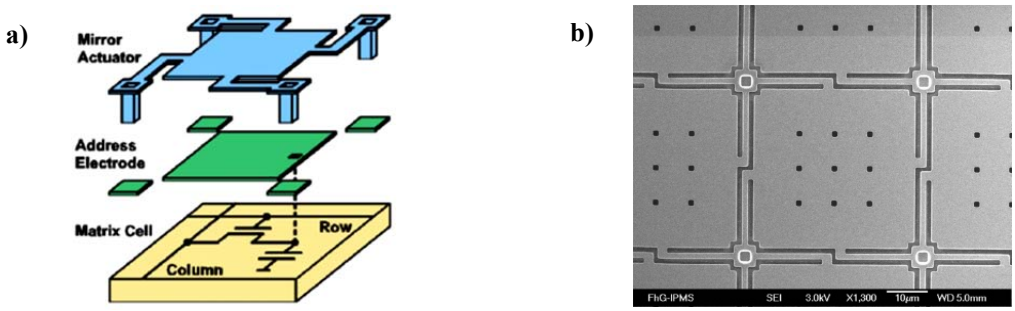

Fig. 4: a) Pixel design of a piston type mirror SLM with matrix cell, address electrode and mirror actuator [11], b) REM graph of piston type mirrors [12]

1.2.3 IPMS – SLM based on arrays of analog tilting mirrors

Another type of SLM developed at IPMS is based on arrays of analogue tilting mirrors presented in [13], [3]. One of the main applications of the IPMS tilting mirror device is microlithography. In this connection, the SLM is used as a programmable mask in laser mask writing tools. Such machines are used for the manufacturing of lithography masks for semiconductor industry. The principle of operation is presented in fig. 5. To generate a certain pattern on the substrate the pattern is first divided in a sequence of rows and the linearized bitmap is sent to the SLM. The SLM is illuminated by a pulsed excimer laser @ 248nm.The laser light hits the SLM surface and the wavefront phase gets modulated by the tilted mirrors. Then the light is imaged onto the substrate. Here, structure details are scaled down by a factor of 200 and the laser fluence is increased by a factor of 200^2. The substrate is scanned row after row to add the single fractions to the final pattern [14].

1.2.4 Design of the investigated tilting mirror

The investigations within the present thesis are carried out on the basis of the mirror type described in the following section. The design of a single pixel is shown in fig. 6 and includes

the mirror plate (fig. 6a) and electrical and mechanical components (different electrodes, torsional springs with yoke) for the mirror actuation (fig. 6 b). The mirror plate is mounted on a yoke and two torsional springs via two posts. The springs have a cross section area of about $0.1*10^{-12}$ m^2 and are mounted on another pair of posts to realize a gap between springs and the electrodes underneath. The actuation of the mirror works electrostatically by applying a voltage between mirror plate and address- and counter-electrode. The electrostatic force causes the mirror to tilt around a tilting axis through the torsional springs [2].

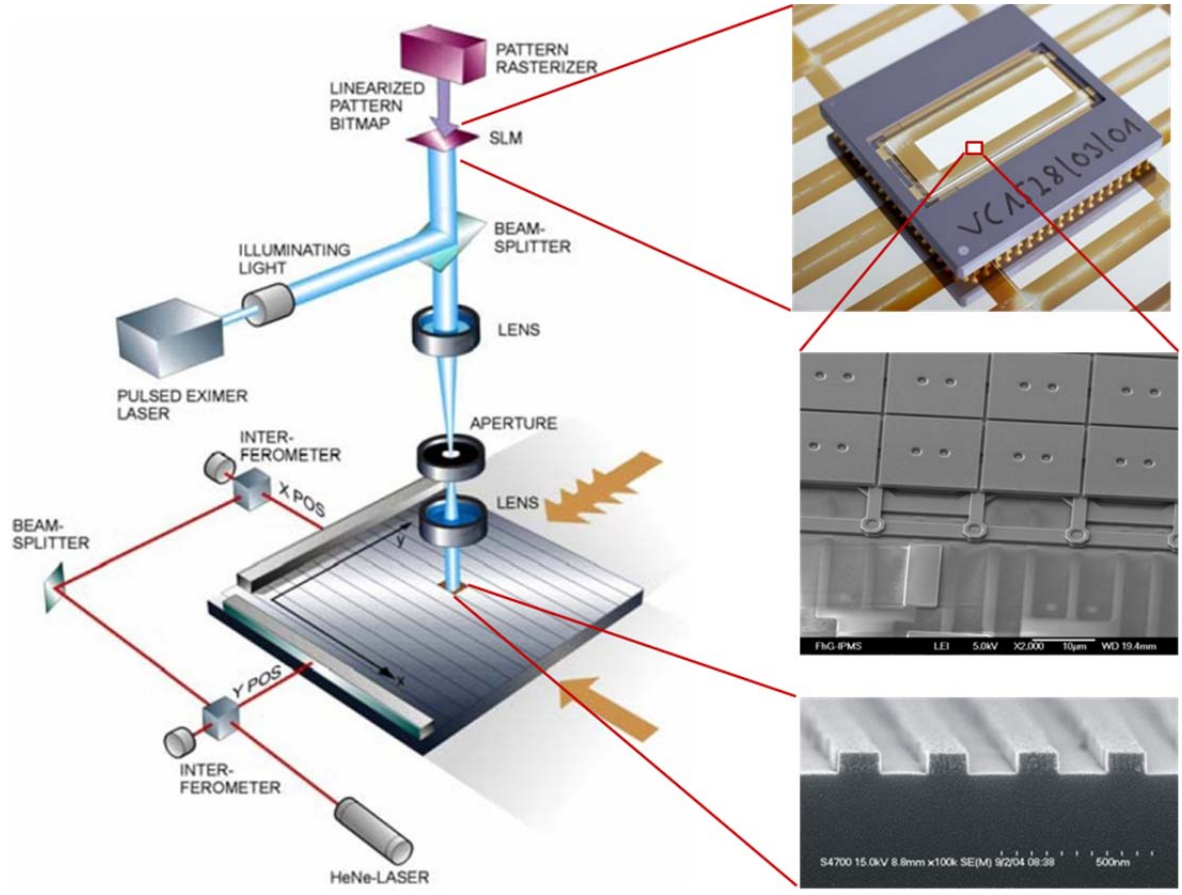

Fig. 5: Principle of operation of a mask less lithography tool using an IPMS SLM based on tilting mirror technology [15]; on the right: a photograph of a SLM bonded in a ceramic package, a SEM showing single mirrors and an SEM image of lithographically processes lines and spaces

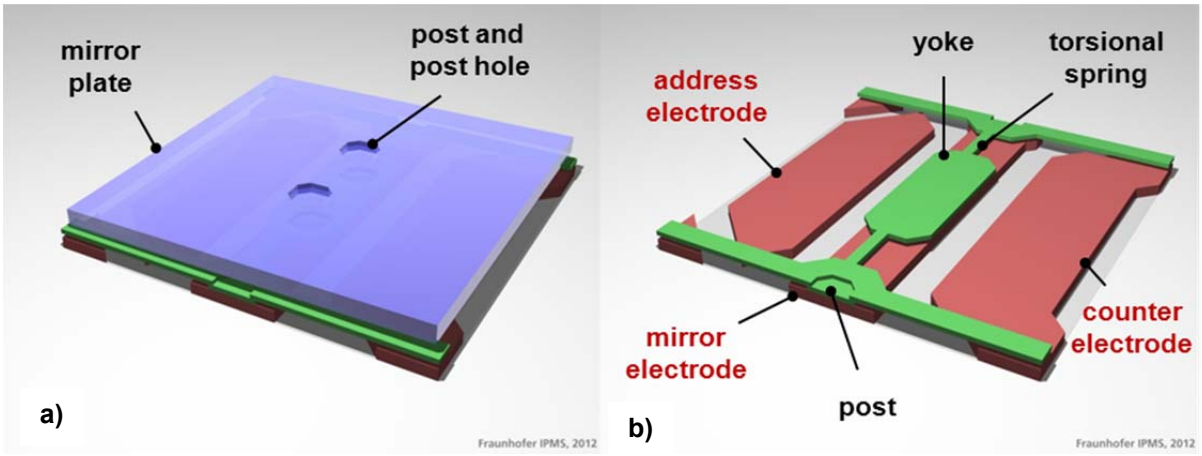

Fig. 6: a) Single 16µm*16µm tilting mirror with mirror plate on top, b) Design of electrical and mechanical components used for the actuation of each mirror (electrodes, torsional springs and yoke)

The pixel pitch is 16µm*16µm, the dimensions of the mirror plate are 15.5µm * 15.5µm * 0.75µm. Considering the slits between the mirrors (0.5µm) and the two post holes (d = 1.6µm) on top of each mirror the entire SLM achieves an optical fill factor of 0.92.

The actuator exhibits a two-layer design which is related to the spatial separation of the mirror suspension (torsional springs) and the reflector (mirror plate) in two independent metallisation layers (fig. 7a,b). The idea is to use different materials and to optimize the mechanical and optical properties of springs and reflector independently [16].

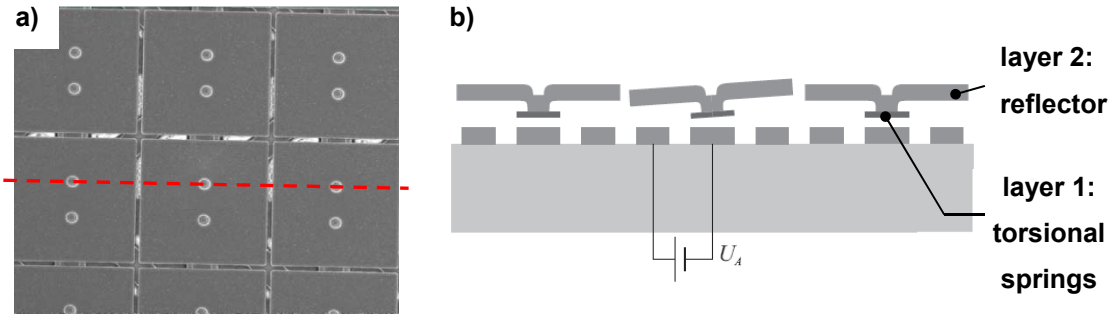

Fig. 7: a) SEM graph with detail of the mirror array, b) cross-section view perpendicular to the mirror tilting axis, showing different metallisation levels for torsional springs and the reflector

The torsional springs are made of a sputter deposited TiAl film with an x-ray amorphous structure and a low stress gradient which makes it an ideal spring material. Compared to former 1-layer Al actuators the TiAl springs show very good deflection stability. The reflector is

made of a sputter deposited Al-alloy film optimized for a reflectivity as high as possible in the DUV region. In both cases one has to consider that the used material for springs and reflector has to be compatible with the manufacturing processes of the underlying CMOS circuitry [12].

On chip control of the mirror array

The SLM consists of 2048 * 512 individual adjustable mirrors. The device can be separated in four logical blocks which are the control unit, column demultiplexer, the row shift register and the active matrix with 2 * 2048*256 pixels (fig. 8). Each pixel has a storage cell consisting of switching transistor and capacitor connected to the mirror's address electrode, see fig.9. An analog voltage is applied to the 256 column demultiplexers with each of them addressing 16 columns. The columns in each block are addressed sequentially for each row. Controlled by the row shift register the procedure is repeated until the whole matrix is completely addressed. The time necessary for the addressing takes about 0.4ms. Adding some time for the irradiation we end up at about 0.5ms. Hence, patterns can be refreshed and imaged with a repetition rate of up to 2kHz [6].

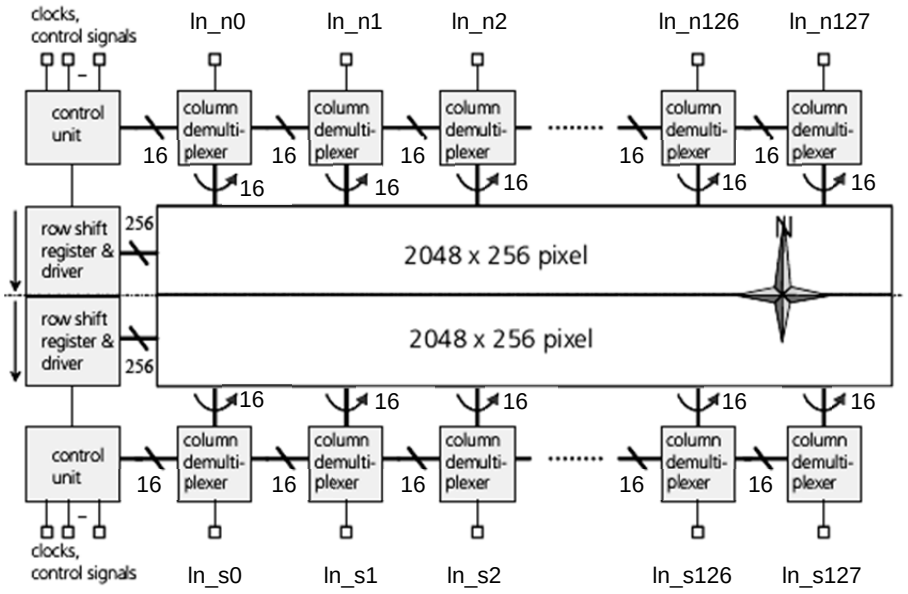

Fig. 8: Functional block diagram of addressing electronics [2]

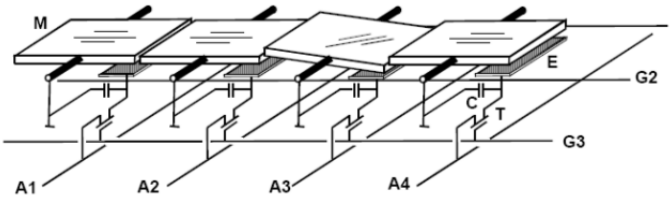

Fig. 9: Individual pixel addressing circuit with analog DRAM architecture [2]

1.3 SLM - imaging principle

1.3.1 Generation of the phase modulation

The SLM imaging principle is based on the modulation of the wavefront phase and on the transformation of the phase modulation into an intensity modulation. An array of tilted mirrors acts as a 2-dimensional reflective phase grating similar to a blazed grating. Incoming light is reflected specular by a single mirror. At the same time an optical path difference of $\overline{AB} - \overline{CD}$ is introduced between two adjacent mirrors and causes interference, see fig. 10.

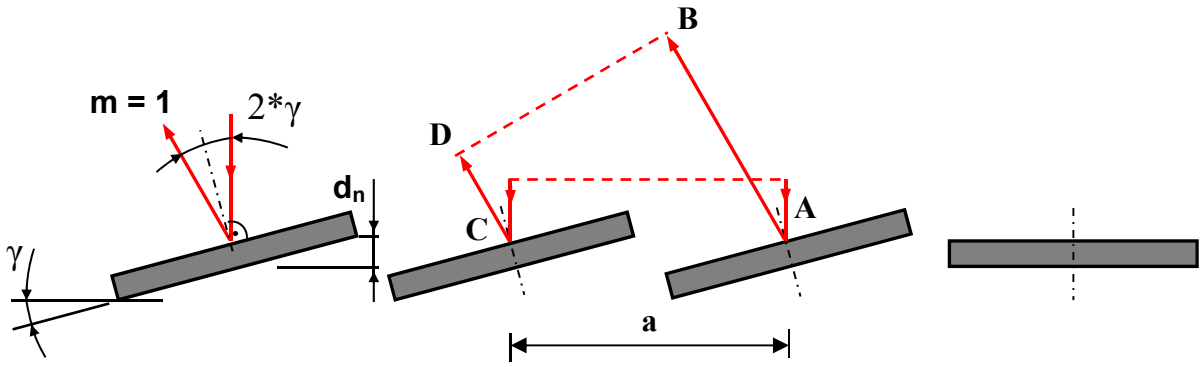

Fig. 10: Introducing the phase modulation by a sequence of tilted mirrors

For normal incidence with respect to the SLM surface, the general grating equation (equ. 1) [17] can be used.

$$a * \sin(2\gamma) = m * \lambda \qquad \textbf{(1)}$$

a - grating pitch, γ – incidence angle on the single mirror, m – order of the diffraction maxima, λ – centre wavelength

Assuming a grating pitch of 16µm and a centre wavelength of 248nm a nominal tilt of γ = 0.44° or d_n = 62nm is required to diffract nearly all photons into the first diffraction maximum. In real operation parameters like the mirror roughness and topography, a possible mirror pre-deflection, differences in the mirror response curve and light coming out of the slits influence the phase modulation and the diffraction efficiency.

1.3.2 Fourier optical imaging principle

The transformation of the phase modulation into an intensity modulation is carried out by a Fourier optical imaging principle, see fig. 11. In the focal plane of a collecting lens which is situated in front of the SLM the Fraunhofer diffraction pattern can be observed. This diffraction pattern shows the far field intensity distribution. Using an aperture placed at the focal plane certain orders of diffraction can be filtered. In our case only the portions within the range of m = ±0.5 orders can pass the aperture and get imaged by a second lens into the image plane. In this way it is possible to create patterns of bright and dark spots.

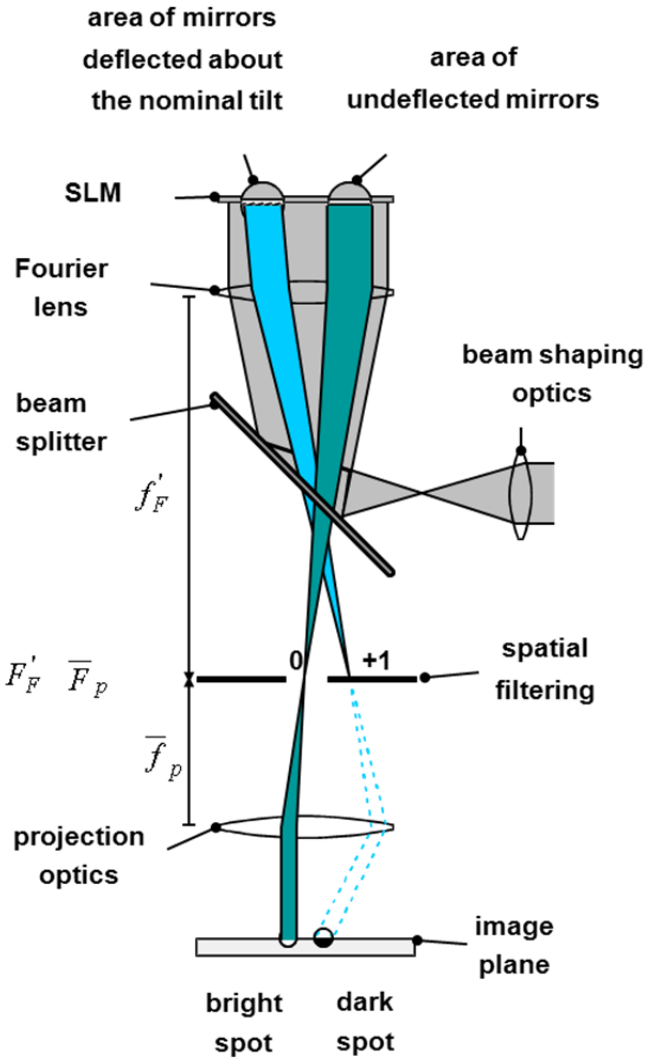

Fig. 11: Fourier optical imaging principle

The generation of patterns or images depending on the arrangement of deflected mirrors is shown in fig. 12. Figure 12a shows an one-dimensional mirror array consisting of 16 mirrors with 2 plus 4 mirrors being tilted about 62nm. The resulting intensity distribution in the Fourier plane and the spatial filtering is shown in fig. 12b. The diameter of the aperture has a width that corresponds ±0.5 orders and blocks all the light from upper orders. The created pattern after passing the projection optics is shown in fig. 12c with bright and dark areas clearly visible. The imaging principle is not limited in the generation of just bright or dark spots. The analog design of the actuator allows a continuous adjustment of any tilt between 0 and λ/4 and beyond that. Hence, it is possible to create gray scales. For detailed information see [13]. The script for this calculation was created by a colleague of my work group and was not part of my thesis.

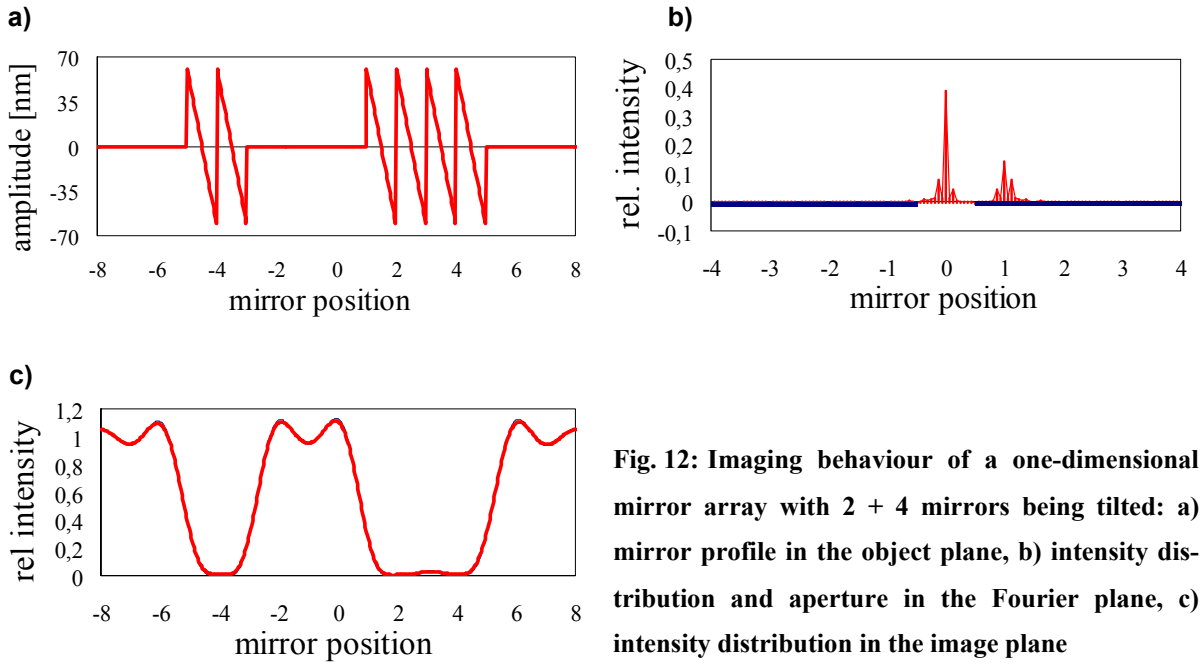

Fig. 12: Imaging behaviour of a one-dimensional mirror array with 2 + 4 mirrors being tilted: a) mirror profile in the object plane, b) intensity distribution and aperture in the Fourier plane, c) intensity distribution in the image plane

There is a significant difference between the analog IPMS - SLM and other devices with digital tilting mirrors. The analog design of IPMS tilting mirrors allows a continuous mirror deflection and the direct generation of selectable gray levels in the image plane see fig. 13. For lithographic applications gray scale imaging is an essential feature and enables the implementation of a sub grid below the device inherent resolution limit. However, this sub grid does not reduce the minimum resolvable feature size but allows the placement of these features anywhere on this sub grid [13].

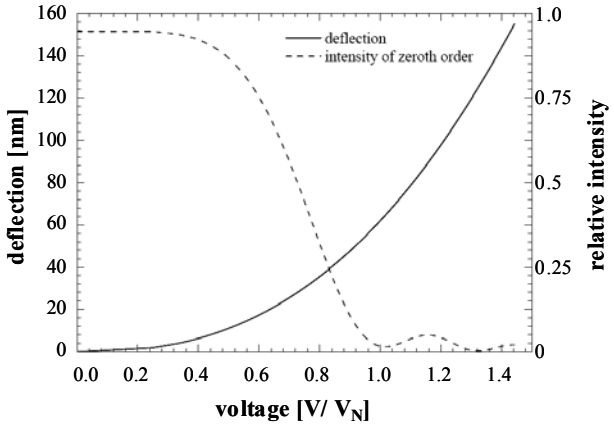

Fig. 13: characteristic curve of the mirror deflection (continuous line) and intensity of the 0th order of diffraction in the image plane (dashed line) versus voltage [13]

1.3.3 Effect of mirror topography on the imaging behaviour

The above described pattern generation showed the theoretical case when using perfect plane mirrors without any artefacts disturbing the created image. However, real mirrors exhibit different artefacts e.g. a real topography and roughness or a pre-tilt that worsens the diffraction efficiency of the light modulator. The imaging behaviour of slightly curved mirrors is shown in fig. 14. The mirrors show a parabolic curvature with a height difference of 31nm from the edge to the centre. This height difference equals half of the nominal tilt in normal operation. Compared to the ideal case shown above a deformation of the created pattern and a degradation of image contrast is visible, fig. 14b. Both result in a decrease of the possible resolution of image details.

The simulation emphasizes the need to detect the mirror topography directly during the laser exposure and is the main motivation for the present thesis.

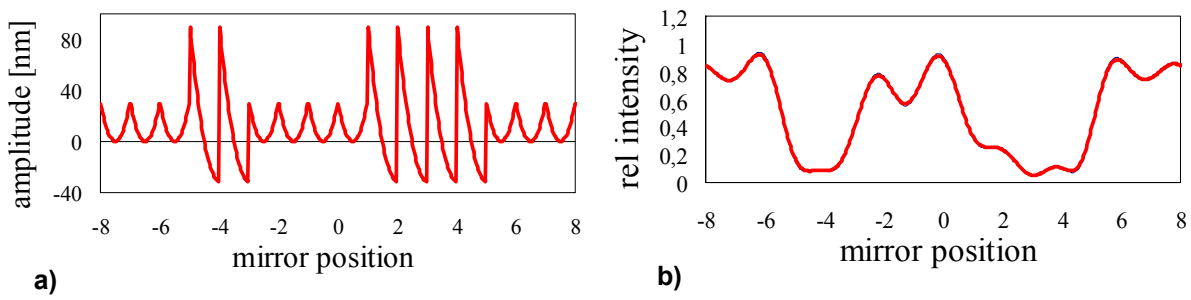

Fig. 14: Imaging behaviour of a one-dimensional array of parabolic curved mirrors with a bow of 31nm: a) mirror profile in the object plane, b) intensity distribution in the image plane

1.4 Radiation induced degradation effects of MEMS and MOEMS

The following section shall provide an overview of radiation induced degradation effects of MEMS and MOEMS. The term degradation usually describes the gradual change of physical and chemical material properties. Within the context of radiation induced effects on MEMS there is another significant component, which is the disturbance of the device actuation. Radiation induced ionization can disturb electrostatic driving principles and cause serious device failure. Although ionization does not match the definition of degradation it is also included in the following chapter.

The comprehensive topic of light and MEMS interaction includes different fundamental aspects like characteristic of the particular radiation, the MEMS actuation principle, actuator design and involved materials. Additionally it is useful to distinguish between different failure modes. Typical impairments are the disturbance of the actuation principle and radiation induced degradation and damage. First actuators made in silicon were developed in the 1960s leading to first MEMS devices in terms of pressure sensors in the 1970s [18]. For MEMS fabrication silicon is a widely-used material. Consequently available literature is focused on silicon based devices in large part. Outstanding applications in this context are the use of MEMS in space or MOEMS for laser applications.

An overview about research activities of several authors in the field of MEMS devices used in space missions is summarized by Herbert Shea. These activities include the interaction of x-rays, gamma radiation, electron and proton beams with MEMS devices typically made of silicon. At doses typical for one year in most orbits mechanical degradation has not been observed at all. In fact, the radiation sensitivity appears by means of radiation induced charge trapping in dielectrics and its impact on the MEMS operation principle. Devices operating on electrostatic principles were affected most [19 - 21].

1.4.1 Laser induced failure of silicon based devices

The group of polysilicon based devices includes bare polysilicon actuators and also these covered with a metallic layer with a thickness of up to 100nm. In these 2nd case it is just assumed that the overall device performance is still mainly determined by the underlying silicon substrate. Typical devices in this group are micro mirrors, scanners, cantilevers, flaps or generally optically driven actuators with dimensions of up to a few hundred microns. These actors are often made of bare polysilicon layers of just 1µm to 2µm. For higher reflectivity applications

they are covered with metal layers of Au, Ag, Al or AlCu or multi-layer dielectric mirrors. Most of the reported irradiation tests were done in VIS and the NIR spectral region using cw-lasers. The range of investigated irradiance varies from several hundred of W/cm^2 to above 10kW/cm^2. At lower power levels bowing and deformation of the optical surface are reported. These deformations can occur dynamically during the pulse (rather elastic deformation) or permanently (plastic deformation). Even a slight bowing of some nanometers can be a significant problem when optical surfaces with a flatness of a fraction of the intended wavelength are required. The bowing is e.g. caused by the mismatch of the thermal expansion coefficients of substrate and coating. Further reported degradation mechanisms are grain growth, recrystallization and the transfer of coating material into the grain boundaries of the underlying silicon. At higher power levels catastrophic failure usually in terms of surface melting occurs. [22 - 28].

Though silicone is a widely used material for MEMS fabrication, the actuator in the present thesis are made of an aluminium alloy. Degradation mechanisms in aluminium can be completely different to these in silicon. Therefore it is meaningful to distinguish between these materials. But the available literature in the field of metal based MEMS/ MOEMS and laser induced degradation is very limited. A few papers are discussed in the following section.

1.4.2 Laser induced failure of metal based devices

The group of metal based devices includes e.g. metallic actuators (often aluminium or aluminium alloys) usually covered with a single dielectric layer (e.g. MgF_2, AlF_3, LaF_3, Al_2O_3, SiO_2) acting as protection against physical and chemical degradation or as reflectivity enhancement. Also included are metallic actuators covered with dielectric multi-layer mirrors for highest reflectivity at narrow spectral bands or particular laser lines. And the group also includes silicon actuators covered with metallic layers of several hundred nanometers where the metallic layer is assumed to determine the overall actuator performance significantly. Such metallic MEMS comprise actuators like single micro mirrors or micro scanning mirrors of a few hundred microns and arrays of micro mirrors of some ten microns. The irradiation experiments were carried out in the DUV, VIS and NIR spectral region (193nm – 1064nm) using cw and pulsed lasers. Here laser pulse lengths from 10^{-9}s to 10^{-3}s were applied on the samples. The range of applied irradiance/ fluence varies from some ten W/cm^2 to some kW/cm^2 and from some ten mJ/cm^2 to 2mJ/cm^2. The duration of reported tests was in the range of some hours or 10^7 pulses respectively.

At lower power levels bowing and deformation of the optical surface and other actuator elements (springs, supports) both of elastic and plastic manner is reported. The irradiation of silicon actuators with metallic coatings at rising power levels occasionally resulted in a significant loss of reflectivity. Thicker coatings (≥100nm) showed rather stable reflectivity within the tested period. At maximum power level serious degradation in terms of surface roughening or agglomeration of the coating occurred. Furthermore damage in terms of melting and ablation of the coating material is reported [29 – 33].

1.4.3 Laser induced ionization effects

The above mentioned charging effects are not limited to space applications. Laser induced charging effects during the operation of micro mirror devices for deep ultraviolet (DUV) mask writing are e.g. described in [34, 35]. During the irradiation of the device with DUV laser light in air ozone was generated. In combination with the applied electrical field the ozone causes an oxidation of the titanium nitride on top of the device electrodes (fig.15a).

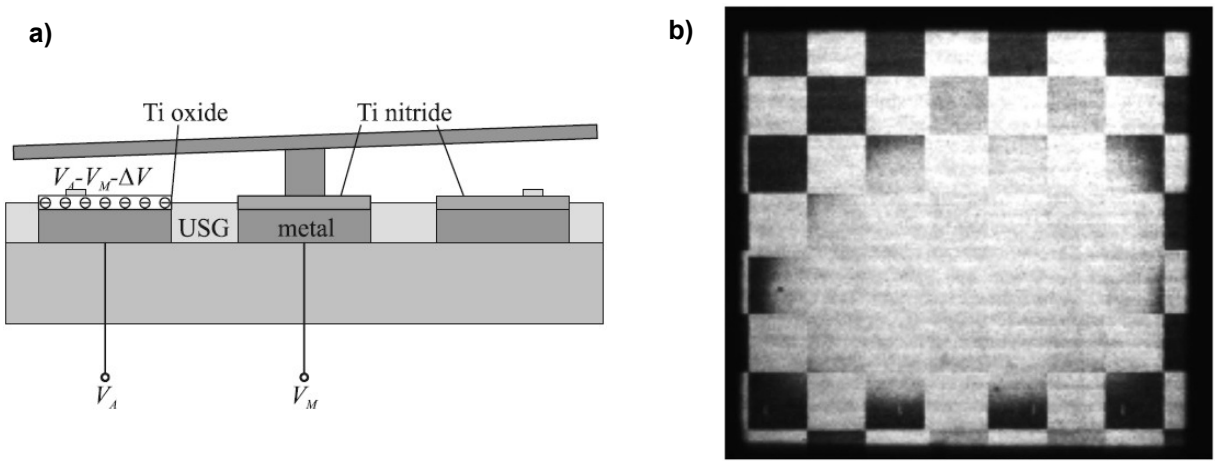

Fig. 15: a) Oxidation of titanium nitride electrodes and charge trapping caused by laser-induced ozone and the applied electric field, b) loss of modulation of the imaged pattern [34]

Within minutes charge trapping inside the titanium oxide layer is observed, resulting in the attenuation of the electric field responsible for the actuator deflection. As a consequence the actuators deflection is almost reduced to zero and the imaged pattern is losing its modulation, see fig. 15b.

1.5 Interaction of laser light with metals

1.5.1 Optical properties of metals (at room temperature)

When radiation hits matter, typical fundamental processes like reflection, refraction, transmission and absorption are observed. In case of optically transparent media, the radiant flux Φ_{e0} that enters the material remains nearly unchanged. But, when an electromagnetic wave enters a metallic sample, a so-called absorbing material, the electric field collapses very soon and the material appears nontransparent. The typical penetration depth of DUV light in aluminium is in the range of a few nanometers, see equ. 4 below. Responsible is a characteristic property of metals, which is the presence of unbound electrons, that can move within the material. These conducting electrons dominate the optical response of metals to radiation. When an electromagnetic wave enters a conducing material the oscillating electric field accelerates the unbound electrons, which scatter and the energy of the wave is turned into Joule heating. Depending on their conductivity, metals exhibit absorption coefficients up to $5*10^6$ cm^{-1} (Ag at λ = 630nm). For radiation with wavelength above 15µm, the optical properties are mainly determined by the material's conductivity. For radiation with lower wavelength the situation changes and the molecular structure of matter has to be considered [36][1], [37][2].

For highly absorbing materials, the refractive index n is replaced by the complex index of refraction $\mathbf{n}$ with real part n and imaginary part k, termed the extinction coefficient (see equ. 2). This modification allows to transfer formalisms of transparent optics to highly absorbing materials.

$$\mathbf{n} = n - ik = n(1 - i\kappa) \qquad \textbf{with} \qquad k = n\kappa \qquad \textbf{(2)}$$

$\mathbf{n}$ = complex index of refraction, n = refractive index (real part of $\mathbf{n}$), k = extinction coefficient (imaginary part of $\mathbf{n}$), κ = absorption index

Based on the material quantities refractive index-n and absorption index-κ further optical parameters can be derived. Equation 3 and 4 describe the reflectance-R of a metallic surface in air for normal incidence and the absorption coefficient-α. [36][3], [37][4].

[1] [36 – p. 246, 272]
[2] [37 – p 258 ff.]
[3] [36 – p. 272ff]

$$R = \frac{I_r}{I_0} = \frac{(n-1)^2 + n^2\kappa^2}{(n+1)^2 + n^2\kappa^2} \qquad \textbf{(3)} \qquad\qquad \alpha = \frac{4\pi}{\lambda} n\kappa \qquad \textbf{(4)}$$

R = reflectance, I_r = reflected intensity, I_0 = incident intensity, α = absorption coefficient, λ = wavelength

A metallic evaporated aluminium film with $n = 0.19$ and $k = 2.94$ shows a reflectance of $R \approx 0.92$ for radiation of $\lambda = 248$nm. However, these numbers can differ significantly in practice depending on surface characteristics and deposition conditions [38][5]. From equ. 4 it follows the absorption coefficient of $1.49*10^6 cm^{-1}$ and the penetration depth of $d \approx 7nm$ with $d \equiv \alpha^{-1}$, correlating with the distance where the initial radiant flux is reduced to $\Phi_{e0}\, e^{-1}$. For a metallic film with a thickness, causing absorption of all incoming radiation that was not reflected, the absorptivity A is defined as

$$A = 1 - R \qquad \textbf{(5)} \qquad \textbf{[37]}$$

1.5.2 Frequency dependence of reflectance and absorption

The above mentioned material parameters show a significant dependence to the frequency of the incoming radiation, see fig. 16. As a critical frequency, the so called plasma frequency ω_p has to be emphasized. For evaporated metallic aluminium the wavelength equivalent to $\omega_p \sim$ 83nm [38]. In metals, conducting electrons and positive charged ions can be considered as a plasma, with its density oscillating with the eigenfrequency ω_p, called the plasma frequency. The plasma frequency separates two regimes of different optical properties. For $\omega < \omega_p$ metals show rather large R and α and the refractive index exhibits real and imaginary part. For $\omega > \omega_p$ the material shows rather small R and α and the complex index of refraction is reduced to its real part again [17][6].

[4] [37 – p. 261]
[5] [38 – p. 397 ff]
[6] [17 – p. 202]

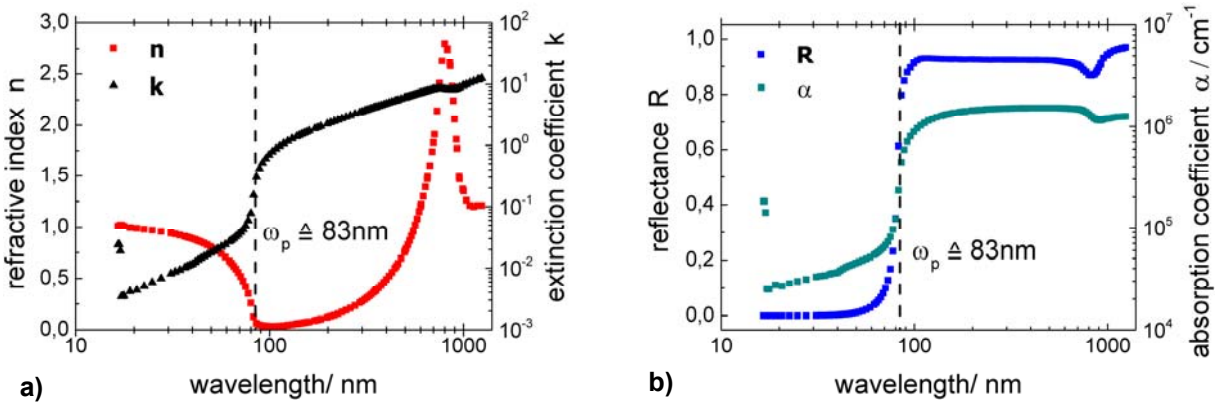

Fig. 16: Wavelength dependence of: a) refractive index n and the extinction coefficient k, b) reflectance R and absorption coefficient α of evaporated metallic aluminium [38]

1.5.3 Real metallic surfaces

The optical properties of real metallic surfaces usually differs significantly from the technically material data. The experimentally determined data for reflection and absorption do not just include the intrinsic material properties but also a real sample surface and material specifics in the surface near layer. The differences between intrinsic and real data arise from surface roughness, film morphology, from surface oxide layers , residual gas incorporated in the surface near region and from surface-adsorbed substances [39][7], [38]. For this purpose fig. 17 compares the reflectance of metallic aluminium surfaces with different characteristics. The uppermost curve shows opaque evaporated aluminium films prepared in ultrahigh vacuum ($\approx 10^{-9}$ mbar). These films are presumed to be free of bulk and surface oxide contamination. The reflectance was obtained by extrapolating the reflectance back to the time where the evaporation was completed. The curve in the middle shows the average of films evaporated in high vacuum ($\approx 10^{-5}$ mbar) where surface and bulk oxidation occurs. The lowermost curve shows mechanically polished samples and sputtered films [38][8].

[7] [39 – p. 19]

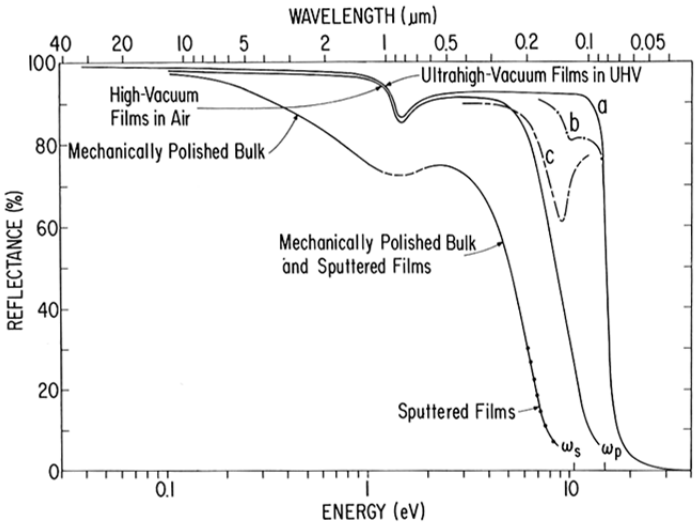

Fig. 17: Reflectance of metallic aluminium at room temperature: Uppermost curve: reflectance of opaque evaporated aluminium films prepared in ultrahigh vacuum (≈ 10^{-9} mbar), presumed to be free of bulk and surface oxide contamination; middle curve: shows the average of films evaporated in high vacuum (≈ 10^{-5} mbar) where surface and bulk oxidation occurs; lowermost curve: mechanically polished and sputtered films [38][8]

1.5.4 Further dependencies of the optical quantities

Beside the above mentioned dependencies metallic samples show further dependencies of the optical constants. Figure 18a shows the reflectance versus the angle of incidence for Al + a natural oxide layer of 5nm at λ = 248nm. The curves were simulated with material data from [38]. The irradiation experiments are carried out with laser light with TM polarization and an incidence angle of 55°, which is unfortunately close to the minimum reflectance around 65°. Figure 18b shows the temperature dependency of the absorptivity of an unpolished aluminium sample @ λ = 10.6μm. At this, one observes an increase of by 1.5 times from zero degree to the melting point.

[8] [38 – p. 389]

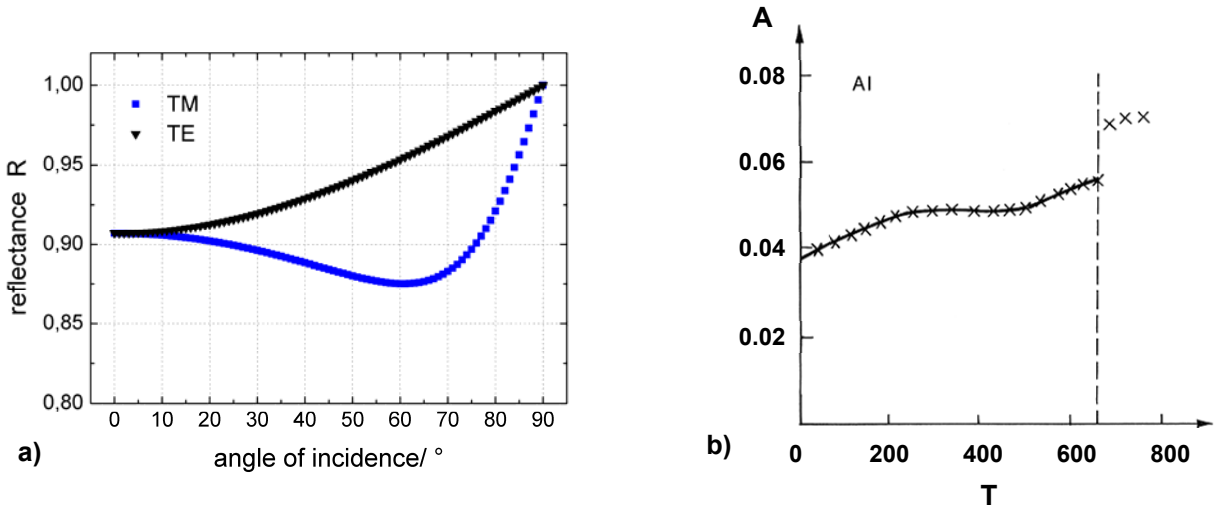

Fig. 18: Further dependencies of optical constants: a) Dependency of the reflectance from the angle of incidence for Al + 5nm Al_2O_3 @ 248nm simulated with material data from [38], b) Temperature dependency of the absorptivity of an unpolished aluminium sample @ λ = 10.6µm [39][9]

1.5.5 Laser-induced heating of metal targets

The following chapter describes the laser-induced heating of metal targets below the melting temperature. Laser radiation energy is absorbed by electrons near the sample surface and then transferred to the lattice by inelastic electron-phonon scattering processes. For typical metals, it takes $0.1*10^{-12}$s - $1*10^{-12}$s to reach thermal equilibrium between electrons and lattice [69]. The thermal propagation in homogeneous and isotropic media in terms of $\vartheta(x,y,z,t)$ is described by the heat conduction equation, see equ. 6. However, the temperature dependence of specific heat capacity and the thermal conductivity are ignored [70].

$$\frac{\partial \vartheta}{\partial t} = \kappa_{th} \nabla^2 \vartheta + \frac{\dot{W}(x,y,z,t)}{\rho c} \quad (6) \qquad \text{with} \qquad \nabla^2 \vartheta = \left(\frac{d^2\vartheta}{dx^2} + \frac{d^2\vartheta}{dy^2} + \frac{d^2\vartheta}{dz^2} \right) \quad (7)$$

ϑ-temperatur, κ_{th}-thermal diffusivity, ρ-sample density, **and** $\kappa_{th} = \frac{k_T}{\rho c}$ **(8)**

c-specific heat capacity, $\dot{W}$ -heat source inside the sample, k_T-thermal conductivity

[9] [39 – p. 35]

Depending on sample and laser beam dimensions [39] found solutions of equ. 6 for different practical applications. Samples with a thickness smaller than the thermal propagation length ($h < l_{th}$) can be characterised with the *finite thickness model.* In the present case, an aluminium sample with $\kappa = 9.5*10^{-5} m^2/s$ and h = 320nm is irradiated with a laser pulse with $\tau_p = 16ns$. From this it follows a propagation length of the laser induced heat wave within the duration of a single pulse of $l_{th} = \sqrt{\kappa_{th}\,\tau_p}$ $l_{th} \approx 1.2\mu m$ [39][10]. Within the *finite thickness model* "small" and "large" irradiation spots are distinguished. In the present case with the spot diameter $D_s >> l_{th}$, the laser spot is assumed as a plane heat wave, see fig. 19 [39].

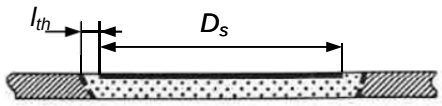

Fig. 19: Laser induced-heating of a thin metallic sample with the diameter of the irradiation spot $D_s >> l_{th}$ (thermal diffusion depth)

Within the *plane heat wave approximation* and assuming a uniform beam profile, the temperature field only depends on the z-coordinate and time. For z = h, the temperature inside the sample is given by equ. 9 [39][11].

$$T(z,t) = \frac{A I_0 \tau_p}{c \rho h} + \frac{A I_0 \tau_p}{k_T}\left[\frac{3z^2 - h}{6h^2} - \frac{2}{\pi^2}\sum_{n=1}^{\infty}\frac{(-1)^n}{n^2}\exp\left(-\frac{\kappa_{th}{}^2 n^2 \pi^2 \tau_p{}^2}{h^2}\right)\cos\frac{n\pi z}{h}\right] \qquad \textbf{(9)}$$

A = spectral absorptivity, I_0 = laser intensity, τ_p = pulse duration, h = sample thickness, z = observation depth, n = number of reflections of the heat wave at the sample boundaries, κ_{th} = thermal diffusivity

The first term in equ. 9 includes a linear rise of the temperature with the time. The second term adds the effect of the heat wave being multiple reflected at the mirror boundaries. However, in the present case, the effect of the reflected heat wave on the average mirror temperature is minimal. Consequently, equ. 9 can be simplified and reduced to the first term. The resulting expression (equ. 10) can be compared with the charging characteristic of a capacitor, being charged with a constant-current source (equ. 11). At this, the accumulated photon ener-

[10] [39 – p. 42]
[11] [39 – p. 66]

gy during a single laser pulse corresponds to the charge Q and the thermal mass $m*c$ corresponds to the capacitance.

$$T(z,t) = \frac{AI_0 t}{c\rho h} \triangleq \frac{Q}{m*c} \qquad (10)$$

$$U = \frac{Q}{C} \qquad (11)$$

U = voltage, Q = charge, C = capacitance

Following from equ. 10, fig. 20a shows the expected temperature rise of a mirror resulting from a single laser pulse at 248nm. The assumed quantities are summarized in table1. The applied model is a strong simplification of real circumstances. Due to the short time scale of a few nanoseconds heat transfer into the substrate and heat exchange with the environment are ignored.

mirror dimensions	**15µm*15µm*320nm**
laser wavelength	**248nm**
pulse length	**16ns**
pulse energy	**10mJ/cm^2**
absorptivity	**0.2**

Table 1: Quantities for estimation of mirror heating resulting from a single pulse

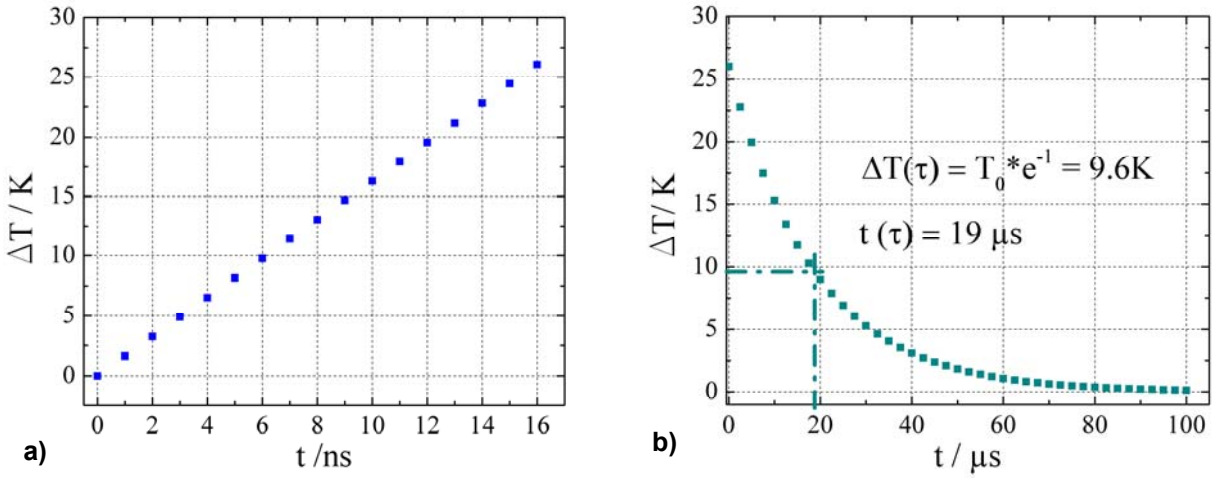

Fig. 20: a) Expected temperature rise of an Al mirror (15µm*15µm*320nm) resulting from a single laser pulse at λ = 248nm, $\tau_p = 16ns$, pulse energy = 10mJ/cm^2, A = 0.2; b) Expected temperature decrease subsequent to the laser pulse, considering heat conduction into the substrate via the gas gap and the elements of the actuator

The expected cooling rate of a single mirror subsequent to a laser pulse is presented in fig. 20 b) above. The model describes the heat transfer from the mirror plate into the underlying substrate due to a thermal gradient ΔT by heat conduction within a solid (actuator elements) and within a gas-filled gap (between mirror and substrate). The two heat guiding paths with actuator elements and N_2-filled gap act like a parallel arrangement of different thermal resistors (see fig. 21).

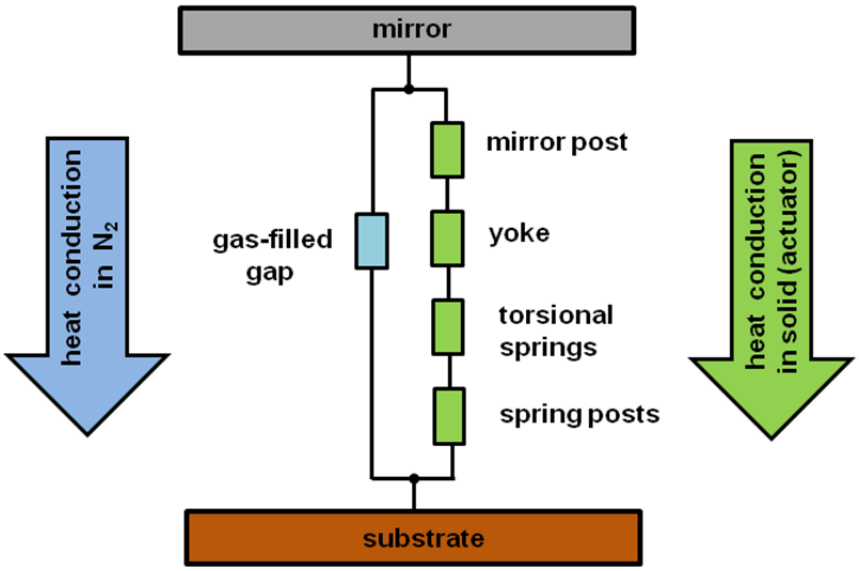

Fig. 21: Heat transfer from the mirror plate into the substrate considering heat conduction within a solid (actuator elements) and the N_2-filled gap

The heat guiding elements in both paths are additionally depicted in fig. 22. Within the solid the heat is transferred from the mirror along the mirror posts, the yoke, the torsional springs, the spring posts and into the substrate (fig. 22a). The overall thermal resistance within this path is the summation of the four actuator elements. The heat transfer via the gas-filled gap is described by a simplified 2-d model (fig. 22b). Here a gap height of 700nm is assumed. The yoke (layer), which is also situated between mirror and substrate, can be neglected. Its thermal resistance within this path is orders of magnitude smaller compared to the gas. The heat transition from solid (mirror) into the gas and from the gas into the solid (substrate), which might introduce an additional resistance, is not considered. For such a consideration microscopic properties of the boundary layer between both media and detailed knowledge of the processes within the gap would be required.

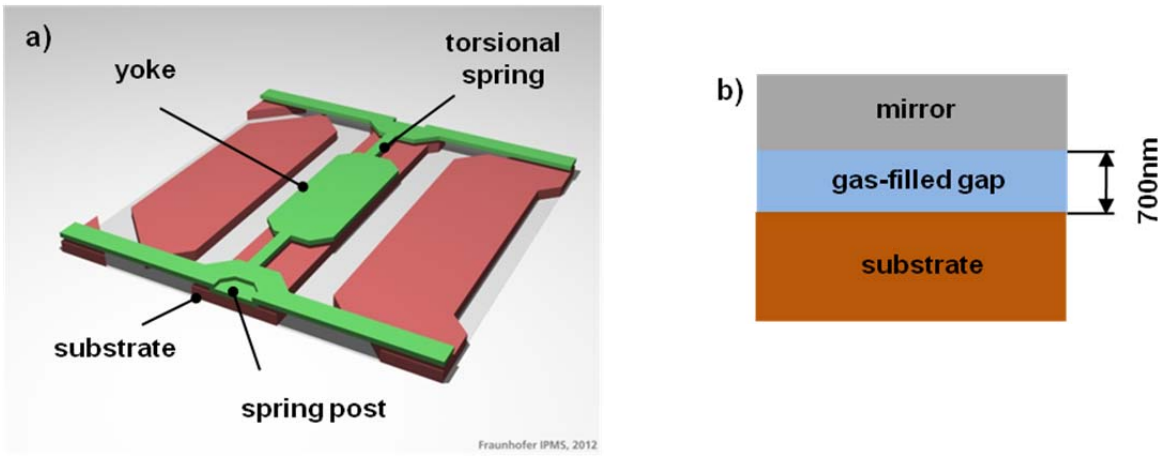

Fig. 22: a) Depiction of heat guiding elements (yoke, torsional springs and spring posts), b) simplified 2-d model of the heat transfer via the gas-filled gap between mirror and substrate

The exponential decay of the mirror temperature in fig. 20b follows from equ. 12 below. The expression is also known from discharging a capacitor via a RC-circuit. The thermal resistance in each heat guiding path results from equ. 12-2. The thermal resistance of the actuator elements (within the solid) depends on each element's dimensions and its thermal conductivity. The overall resistance within this path is mainly determined by one element, the torsional springs. The springs have by far the smallest cross section and hence the highest resistance of all elements. The thermal resistance of the gap depends on the assumed gap height (700nm), its cross-section and the thermal conductivity of the media (N_2). The overall thermal resistance R_{th} of both paths results from the parallel arrangement of $R_{th\ gas}$ and $R_{th\ sol.}$ (equ. 12-1). With $R_{th\ gas}$ = 2.0*10^{5}K/W and $R_{th\ sol.}$ = 1.7*10^{6}K/W the resulting overall resistance equals 1.8*10^{5}K/W. Accordingly most of the heat is transferred via the N_2-filled gap.

$$\Delta T = T_0 * exp\left[-\frac{t}{R_{th}*C_{th}}\right] \quad (12) \qquad \frac{1}{R_{th}} = \frac{1}{R_{th\ gas}} + \frac{1}{R_{th\ sol.}} \quad (12\text{-}1)$$

$$R_{th} = \frac{1}{k_T} * \frac{l}{A_{th}} \quad (12\text{-}2) \qquad C_{th} = m * c \quad (12\text{-}3)$$

$$\tau = R_{th} * C_{th} \quad (12\text{-}4)$$

ΔT = temperature gradient, T_0 = initial temperature, R_{th} = overall thermal resistance in both heat guiding paths, $R_{th\ gas}$ = thermal resistance of the gas-filled gap, $R_{th\ sol.}$ = thermal resistance of the actuator elements, C_{th} = thermal mass, k_T = thermal conductivity, l = length of a particular heat conducting element, A_{th} = cross

section of a particular heat conducting element, m = sample mass, c = specific heat capacity, τ = time constant for $\Delta T(\tau) = T_0 * e^{-1}$

The time constant τ with $\Delta T(\tau) = T_0 * e^{-1}$ is determined by means of R_{th} and C_{th} the thermal mass of the mirror (equ.12-4). With R_{th} = 1.8*10^{5}K/W and C_{th} = 1.1*10^{-10}J/K, τ equals 19μs. In Chapter 3 the theoretical data will be compared with real experimental data.

1.6 Areal surface texture measurement

The measurement of surface texture can be distinguished in the determination of a surface profile $z(x)$ and an areal surface measurement $z(x, y)$. A surface profile is determined by tracing a contacting stylus across the surface and measuring the vertical motion of the stylus as it traversed the surface features. The result is a height function with lateral displacement $z(x)$. On the other hand, the use of optical methods allows an areal and non-contact determination of surface texture with a height function showing the displacement across a plane $z(x, y)$ [40]. In the present thesis phase-shifting interferometry was used to describe the sample surface. Consequently, the following chapter contains explanations about an areal surface measurement exclusively.

1.6.1 Areal specification standards

Entitled as *Geometrical product specification (GPS) – surface texture: areal:* a standardisation of areal surface measurement has been carried out by the International Organization for Standardization recently. For this purpose, ISO 25178 contains definitions of terms and parameters, different measurement methods, calibration methods, file formats and characteristics of instruments. The following parts of ISO 25178 are of concern when doing areal surface characterization by means of phase-shift interferometry.

Part 2:	Terms, definitions and surface texture parameters
Part 3:	Specification operators
Part 6:	Classification of methods for measuring surface texture
Part 70:	Physical measurement standards
Part 603	Nominal characteristics of noncontact (phase-shifting interferometric microscopy) instruments [40, 46 – 50]

Definition of the measurand - bow

In general, the mirrors itself and their performance in service is being investigated to characterize the manufacturing process on the one hand and to characterize the effect of irradiation on the other hand. For this purpose, different properties as the mirror z-position, the mirror pre-deflection and deflection characteristic in service and the single mirror topography is determined. The curvature of a single mirror directly determines the imaging behaviour and fi-

nally the contrast of the generated patterns in the image plane. From this arises one of the main questions of the present thesis which is the effect of UV-laser light on the topography of single micro mirrors. Curvatures of optical surfaces are usually described by the radius of curvature. But in the present experiment a measurement delivers an average of the topography data of about 500 single mirrors. In such a case, single very planar samples with radii of up to several thousands of millimetres would influence the arithmetic mean significantly. Therefor the measurand "bow" has been chosen alternatively. For receiving the bow of a certain mirror the surface is first fitted by a cylinder in x- and y-direction. The bow, which is consistent with the height of a circular segment, is then determined with the cylinder's radius. see fig. 23. In order to consider a possible effect of the mirror design, the bow is determined both, in x- and y-direction.

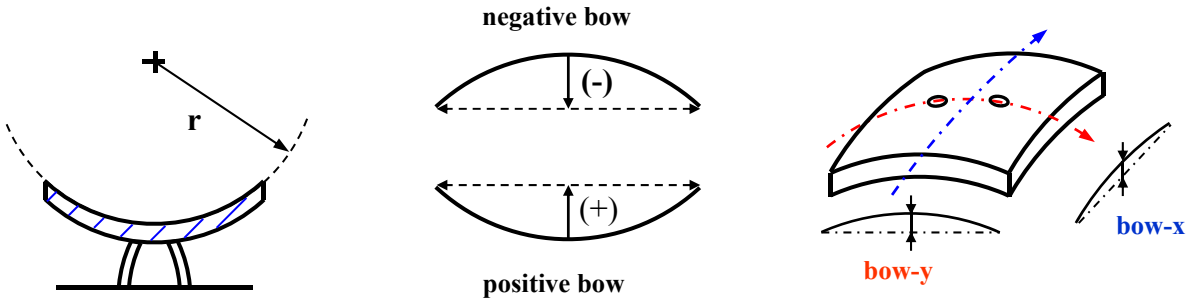

Fig. 23: Definition of the measurand bow: a) Sample surface is fitted by a cylinder in x- and y-direction, b) definition of the bow with positive and negative algebraic sign, c) definition of the bow in x- and y- direction by means of the depicted 2-post design

In ISO 25178-2 the procedure of describing a mechanical surface is done by dividing the surface in elements of areas, elements of lines and elements of points. However, this procedure seems not to be suited for the present case, where no detail information but a general description of the mirror topography by its mean curvature is required.

Considerations when choosing the measurement method

Several considerations, supporting the decision for a certain measurement method, are listed by [40]. This list includes amongst others the type and characteristic of the surface, the type and amount of information necessary for the description of the surface texture, the measurement uncertainty, the tolerable duration for the generation of the measurement data and finally the available budget.

The fundamental aim of the measurement is the determination of the topography of a single micro mirror and a possible topography change due to irradiation with laser light. Table 2 shows a list of requirements for the characterisation of the mirror topography in the context of this thesis. A fundamental boundary condition is the performance of the measurement parallel to the real irradiation. The requirements were mostly defined by the IPMS.

MEASUREMENT CATEGORY	AREAL NON CONTACT SURFACE CHARACTERISATION
sample characteristic:	metallic non transparent optical surface
another boundary condition	irradiation of the sample with laser light in parallel
field of view	10*10 mirrors (160µm * 160 µm)
resolution	
resolution in z	1nm
resolution in x, y	1µm
maximum step height:	100nm
measurement error	
random error (3σ):	0.3nm
systematic error:	1nm
duration of data generation:	≤ 10s
size of measuring station:	transportable
budget:	≤ 20,000 EUR

Table 2: List of requirements and boundary conditions to make the decision for a certain measurement method within the context of this thesis.

1.6.2 Possible measurement methods

Diffraction pattern analysis:

The SLM mirror array acts as a two dimensional phase grating. According to the Fourier-optical imaging principle, a phase modulation in the mirror plane results in a change of the intensity distribution in the so-called Fourier plane. The Fourier plane is the focal plane of a

collecting lens situated in front of the SLM and contains the Fraunhofer diffraction pattern (far field intensity distribution) of the modulated laser light (see fig. 11). The approach is to identify a change of the single mirror curvature by its effect on the intensity distribution of the diffraction pattern in the Fourier plane (fig. 24a). The expected effect of a curved mirror is depicted in fig 24b. The curved mirror (violet graph) with a bow of λ/10 results in a decrease of the central diffraction order of 20%. But in real operation the intensity distribution is also affected by other quantities like a statistical mirror pre deflection and the response curve of the particular mirror. For the diffraction pattern analysis the separation of the different quantities would be necessary.

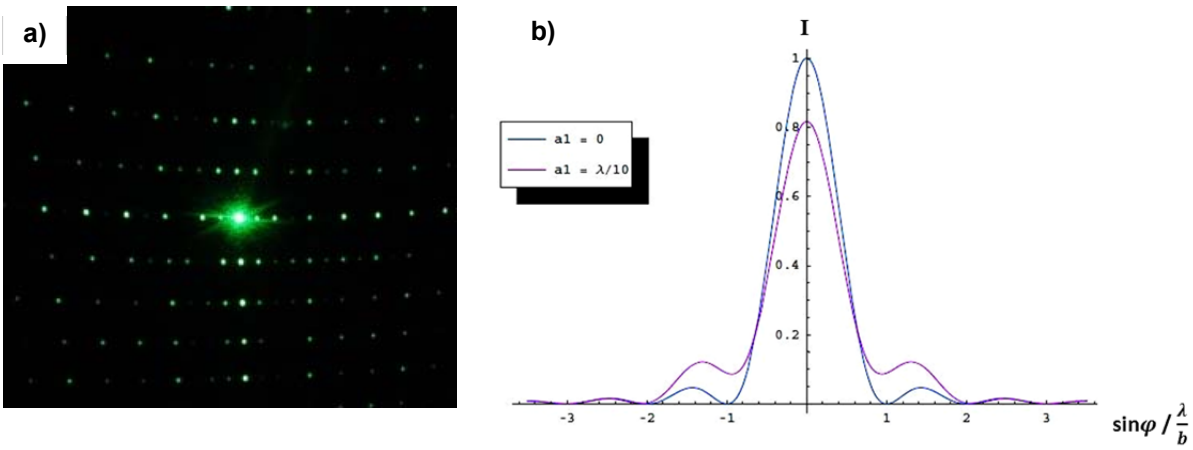

Fig. 24: a) 2-D Fraunhofer diffraction pattern (far field) resulting from a SLM irradiated at 532nm, b) intensity distribution of the diffraction pattern from a planar (blue) and curved micro mirror (violet) with bow = λ/10 (the simulation was done by a college at IPMS)

Deflectometer:

The so called deflectometer is a measurement station, initially designed for the analysis of micro mirror deflection and determination of the resonance frequency. The measurement principle is to detect the position of a micro laser spot that is reflected from a single mirror. In both cases of mirror deflection and mirror bowing the position of the reflected beam on a position sensitive detector (PSD) is slightly changed and analysed (fig. 25). However, the width of the laser beam in the sample plane is of several microns and does not provide a sufficient spatial resolution within the investigated mirror.

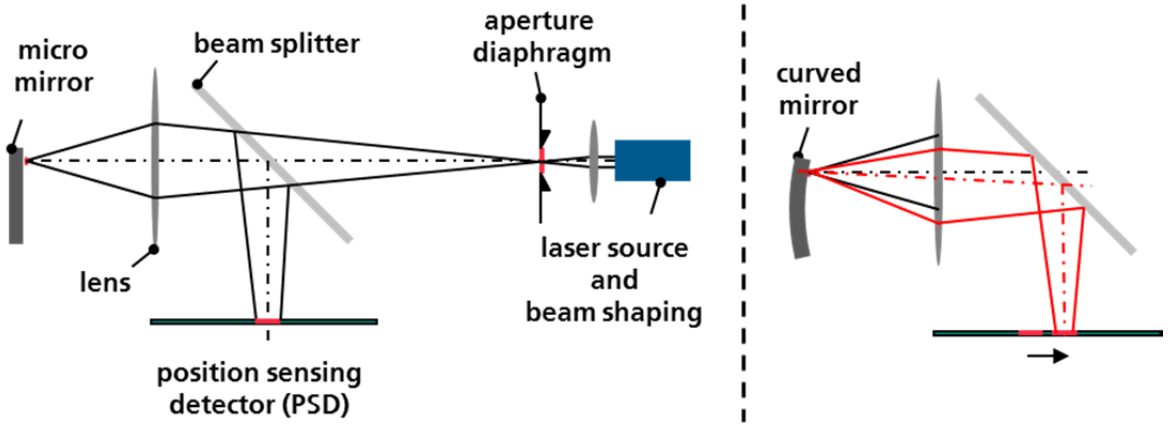

Fig. 25: Mirror bow measurement with the "deflectometer", initially designed for mirror deflection analysis

Interferometry/ phase-shift interferometry:

Compared to static interferometry with a possible resolution of ≈ λ/ 10 the use of the phase-shift principle, including the analysis of phase-shifted series of fringe patterns, provides a resolution in z-direction of up to λ/ 1000 [41]. The areal characterization of a single mirror with several hundreds of data points allows a substantial description of the mirror topography.

MEASUREMENT METHOD:	**PROS/ CONS:**	
diffraction pattern analysis	pros:	- simple setup design, no additional hardware except a detector - similar to the real mode of operation
	cons:	- intensity distribution of the diffraction pattern is affected by different parameters e.g. the statistical mirror deflection/ pre-deflection and the mirror topography - separation of these mix of effects is necessary - minimum resolved bow change was uncertain
deflectometer	pros:	- setup was already available - saving of time for the design of a new setup

	cons:	- allows the investigation of just one mirror at a time -laser spot size of several microns allows just a few data points per mirror - minimum resolved bow change ≈ 5nm
phase-shift interferometer	pros:	- possible resolution in z-direction of ≈ λ/ 1000 - substantial description of the mirror topography by several hundred data points per mirror
	cons:	- time consuming design and characterization of a sophisticated setup

Table 3: Pros and cons of different measurement methods

After considering all requirements and balancing pros and cons, the decision was made to design a phase-shift interferometer for the investigation of the effect of laser light on the micro mirror topography.

1.6.3 Phase-shift interferometry

The technique of temporal phase measurement, also known as phase-shift interferometry (PSI), was already used by Carrè in 1966 [42]. The development of solid-state detector arrays and faster microprocessors in the 1970s enabled its wide practical use. PSI allows determining the phase of a wavefront directly from recorded intensity data. For this purpose, a relative phase shift between object and reference beam is applied and a series of phase-shifted interferograms is generated. A detector senses the resulting fringe pattern for each position. Finally, the surface map of the area of interest is achieved by calculating the optical path difference (OPD) for each pixel of the detector. Compared to static interferometry, where a single fringe pattern is analysed, the systematic modulation and measurement of the phase improves the interferometer's resolution limit to the range of λ/1000 [41].

The phase-shift between both arms of the interferometer can be applied by several techniques, see [43]. In the present experiment, a piezoelectric actuator is used that shifts the sample in discrete steps of π/2 regarding the measurement light wavelength. In PSI there are various algorithms in order to calculate the shape of an optical surface by means of recorded intensity data. These algorithms usually differ in the number of frames (fringe patterns), the length of

the introduced phase-shift and whether the length is known or unknown, the maximum length of detectible phase steps on the sample (modulo π or modulo 2π) and their sensitivity to phase shift error. For the reconstruction of the wavefront phase in PSI a minimum of three intensity measurements is required.

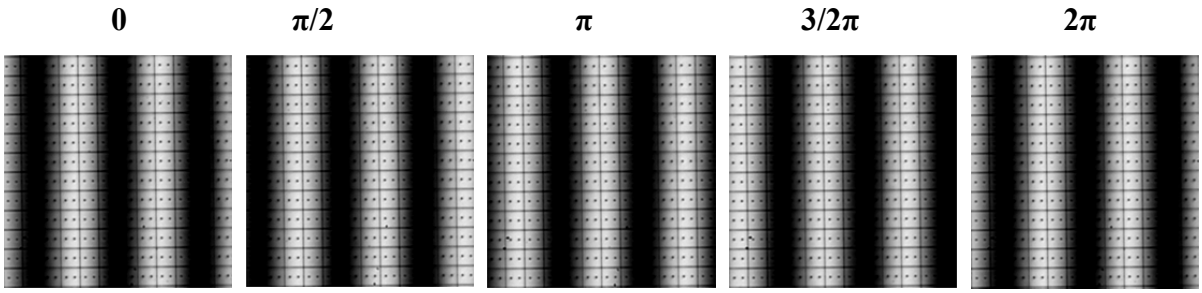

Fig. 26: Sample surface overlaid with fringe pattern. From frame to frame a phase shift of π/2 is introduced, resulting in an overall phase-shifted of Δφ = 2π.

First algorithms were using four and three frames respectively. Later on, algorithms with six and more frames were developed to compensate environmental effects on measurement results [41, 43]. Figure 26 shows a series of sample pictures with the single mirrors clearly visible, overlaid with a fringe pattern. The phase-shift between each frame is π/2, resulting in an overall shift of 2π between first and last frame. When the wavefront phase $\varphi(x,y)$ is known the real optical surface can be determined dependent on λ the centre wavelength of the illuminating light source and on θ and θ' the angle of incidence and of reflection (equ. 13a). In the present case with perpendicular incidence equ. 13a is simplified to equ. 13b [41].

$$\textbf{(a)}\ H(x,y)=\frac{\varphi(x,y)\ \lambda}{2\pi\left(\cos\theta+\cos\theta'\right)} \qquad \textbf{(b)}\ H(x,y)=\frac{\varphi(x,y)\ \lambda}{4\pi} \qquad \textbf{(13)}$$

H(x, y) = surface height, φ(x, y) = wavefront phase, λ = centre wavelength of the illuminating light source, θ = incidence angle of the measuring bundle of rays coming, θ' = angle of reflection

Details of the procedure to turn the wavefront into the OPD map e.g. the "Phase Unwrapping" go beyond the scope of this chapter but can be found in [41] or in [44][12]. In the present experiment a commercially available software (IntelliWave) is used for calculating the wavefront and OPD map. The algorithm that is chosen is developed by Schmit and Creath and is based on a series of five frames (equ. 14) where I_1, I_2, I_3, I_4 and I_5 equal the recorded intensity data

[12] [44 – p. 122]

for phase-shifts of 0, π/2, π, 3/2π and 2π [45]. Compared to algorithms with less than five frames this one is more time consuming but less sensitive to phase-shift error.

$$\varphi(x,y) = \tan^{-1}\left(-\frac{-I_1 + 4I_2 - 4I_4 + I_5}{I_1 + 2I_2 - 6I_3 + 2I_4 + I_5}\right) \quad \textbf{(14)}$$

The series of phase-shifted interferograms from above is turned into the OPD map which shows the real sample surface in false colours with the colours scaling the height profile. Post holes and slots between the mirrors are clearly visible (fig. 27).

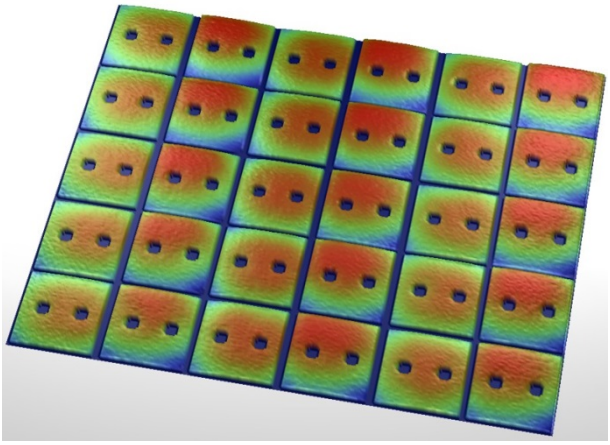

Fig. 27: Series of phase-shifted interferograms from above is turned into an optical path difference map that shows the real sample surface in false colours with the colours scaling the height profile.

2 Design and characterization of the Phase-Shift Interferometer

2.1 Interferometer design

Sample dimensions in the range of some micrometre require a sufficient magnification of the surface topography. For this reason, the instrument is a combination of an interferometer and an optical microscope. The main elements of the designed instrument are:

- Illumination device (light source and Köhler illumination)
- Imaging device (interferometer objective, tube lens, beam splitter)
- Phase shifter
- Image detector (see fig. 28)

Additional hardware:

- Optical table with vibration damping
- Optics for beam guidance and beam shaping of laser light
- Housing of the interferometer against ambient conditions

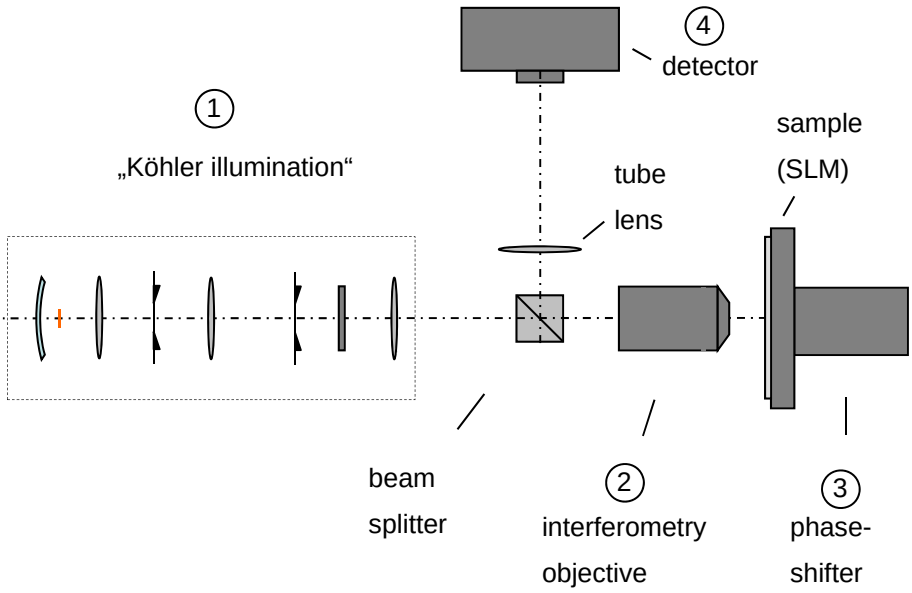

Fig. 28: Interferometer design with the four main elements: illuminating device, imaging device, phase-shifter and image detector

Illumination device - light source

A halogen bulb for optical microscopes is used as light source. In combination with a band pass filter the emitted spectrum is restricted to 650nm ± 5nm and the coherence time of transmitted light is increased to 10^{-13}s. This results in an optical path difference between both arms of the interferometer of 30µm in maximum to still enable interference [51][13]. The band-width of the filter is a compromise between irradiance and coherence time of the transmitted light. In general a sufficient coherence time is required to get fringes with high contrast when adjusting the interferometer.

Illumination device - Köhler illumination

A fundamental element of each optical microscope is the illuminating device. Such a device, usually designed according to August Köhler enables a nearly homogenous illumination of the sample, and optimizes image contrast and resolution. The Köhler illumination was initially designed for transmitted light configuration and consists of two collecting optical systems (collector and condenser lens) and two diaphragms (aperture and field diaphragm) [52]. The illumination device in fig. 29 shows elements and optical paths of the designed Köhler illumination for incident light and infinity corrected configuration. There are two additional lenses and the objective itself is used as the condenser lens.

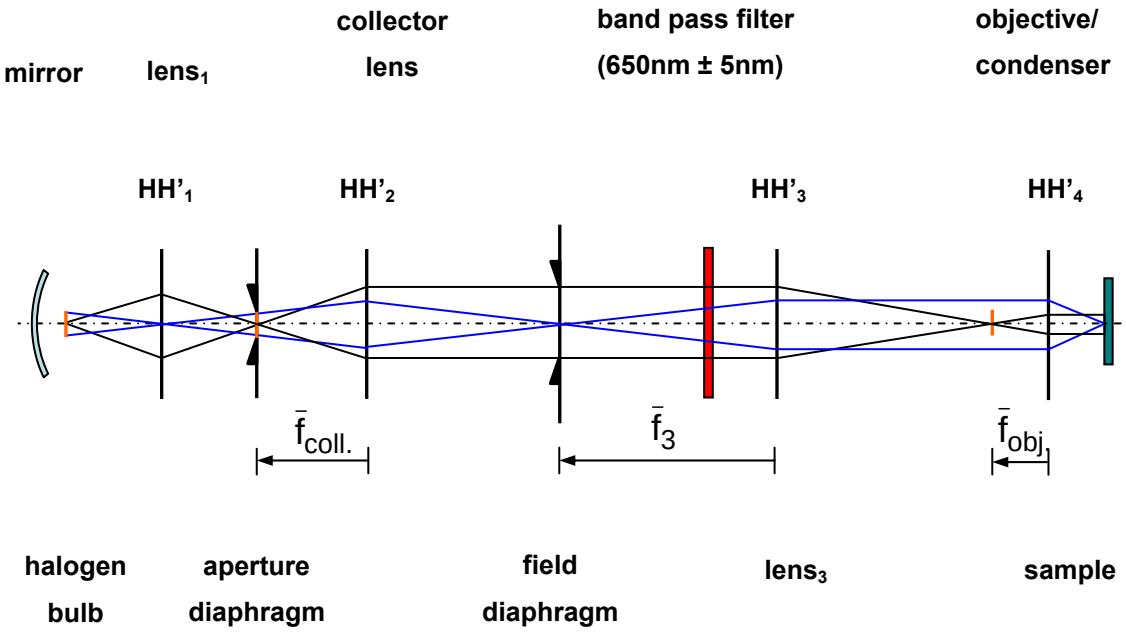

Fig. 29: Köhler illumination for incident light and an infinity corrected configuration

[13] [51 – p. 412]

Imaging device

The imaging device consists of the interferometer objective (NA= 0.3, $f'_{obj.}$ = 20mm, wd = 7.4mm), beam splitter and tube lens. The objective creates an image at infinity which is transferred by the tube lens into a real image localized in the tube lens focal plane (fig. 30a).

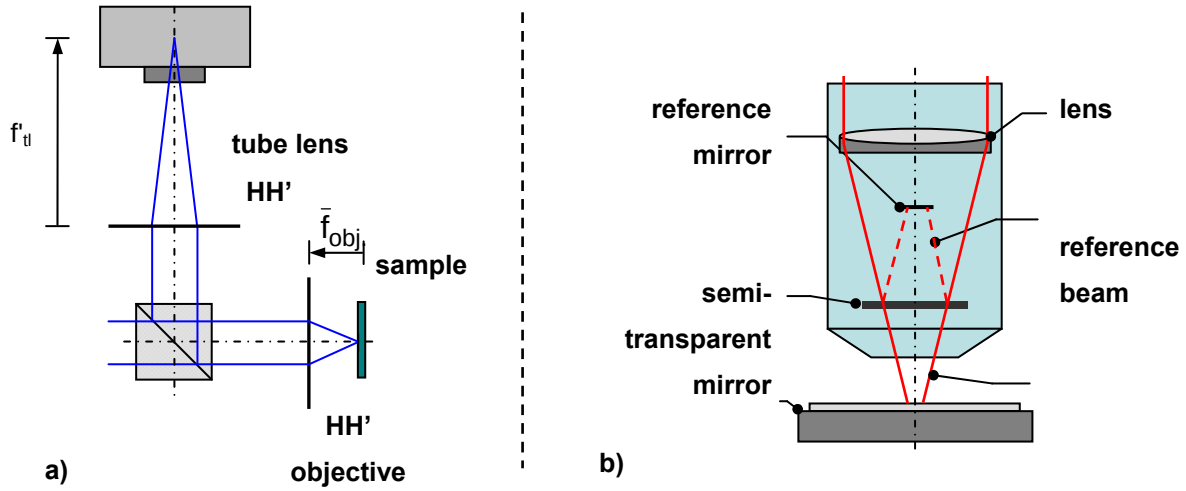

Fig. 30: a) Imaging device with the interferometry objective (infinity configuration), tube lens, beam splitter and image detector; b) working principle of the Mirau-type interferometer objective

The total magnification of the optical microscope is determined by the ratio of focal distances of tube lens and objective, (equ 15). With f'_{tl} = 400mm the total magnification of the instrument is 20x.

$$\Gamma'_M = \frac{f'_{tl}}{f'_{obj.}} \qquad \textbf{(15)}$$

Γ'_M-total magnification, f'_{tl}-focal distance tube lens, $f'_{obj.}$-focal distance objective

The interferometer is of the Mirau type. It is realized by a semi-transparent mirror in front of the lens that splits the light in object and an internal reference beam (fig. 30b). Due to the recombination of reference and object beam the image gets superimposed by a fringe pattern.

Phase shifter

The phase-shift is realized by a piezoelectric actuator (P-753.11C LISA by PI). It is equipped with a capacitive feedback sensor for control of the current actuator position. It allows a maximum travel of 12µm and shows a linearity of 0.03 % in closed loop.

Image detector

As image detector a CCD camera (CCD-4000UV by Vosskühler) is used. The camera has a bit depth of 12, a pixel size of 7.4µm * 7.4µm and a resolution of 2048*2048 [53].

2.2 Complete experimental setup

The complete experimental setup is shown in fig. 31. It includes the excimer laser (KrF) as light source emitting at 248nm, the attenuator for alignment of the energy level, UV-optics for beam guiding and beam shaping, a vibration isolated optical table, the interferometer and housing of the interferometer as protection against ambient conditions. Furthermore, there is a motorized translation stage and some precision mechanics for adjustment and focussing of the sample with respect to the interferometric beam path.

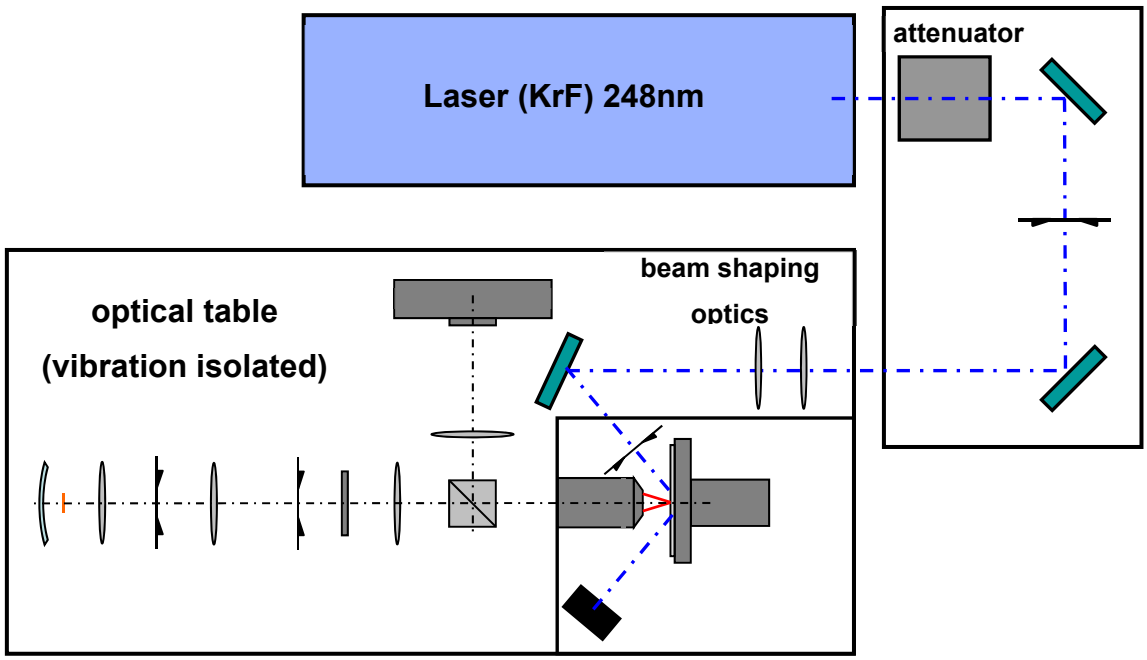

Fig. 31: Complete experimental setup: laser (KrF), attenuator, optics for beam guiding and beam shaping, interferometer, vibration isolated optical table, housing against ambient conditions

In normal operation the SLM is irradiated perpendicularly that means at 0°. For the irradiation experiments and according to the interferometer design it is necessary to change the angle of incidence to 55°, fig. 32. This results in a decrease of the reflectance of the mirror material. For aluminium covered with an oxide layer of 5nm the reflectance changes from 91% to about 88%, see fig. 18.

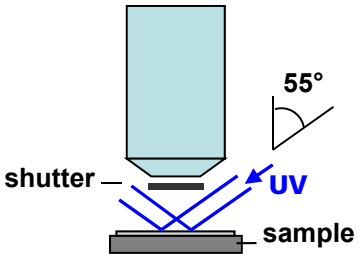

Fig. 32: Irradiation of the sample with an incidence angle of about 55°

2.3 Control and automation

A measurement cycle consists of the following sequence of activities: opening the shutter that protects the lens from laser light, focussing of the sample, capturing the data, data transfer, phase shift, repetition of the loop for 4 times and finally closing the shutter, see fig. 33. Except the focussing procedure, the sequence is carried out automatically. For this purpose a script is created in Labview which controls the hardware and handles the measurement data.

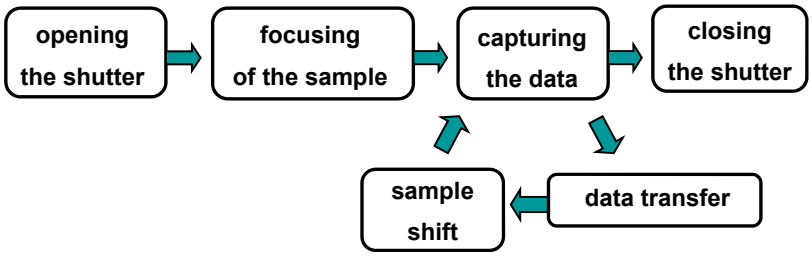

Fig. 33: Sequence of the measurement cycle

The following hardware components are controlled by the Labview script which reduces the duration for running the sequence to just a few seconds (< 5s): power supply for opening and closing the shutter, frequency synthesizer for the actuation of the piezo transducer and camera.

2.4 Characteristic parameters of the interferometer

The following chapter is focusing on parameters that describe the interferometer's optical performance. At first, the instrument's coordinate system with the axes x, y and z needs to be defined. The sample surface is situated in the plane spanned by x and y. The z axis is perpendicular to x and y and contains the height information.

The measuring range:

The lateral measuring range of an optical microscope is defined by the field of view of the used objective. For the present instrument the lateral range is limited by the dimensions of the image detector (15.2mm * 15.2mm). The measuring range of the z-scale runs from the instrument's resolution limit of about 1nm up to a maximum step height of λ/4. With a central wavelength of 650nm maximum step heights of $\Delta H_{\max} = 162\text{nm}$ can be detected. The λ/4-limit results from a maximum phase shift of $\lambda/2$ that still can be allocated to an explicit height difference. Larger phase shifts can be caused by different height differences and result in unwrapping error. The same limitation has to be considered for phase shifts resulting from slopes or sample tilt.

Sampling of lateral details

The sampling rate for lateral details is determined by the pixel size of the image detector and the total magnification of the microscope. With a pixel size of 7.4µm and a total magnification $\Gamma'_M = 20$ the lateral sampling rate equals $7.4\mu m / \Gamma'_M = 0.4\mu m$. A sample detail like the gap between the mirrors with a width of 0.5µm is detected by just a single detector pixel and is rarely visible in the height profile.

Sampling of fringes

For a successful sampling and reconstruction of the wavefront's phase the Nyquist frequency has to be considered by sampling the fringes. This means, that single fringes have to be detected with at least two detector elements. Otherwise undersampling and aliasing effects occur. Within the present experiments the sample was adjusted that way with 4-5 interference fringes visible. Thus, a single fringe was sampled by about 400 detector pixels.

Lateral resolution limit

The resolution for a diffraction limited optical system can be defined by the general Rayleigh criterion. For an optical microscope with an illuminated sample the resolution limit is usually indicated in dependence of the used central wavelength and the numerical aperture of illumination and imaging beam path, see equ. 16 [54][14]. With λ = 650nm and $NA_{ill.}$ = $NA_{im.}$= 0.3, lateral details of 1.1µm can be resolved.

$$y_{\min} = \frac{\lambda}{NA_{ill.} + NA_{im.}} \qquad \textbf{(16)}$$

y_{min}-minimum resolved detail, λ-central wavelength, $NA_{ill.}$, $NA_{im.}$-numerical aperture of illuminating and imaging beam path

Resolution of minimum height differences limited by the quantization error

In PSI the resolution in z-direction is ideally limited by the analog-to-digital data conversion of the image detector. For this assumption it is required that the measurement is free of any external disturbance or other internal noise and the resolution of minimum height differences depends on the bit number of the detector, see equ. 17 [55][15].

$$\Delta H_{\min} = \frac{\lambda}{2\pi} * \Delta\varphi_{\min} \qquad \textbf{with} \qquad \Delta\varphi_{\min} \approx \frac{2\pi}{2^n} \qquad \textbf{(17)}$$

ΔH_{min}-minimum step height, $\Delta\varphi_{min}$-minimum phase angle, λ-centre wavelength, n-detector's bit number

A camera with n = 12bit and a centre wavelength of 650nm allow a minimum step height $\Delta H_{\min}$ = 0.16nm. However, this is just a theoretical assumption.

Fringe modulation (contrast) and focussing of the sample

The use of a broad band light source requires a certain control of the fringe modulation. To receive high contrast fringes sample and reference mirror should have similar reflectance and the image detector should be used to full capacity of its bit number. Furthermore, the optical path difference between object and reference beam needs to be minimized. That means the sample focussing has to be carried out very precisely. Figure 34 shows the effect of defocusing on the fringe modulation. Around the zero position of the z-axis there is a zone of best

[14] [54 – p.151]
[15] [55 – p.102]

modulation of about ±2λ (±1.3µm). Beyond that the modulation decreases clearly. To achieve fringes with maximum modulation it is necessary to align the sample within the best focus range. This is realized by aligning the sample first roughly with a motorized translation stage and then by shifting the sample stepwise in steps of λ/2 with the piezo actuator around the assumed focus position. With the histogram of the image detector the fringe modulation on a certain z-position is monitored and the focus position is determined precisely.

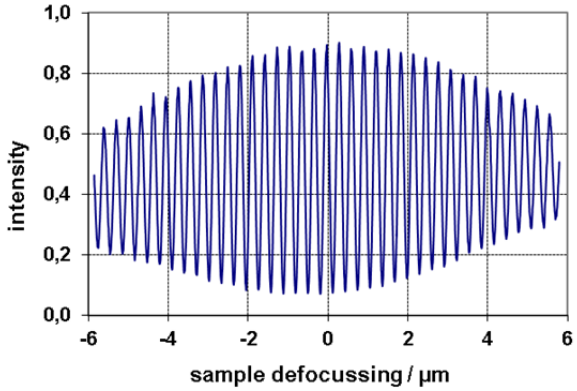

Fig. 34: Effect of defocusing on fringe modulation

2.5 Measurement error analysis

2.5.1 General sources of measurement error in PSI

General sources of measurement error of PSI are described in [56]. At this, error sources like phase-shift error, detector nonlinearities and quantization errors are responsible for systematic measurement errors. Error sources like mechanical vibrations and air turbulences result in random measurement errors.

The systematic error of any PSI should ideally be determined by the quantization error, resulting from the analog-to-digital data conversion of the detector. But this limit is rarely ever reached because other error sources usually occur more intense. Mostly it is the phase-shift error, originating from different sources, which is the dominating error source at all. In the present case, the phase-shift is realized by a piezoelectric transducer with a capacitive feedback sensor and a very high linearity of 0.03%. Thus, phase-shift error introduced by a nonlinear phase-shifter can be neglected. It is assumed that the phase-shift error introduced by mechanical vibrations and air turbulences as well as the sensitivity of the used algorithm to this error is the dominating error source of the interferometer [56]. Additionally to the standard error sources we need to consider phase-shift error introduced by laser induced sample drift. Laser induced heating of the sample causes such a drift especially at the beginning of the irradiation and of the relaxation cycle. In this way at higher energy levels the phase-shift can be disturbed significantly.

2.5.2 System aberrations

Depending on the type of instrument aberrations can have static and dynamic parts. Here, static aberrations include optical aberrations from all optical components and the surface characteristic of reference mirror and optical flat. Additionally there are dynamic aberrations due to measurement noise and the effect of ambient conditions. A superposition of all aberrations being present is shown in fig. 35. The picture is gained by measuring the surface of an optical flat in terms of a si-waver covered with a thin layer of aluminium. The depicted result contains both static (systematic) and dynamic (noise + ambient conditions) instrument aberrations. The topology of the detected optical flat itself is unknown. Hence it is not possible to identify the particular source or to distinguish between different types of the detected aberrations.

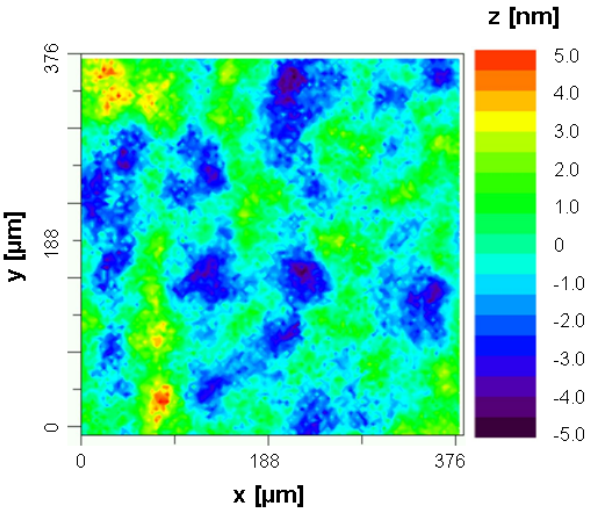

Fig. 35: Measurement of an optical flat (si-wafer), representing the superposition of all system aberrations being present. Detected profile shows a roughness of R_{RMS} = 1.3nm.

The detected profile shows a roughness of R_{RMS} = 1.3nm. Assuming that the effect of dynamic aberrations (mostly ambient conditions) is of the same order of magnitude, all future measurements will be superimposed by these aberration pattern and will exhibit a $R_{RMS} \geq 1.3$nm. Usually it is a standard procedure in metrology to determine the systematic aberrations once in a while and to subtract them from the respective sample. But due to the presence of dynamic aberrations this procedure seems not to be useful in the present case.

2.5.3 Random error - measurement noise

Noise in general is defined as an additional internal signal with the measuring system ideally being in an undisturbed environment. In the present experiment the influence from ambient conditions can be minimized but it is almost impossible to completely separate them from the interferometer's internal noise. For this reason, the repeatability of the generated measuring data (random error) contains both, internal and external error sources. It is assumed that a phase-shift error introduced by external ambient conditions and the focussing accuracy of the sample are the limiting factors for the minimization of the random error. For the determination of the random error a calibration standard with a step height of 97.4nm etched in chrome is used. The standard deviation from the detected arithmetic mean after 20 cycles is ±0.1nm, see fig. 36.

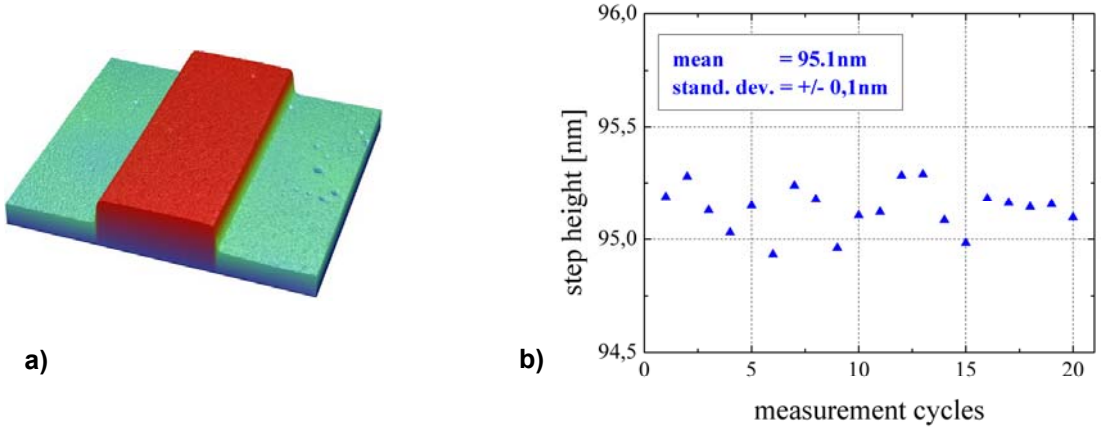

Fig. 36: Determination of the random error of measurement a) used step reference in chrome with a step height of 97nm, b) detected step height with mean = 95.1nm and a standard deviation of ± 0.1nm

Furthermore, the random error is investigated by measuring an array of unreleased mirrors, which means, they are not separated from the underlying spacer material. Thus it can be ensured, that the mirrors will not change their surface texture during the long-term measurement. The result is shown in fig. 37 with the averaged bow of 500 mirrors showing an arithmetic mean of 0.1 nm and a standard deviation of 0.02nm.

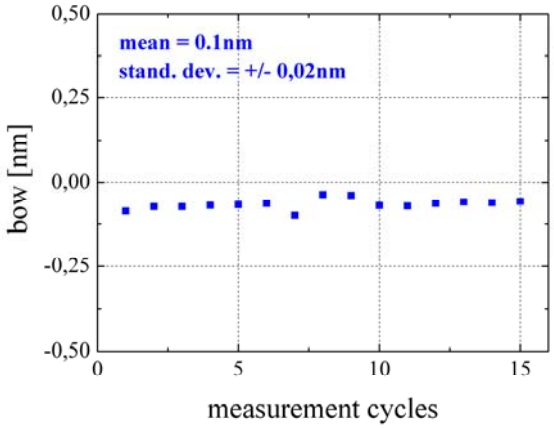

Fig. 37: Determination of the random error of measurement by means of an array of unreleased (fixed) mirrors

2.5.4 Systematic error - amplification and linearity of the z-scale

The correlation between a measured quantity and the real quantity of any measuring instrument is defined by its transfer function. This function can be used for alignment purpose and for correction of the measurement results. An ideal transfer function would be a straight line and shows a slope of one which means that the measured quantity equals the input quantity. The instrument's real transfer function shows the deviation of the detected to the input quantity [57].

certified step height/ nm	**detected step height/ nm**
9 ± 0.5	8.8 ± 0.3
46.9 ± 1	46.0 ± 0.14
97.4 ± 1	95.1 ± 0.1
transfer function:	f(x) = 0.98x + 0.3
amplification coeff.:	0.98
linearity:	0.46

Table 4: Certified step heights of the used calibration standards and step heights measured by the interferometer

For this purpose, different calibration standards with step heights of 9nm, 46.9nm and 97.4nm were measured. The step heights measured by the interferometer are listed in table 4. Within the investigated measuring range from 9nm to 97nm the interferometer shows a mean deviation from the ideal case of -0.02 resulting in an offset of the measured data of -2% (see fig 38a). This offset could get compensated but so far has not been considered necessary.

2.5.5 Additional noise under laser exposure

As previously discussed, the laser induced heating during an irradiation at higher energy levels causes a mechanical drift of the entire SLM of several microns. The higher the laser energy the higher is the effect on the irradiated sample. The phenomenon occurs at the very beginning and subsequent to an irradiation until the sample apparently reaches thermal equi-

librium. The sample drift causes an additional phase-shift error and results in an uncertainty during the focusing procedure. And finally it worsens the repeatability of the generated surface data. To estimate the effect on the random error of measurement, a calibration standard is irradiated (at 10mJ/cm^2, 1kHz) and the measurement of the random error is repeated (fig. 38b). The sample drift causes a slight shift of the detected mean (46.4nm) and an increase of the standard deviation (±0.4nm). Hence there is a certain effect by the laser induced sample heating. But once the sample reaches thermal equilibrium the effect attenuates and seems not to be significant especially during long-term experiments.

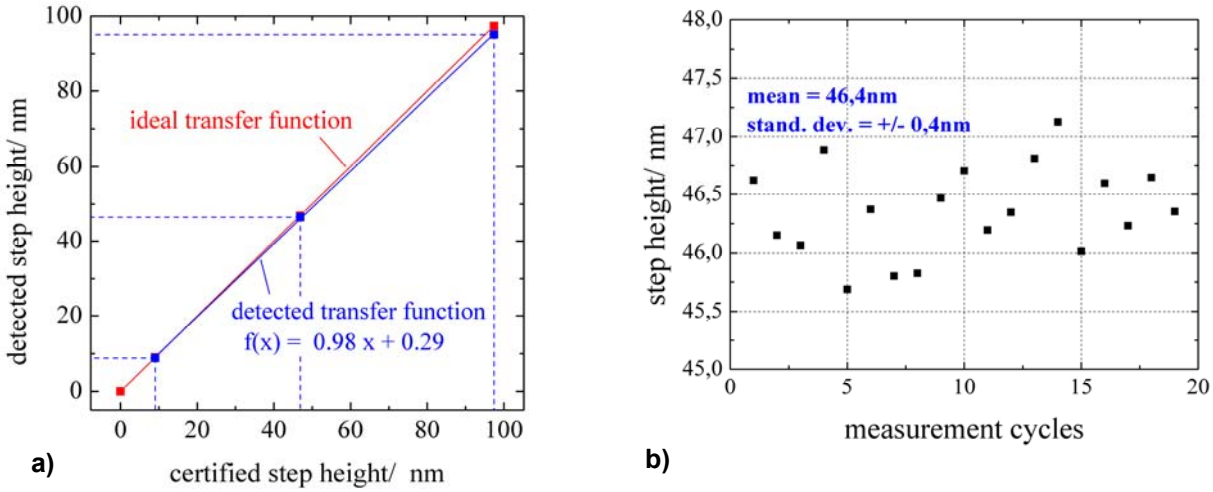

Fig. 38: a) Detected transfer function of the interferometer with amplification coefficient = 0.98 and linearity = 0.46, b) Determination of the random error of measurement of an irradiated sample, detected step height with a mean = 46.4nm and a standard deviation of ± 0.4nm

3 Laser irradiation of SLMs at 248nm

3.1 Characterization of material properties or devices?

A fundamental question of the present thesis is whether the results show typical properties of the investigated mirror material or whether they show the specific behaviour of a few investigated samples. Is it generally possible to separate the experimental results from an influence of specific devices? No, it is not. Of course, the experiments contain device dependent results, especially when it is about such a complex system like a highly integrated optical MEMS.

What are the factors that might introduce differences in the device performance?
By comparing samples from different positions on a wafer, there are circular fluctuations in the sputtered layer thickness. Hence, slight differences in the mirror thickness can occur. By comparing samples, fabricated in different lots, the performance might be affected by the use of different sputter targets or the application of different thermal loads.

How is this problem handled within the thesis?
First of all, a study was carried out to figure out settings and parameters that have an impact on the detected bow change and to realize stable experimental conditions. During the experiments settings and the course were documented carefully. Each specific series of measurement is always carried out several times and by the use of different samples. During the investigation of a certain irradiation parameter, like the pulse energy, only samples from a certain lot were used. All in all more than 20 devices were used within the following investigations.

Any effect which is depicted in one of the many figures and discussed in the running text is a real phenomenon. Only these were depicted, which were reproduced during several series of measurements.

3.2 Procedure of the measurement data analysis

3.2.1 From surface data to the single mirror bow

Generation of surface data and recognition of single mirrors

The following section describes the procedure of the measurement data analysis. After the data acquisition itself the height profile of the sample is calculated with a commercial available software (IntelliWave). The resulting OPD map is presented in fig. 39a below. This closed surface passes through another software to recognize each single mirror and to separate the mirrors from the surrounding slits and the two post holes (fig. 39b). This step is necessary otherwise the mirror edges would be superimposed by disturbing spikes from light coming out of the slits and the post holes[16].

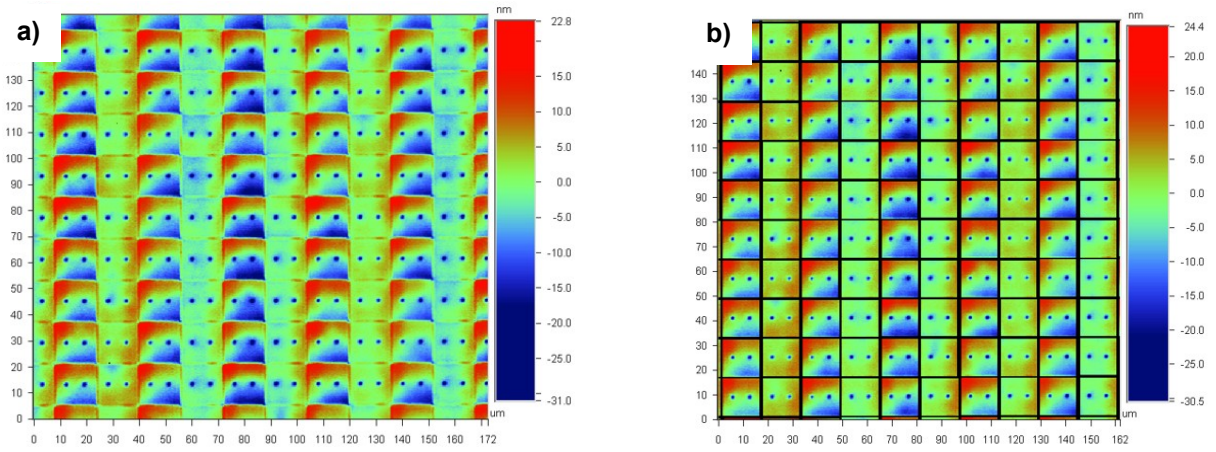

Fig. 39: a) OPD map calculated from the acquired intensity data, b) Recognition of each single mirror and separation from the surrounding slits and post holes

Topography of a single mirror

The topography of a single mirror prior to any laser irradiation is shown in fig 40a, b. The cross section in fig 40a shows a mirror which is slightly curved along its x-axis and a positive bow of 4nm. Remember the definition of the mirror bow on p.31. Additionally the mirror shows a certain roughness, which is not quantified in this depiction. The same mirror shows again a certain roughness but no curvature along its y-axis (fig. 40b).

[16] The software for the mirror recognition is an existing tool at the IPMS and was not created within this thesis.

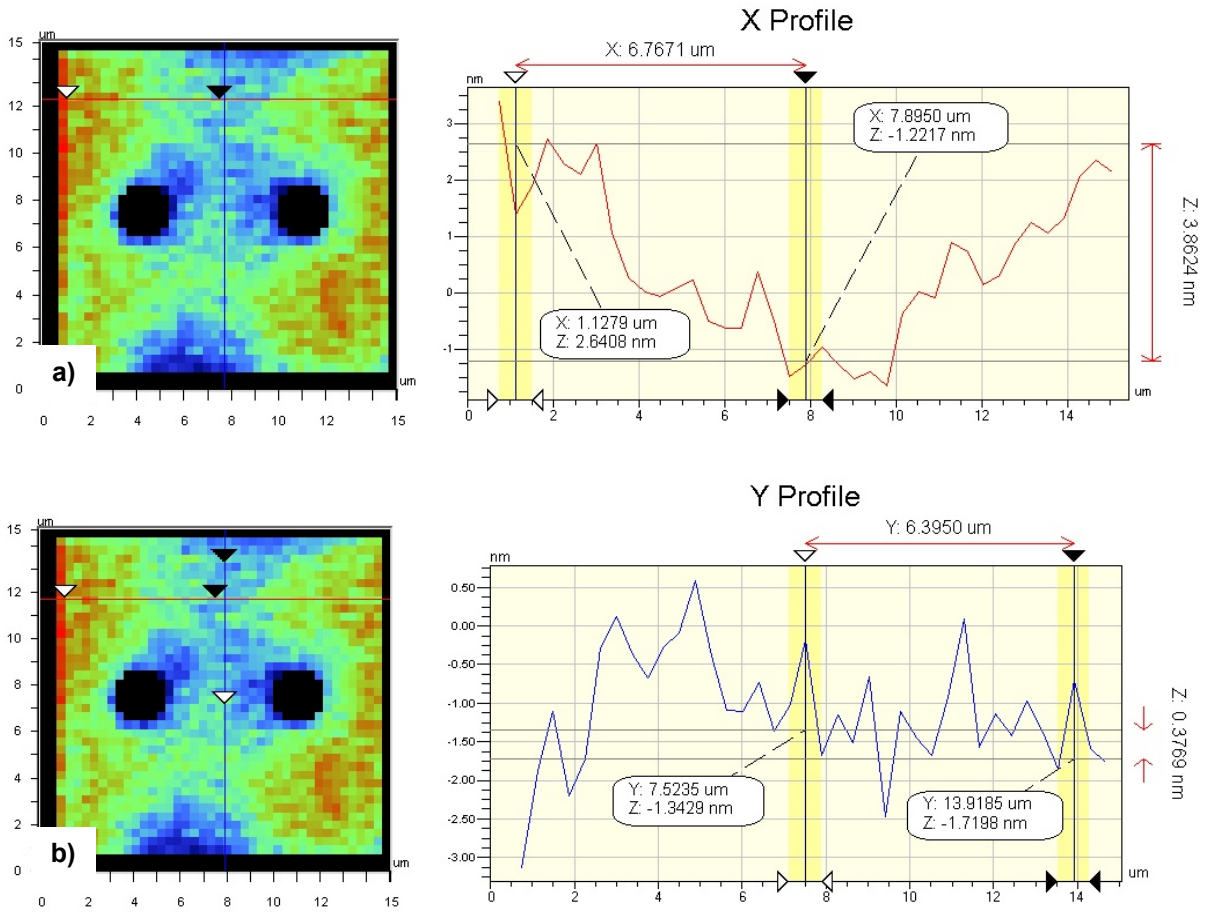

Fig. 40: Topography of a single mirror a) along its x and b) along its y-axis prior to any laser irradiation

The topography of a single mirror after a laser irradiation is depicted in fig 41 below. The mirror now shows a distinct curvature along both axes and the curvature has changed in negative direction. The bow along the x-axis is -9nm (fig. 41a), along the y-axis is -11nm fig. 41b.

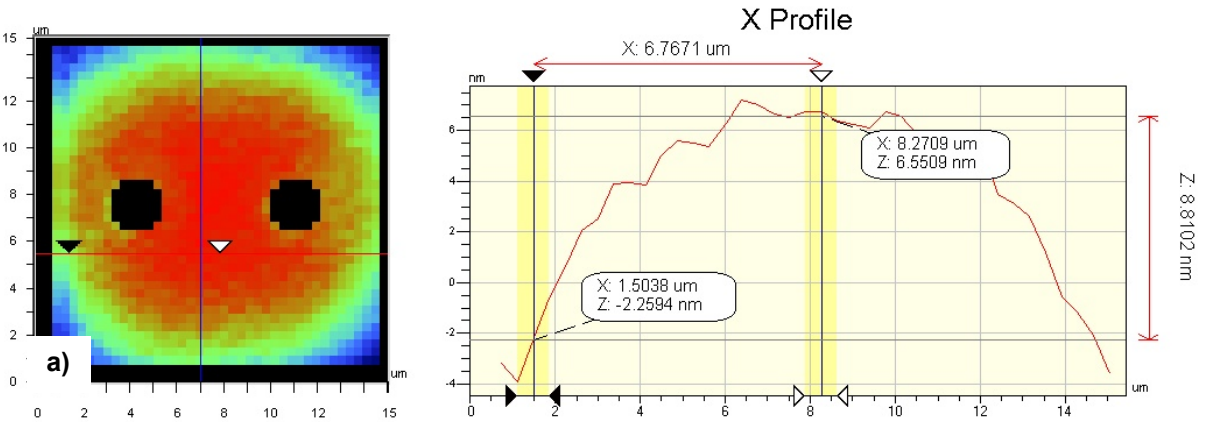

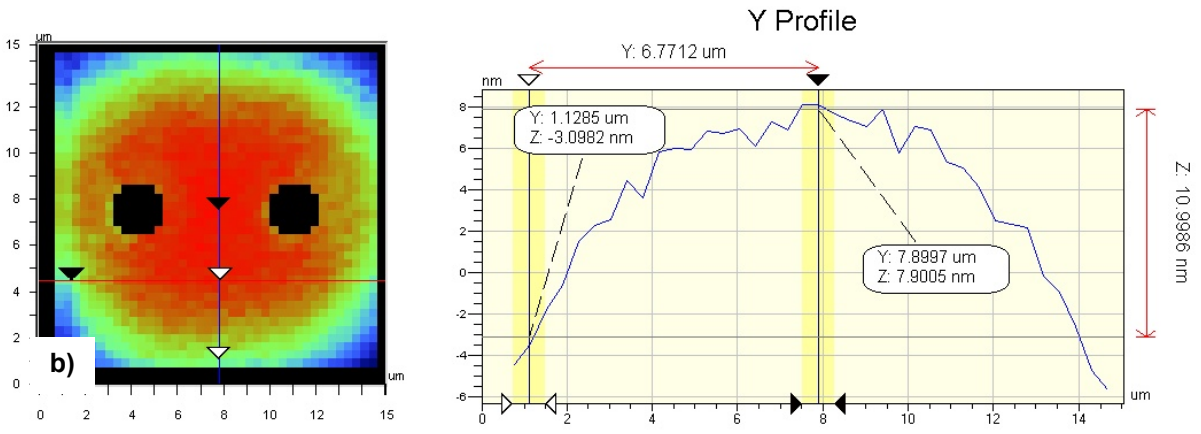

Fig. 41: Topography of a single mirror a) along its x and b) along its y-axis subsequent to a laser irradiation. Along both axes the mirror shows a distinct negative curvature.

3.2.2 Realisation of single and multiple measurement cycles

The following chapter describes the procedure of the in situ areal surface texture measurement. A single measurement cycle consists of three periods, including the measurement before (I), during (II) and after (III) the irradiation, see fig. 42a)

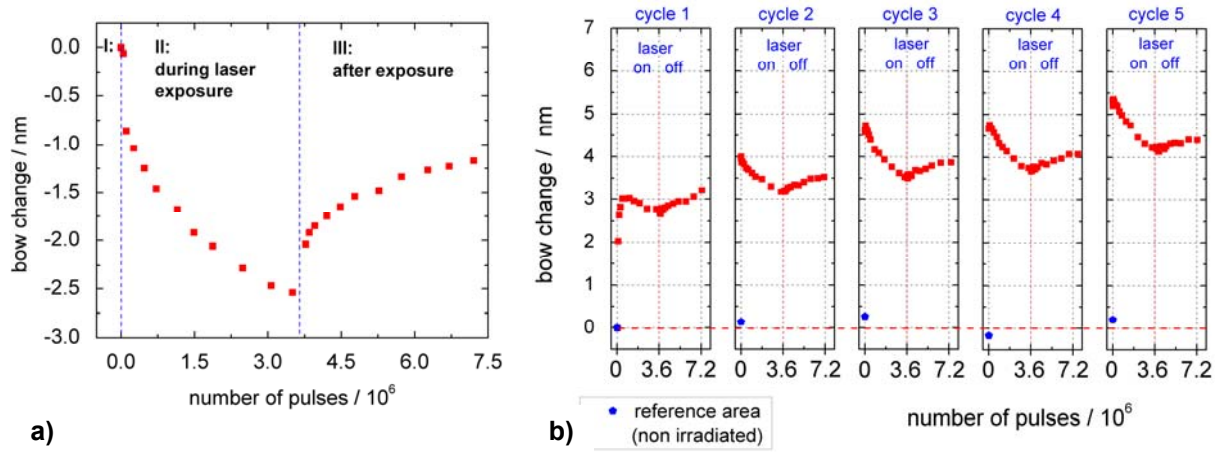

Fig. 42: a) Description of the insitu areal surface texture measurement procedure with measuring before (I), during (II) and after (III) the laser irradiation, b) presentation of measurement data when several irradiation cycles are carried out one after another with a break of one day after each cycle; blue data points show the reference measurement taken from an non-irradiated area in advance of each cycle

The y-axis shows the average bow change in nanometer of about 500 mirrors, defined as the respective area of interest. Remember the definition of the measurand “bow”, introduced in fig. 21 . The topography data in advance to the irradiation is defined as the initial state and is shifted to the zero position. The x-axis shows the applied number of laser pulses. Each of the periods II and III usually lasts one hour. For the investigation of the laser induced effect on the mirror bow a single measurement cycle shown in fig. 42a) provides a very limited amount of information. Therefore, series consisting of five of this single irradiation cycles were carried out at a certain set of irradiation parameters and on a certain sample position. Note that there is a break of one day between each cycle within the series. An example of such a series is presented in fig. 42b). The initial value of the first cycle is shifted to the zero position. The following cycles show the real bow change during the series with respect to the first cycle. In advance of each cycle a non-irradiated reference area

3.2.3 Averaging of mirror surface data

The investigations within the present thesis always show the effect of laser radiation to a group of many (ca. 500) micro mirrors. All presented results show the averaged data of the area of interest. Nevertheless it is useful to show the difference between single mirror and averaged topography data. Fig. 43a shows a histogram analysis with distribution and frequency of the single mirror bow of the investigated area of interest. The dataset belongs to fig. 42a, shown above and shows the first data point before the laser exposure. The mean is situated around 9.8nm.

As a comparison to the averaged dataset from above, fig. 43b shows the bow change from three individual mirrors from the same area of interest. As expected, the uncertainty of the individually data points is significantly higher. Nevertheless, the general tendency of a decreasing bow during the irradiation and a subsequent relaxation in the nanometer regime is clearly visible. Besides, due to the short scale of the y-axis of just 2.5nm the normal measurement noise gets visible already.

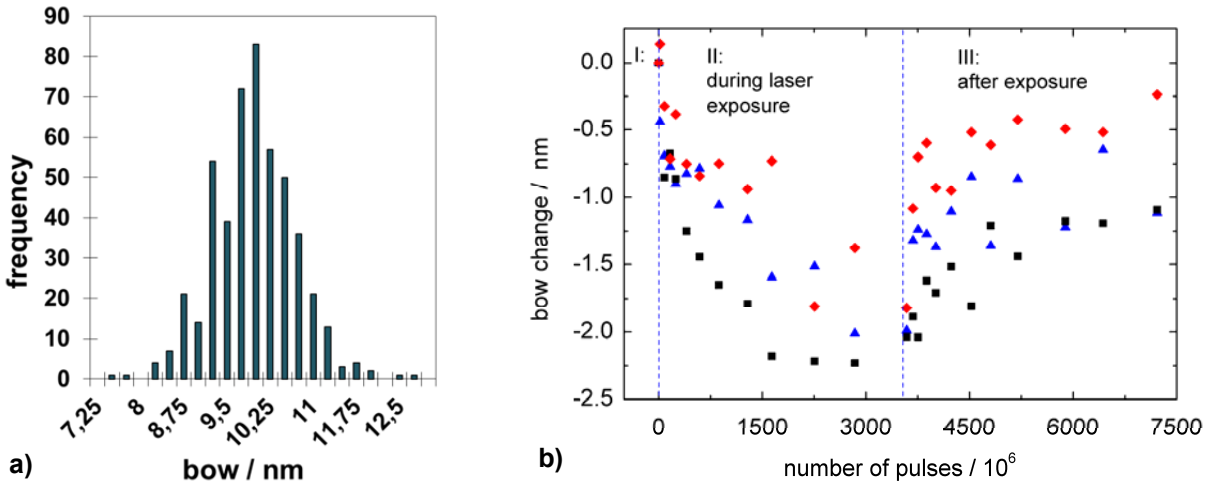

Fig. 43: a) Histogram analysis of the area of interest (500 mirrors), showing the distribution of the quantity bow, b) in situ areal surface texture measurement with analysing three single mirrors instead averaging of 500 mirrors

Resulting from the uncertainty of the single mirror data there is the question regarding the resolution of minimum bow differences in the averaged data set. What is the minimum bow difference that still can be distinguished from the variable behaviour of the single mirrors and from the measurement noise? Remember chapter 2.5.3, where the random error of measurement was determined by measuring an array of fixed mirrors. The standard deviation of the arithmetic mean was around +/- 0.02nm. Additionally we add two times the mean confidence interval of 0.07nm from the dataset in fig. 44, which corresponds to the confidence interval of each data point (averaged from 500 mirrors). Then we end up at an uncertainty of the averaged data set of about +/- 0.2nm. From this it follows, that averaged bow changes higher than +/- 0.2nm can be defined as real radiation induced effects in spite of the "single mirror uncertainty".

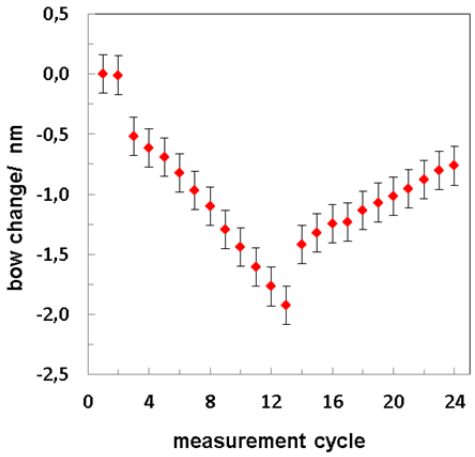

Fig. 44: Estimation of the resolution limit for minimum bow changes

3.3 Investigation of mirror bow as a function of different irradiation parameters

Within the following chapter a comprehensive study about the effect of UV-laser light on the micro mirror topography (mirror bow) is presented. The change of the mirror bow is represented in dependence of varying laser and irradiation parameters such as the energy density, laser repetition rate, pulse number and the ambient atmosphere. Additionally, first approaches will be discussed to give reasons for characteristic behaviour of the mirror topography under UV laser light.

3.3.1 Dependence of the bow change from incident energy density

Within the investigation of the energy dependent change of the mirror bow the following irradiation parameters where used, see table 5. Samples were irradiated at energy densities within the range from 10µJ/cm^2 – 30mJ/cm^2. The lower value is chosen where first laser induced effects are observed at all. The upper value is limited by the maximum energy density that can be realized within the experimental setup. The range from 10µJ/cm^2 to 1mJ/cm^2 is termed as "low energy". The range above this limit is termed as the "high energy" range. This classification is useful due to the different characteristic development of the mirror bow in the respective range.

energy density	**laser repetition rate**	**number of pulses**	**ambient atmosphere**
10µJ/cm^2 – 30mJ/cm^2	**1000Hz**	**5 * 3,6 10^6**	**N_2 ($O_2 \leq 1\%$)**

Table 5: Overview about the applied irradiation parameters

3.3.1.1 Bow change during the first irradiation cycle

During the experiments it turned out that for most of the applied energy levels the mirrors behave quite different during the first irradiation cycle compared to following cycles. That's why the change of the mirror bow during the first cycle is discussed in a separately.

In fig. 45a the change of the mirror bow in x-direction (remember the definition on p. 31) during the first irradiation cycle is presented for the "low" energy range. The diagram shows the bow change versus the applied number of laser pulses. Typically the curves do not show absolute values but the change from the initial value.

A cumulative change of the bow in positive direction is observed. A rising energy level results in a rising bow change. At this, the bow change is of permanent manner which means that there is no relaxation subsequent to the irradiation. After the irradiation the positive rise is even slightly ongoing. The results for "high" energy range are shown in fig. 45 b). It appears that after a few pulses and while the irradiation is ongoing, the initial positive development of the bow turns around and changes into the negative direction.

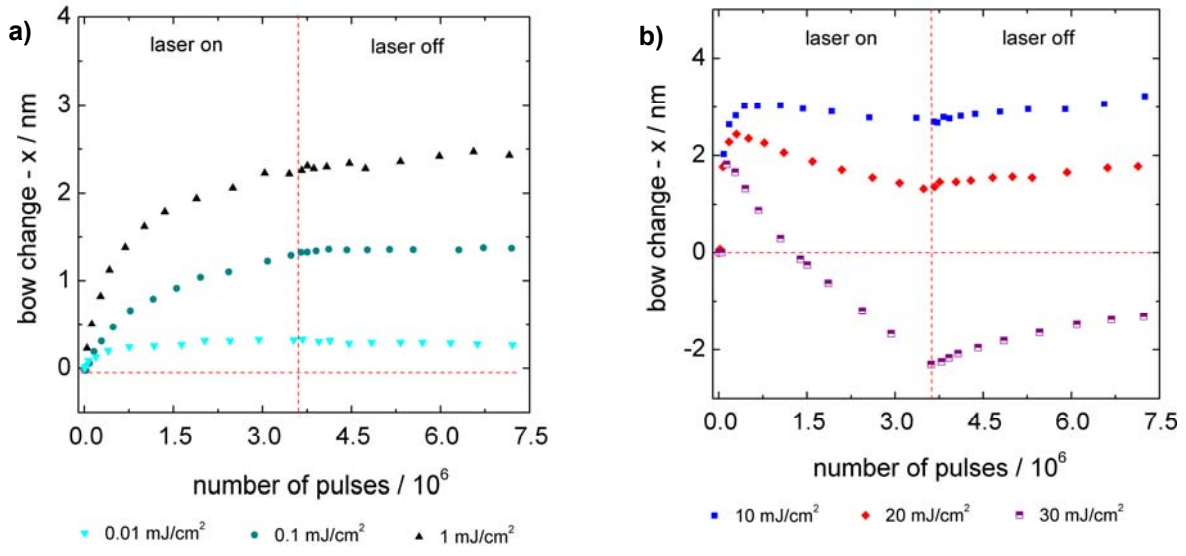

Fig. 45: Laser induced bow change in x-direction during the first irradiation cycle of a sample position for a) "low" and b) "high" energy densities

This turnaround is observed for energy levels from 10mJ/cm^2 and even more significant for higher levels. In case of the 30mJ/cm^2–series the curve even develops below the initial bow value before the irradiation started. Then, subsequent to the irradiation the bow develops slightly in positive direction for all energy levels applied.

In fig. 46a, b the same procedure is presented for the mirror's y-direction, which is along the tilting axis.

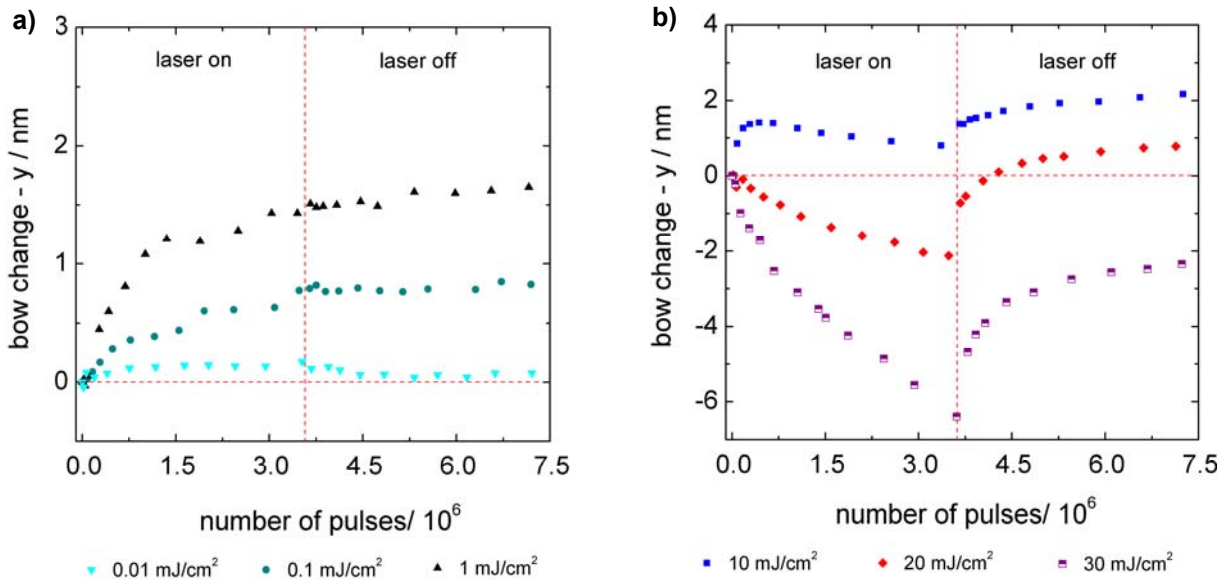

Fig. 46: Laser induced bow change in y-direction (tilting axis) during the first irradiation cycle of a sample position: a) "low", b) "high" energy densities

The change of the bow during the irradiation occurs almost similar with a permanent positive change for lower energy levels and the characteristic turnaround after a few pulses for higher energy levels. But now the turnaround occurs slightly earlier and even more significant. The 20mJ/cm^2 and 30mJ/cm^2 curves even develop in negative direction right from the beginning. This enhancement might come from the mirror's 2-post design. This phenomenon is discussed in detail on p. 99.

Conclusion

It is assumed that the change of the mirror bow is generally caused by at least two different effects. One of them causes a bow change in positive direction and seems to prevail in the "lower" energy range and during the first irradiation cycles. Another one causes a bow change in negative direction and seems to prevail in the "higher" energy range.

3.3.1.2 Bow change at “low” energy densities

The current chapter describes the bow change for “low” energy densities from 10µJ/cm^2 - 1mJ/cm^2. According to the description of the measurement procedure (p.54), the change of the mirror bow during five sequential irradiation cycles is presented. The diagrams show the change from the initial value versus the applied pulse number. Each cycle consists of a first half (3.6*10^6 pulses) with the sample being irradiated and a second half after the irradiation is stopped. After five cycles the number of pulses adds up to 18*10^6 totally. Fig. 47 shows the laser induced bow change in the mirror’s x-direction. Here, one observes a cumulative change of the mirror bow in positive direction. The rising energy level involves a rising bow change. The effect is of permanent manner and still slightly ongoing during the first hour subsequent to the irradiation. After five irradiation cycles the bow change adds up to 0.5nm, 2nm and 4nm respectively.

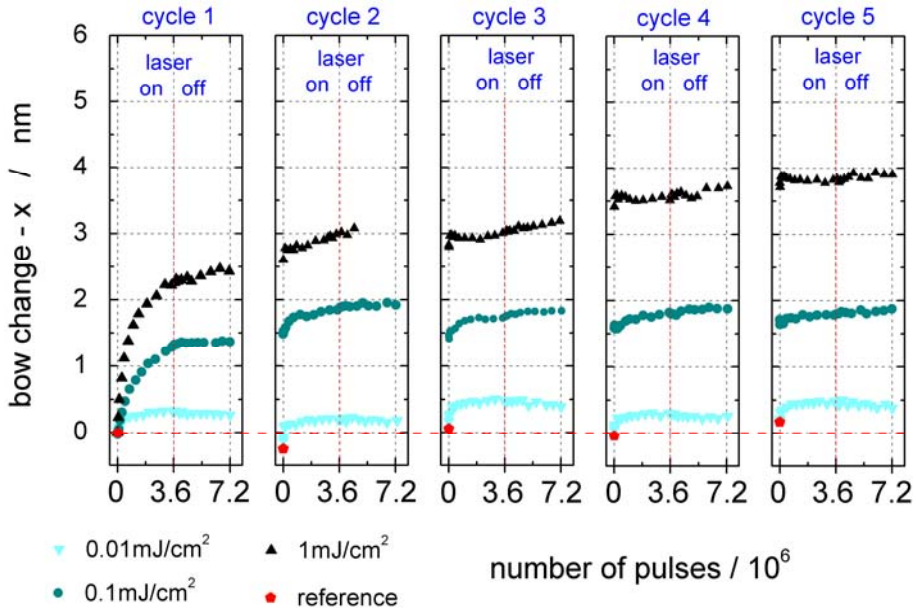

Fig. 47: Laser induced bow change in x-direction at “low” energy levels

The results for the mirror’s y-direction are presented in fig. 48. The trend of the occurred bow change is similar to the results shown above but less significant. For the 0.1mJ/cm^2 and 1mJ/cm^2 - series it adds up to 1nm and 2nm respectively, which is about the half compared to the x-direction. In both diagrams it is noticed that single irradiation cycles for a certain energy level show fluctuations of some 0.1nm within the whole series. But these fluctuations are very

small and are either covered by the normal measurement noise or maybe caused by small uncertainties of the measurement conditions.

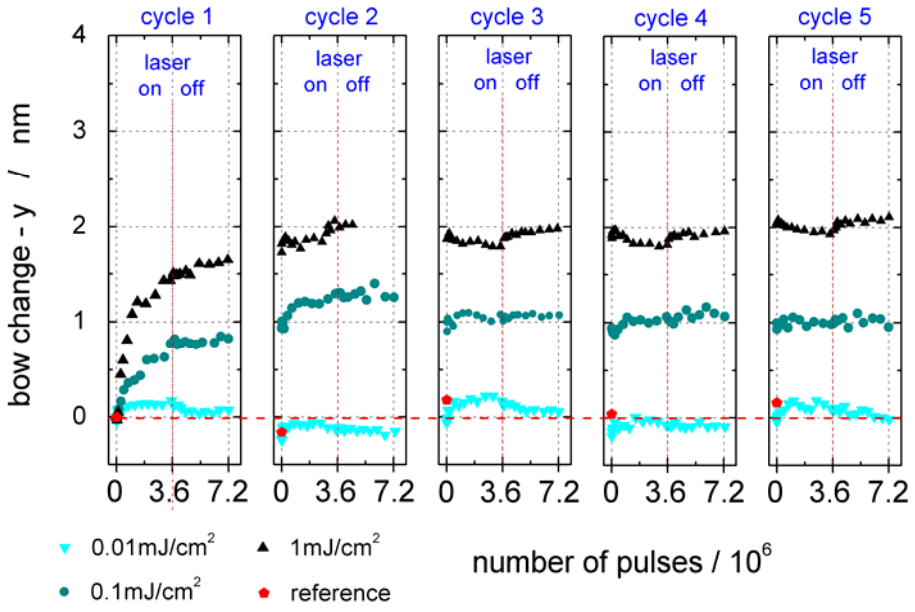

Fig. 48: Laser induced bow change in y-direction at "low" energy levels

Table 6 shows a summary of the laser induced bow change at energy levels from 10µJ/cm² – 1mJ/cm².

"low" energy density: 10µJ/cm² – 1mJ/cm²:		
state of the laser	**type of bow change**	**direction of bow change**
during and past the exposure	bow change is mainly permanent, no relaxation	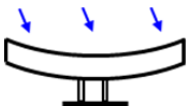 positive direction

Table 6: Overview about laser induced bow change at „low" energy densities

Bow change as a function of the deposited energy

The bow change as a function of the deposited energy is depicted in fig. 49 below. The depicted curves are similar to these from fig. 45 – 48 shown above and show the development for energy densities of 1mJ/cm^2 – 30mJ/cm^2. Depending on the energy level of the particular curve, data from different irradiation cycle (1 – 5) are depicted. The curve of the 1mJ/cm^2 level includes the first three irradiation cycles. For the energy levels > 1mJ/cm^2 the depicted curves just include parts of the first irradiation cycle. In fig. 49a (bow change along the x-axis) we see the that all curves show a similar development including a quick positive rise of the bow within a dose of 5*10^{3}J/cm^2. The further increase of the dose up to 10^{4}J/cm^2 has almost no effect on the bow. The 1m/cm^2–curve exhibits sudden changes at 4*10^{3}J/cm^2 and 8*10^{3}J/cm^2, coming from the interruptions in the irradiation between the different cycles. Remember the fact, that there was an interruption of one day between each irradiation cycle.

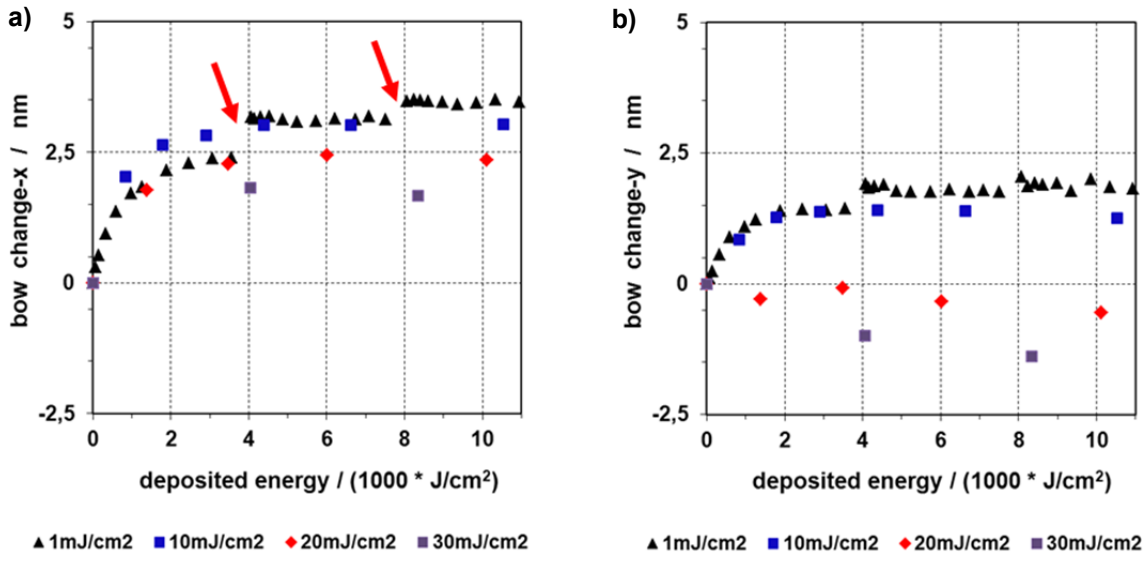

Fig. 49: Bow change during the first irradiation cycle(s) as a function of the deposited energy: a) bow change – x, b) bow change - y

Fig. 49b shows the development along the mirror's y-axis. Here the curves for 20mJ/cm^2 and 30mJ/cm^2 show a negative bow change right from the beginning. It is assumed that the different development arises from the mirror's 2-post design (see the discussion in p. 106f.).

Conclusion:

The irradiation of the samples at low energy levels resulted in a positive bow change, which happens quicker the higher the energy level is. Additionally it was observed that this effect is

even slightly ongoing during the first hours subsequent to the irradiation, which resulted in sudden steps of the bow between different irradiation cycles. Finally it became apparent, that the positive bow change during the first irradiation cycle is similar for low and high energy levels up to a deposited dose of 10^4J/cm^2. From this it is assumed that the observed positive bow change is a unique conditioning process of the sample like a permanent change of the material properties. The final discussion is made on p. 113.

3.3.1.3 Bow change at "high" energy densities

The following section describes the bow change for "high" energy densities from 10mJ/cm^2 - 30mJ/cm^2. We will see that the development of the mirror bow during an irradiation can differ significantly from the development after the irradiation. The results for the bow change in the x-direction are presented in fig. 50. Consider the scale of the diagram's y-axis which is now enlarged to a width of 25nm. Compared to the low energy range there is now an opposite behaviour. During the laser exposure the mirror bow changes in negative direction. After the irradiation the bow relaxes partially towards the initial value.

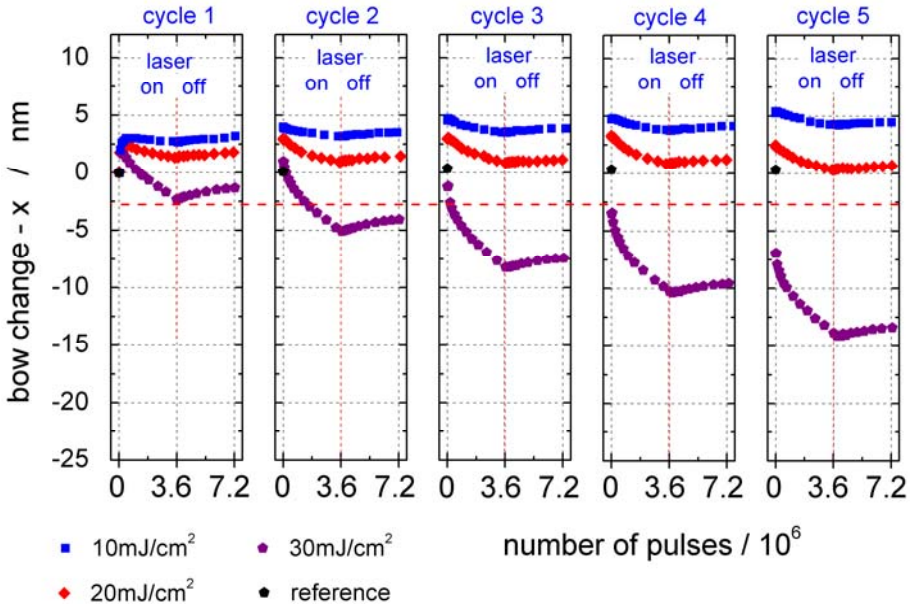

Fig. 50: Laser induced bow change – x at "high" energy levels

At 10mJ/cm^2 the negative change within a single cycle is about -1.5nm followed by a relaxation of +0.5nm within the first hour. The tendency in the longer run of five cycles is clearly positive. For the 20mJ/cm^2 – series the irradiation response is increased to -3nm and the tendency in the longer run changes from positive to slightly negative. For the 30mJ/cm^2 level the negative bow change adds up to more than -7nm within a single cycle. The negative tendency within the whole series becomes quite significant and adds up to -13nm after five cycles.

The results for the mirror's y-direction (along the tilting axis) are shown in fig. 51. The negative bow development during an exposure is now even heavier. For 10mJ/cm^2 it comes to -2nm. The subsequent relaxation seems to compensate the laser induced bow change more or less exactly. Each of the cycles "3", "4" and"5" start around the same height level as the day before. For the 30mJ/cm^2 series the bow change comes more than -10nm during a single cycle and adds up to -18nm after the whole series.

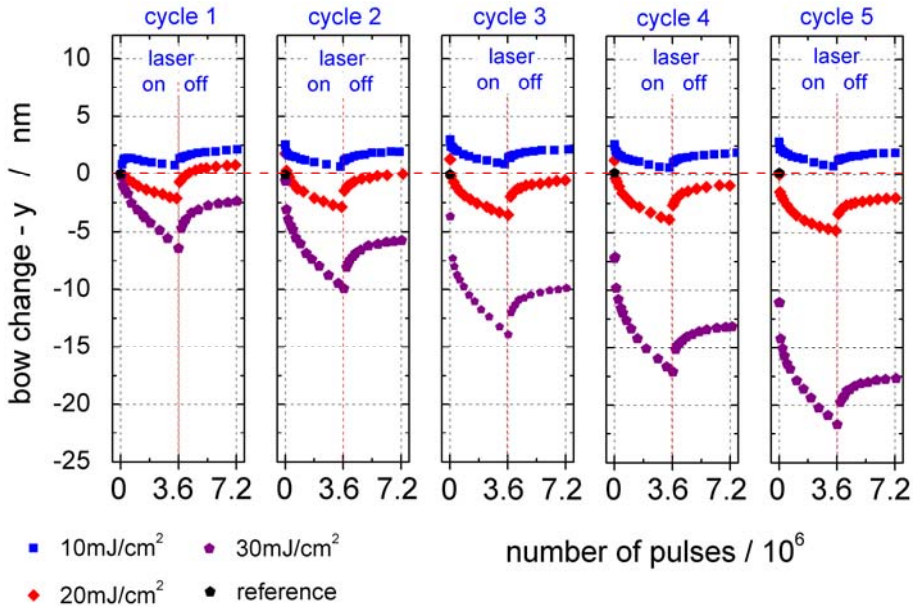

Fig. 51: Laser induced bow change – y at "high" energy levels

Table 7 shows a summary of the laser induced bow change at energy levels from 10mJ/cm^2 – 30mJ/cm^2.

Conclusion

Mirrors irradiated at high energy densities behave differently compared to low energy densities. During the irradiation they show a negative bow change, which goes along with the ap-

plied energy level. After the irradiation they partially relax towards their initial value. It is assumed that the negative bow change arises from the laser induced heating. The irradiation in the mJ/cm^2-regime results in an increasingly heating of mirror and the underlying actuator. The laser induced heating is discussed in detail in chapter 3.4 (p.75). It is conceivable that the heating of mirror and actuator causes a bimorph effect, which results in the observed bowing. Furthermore it was observed that the negative bow change is bigger along the mirror's tilting axis (y-axis).

"high" energy densities: 10mJ/cm^2 – 30mJ/cm^2:		
state of the laser	**type of bow change**	**direction of bow change**
during the irradiation	negative bow change	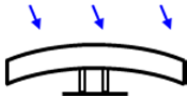 negative direction
after the irradiation	partially relaxation	 positive direction

Table 7: Overview about laser induced bow change at "high" energy densities

3.3.2 Dependence of the bow change on the laser repetition rate

The following section describes the effect of the laser repetition rate on the detected mirror bow change. The applied irradiation parameters are presented in table 8. Samples were irradiated at a constant energy density of 10mJ/cm^2 and varying repetition rate of 250Hz, 500Hz, 1kHz and 2kHz. The upper value was limited by the maximum repetition rate of the used laser. The experimental procedure was the same as before. For a certain repetition rate a series of five irradiation cycles was carried out. A single irradiation cycle includes first the irradiation of the sample with 3.6*10^6 pulses followed by a continued bow detection of one hour with the laser being off. For all repetition rates the amount of deposited energy was the same.

energy density	**laser repetition rate**	**number of pulses**	**ambient atmosphere**
10mJ/cm^2	**250Hz – 2kHz**	**5 * 3,6 10^6**	**N_2 ($O_2 \leq 1\%$)**

Table 8: Overview about the applied irradiation parameters

Figure 52 shows the bow change in x-direction for samples irradiated at 250Hz, 500Hz, 1kHz and 2kHz. Within the investigated domain there seems not to be a significant dependence of the bow change on the applied repetition rate.

During the first cycle the bow first changes in positive direction and then, while the irradiation is ongoing, turns around and changes in the negative direction. When the laser is switched off a slight relaxation in positive direction is observed. During the following cycles (2-5) all curves show a similar behaviour. During the irradiation the bow develops in negative direction. This development equals about 1nm in cycle 2 and rises within the following cycles to about 2nm in cycle 5. After the laser is stopped one observes a slight relaxation in the opposite direction. All in all this behaviour is known and comparable to this from the previous investigation of the applied energy density.

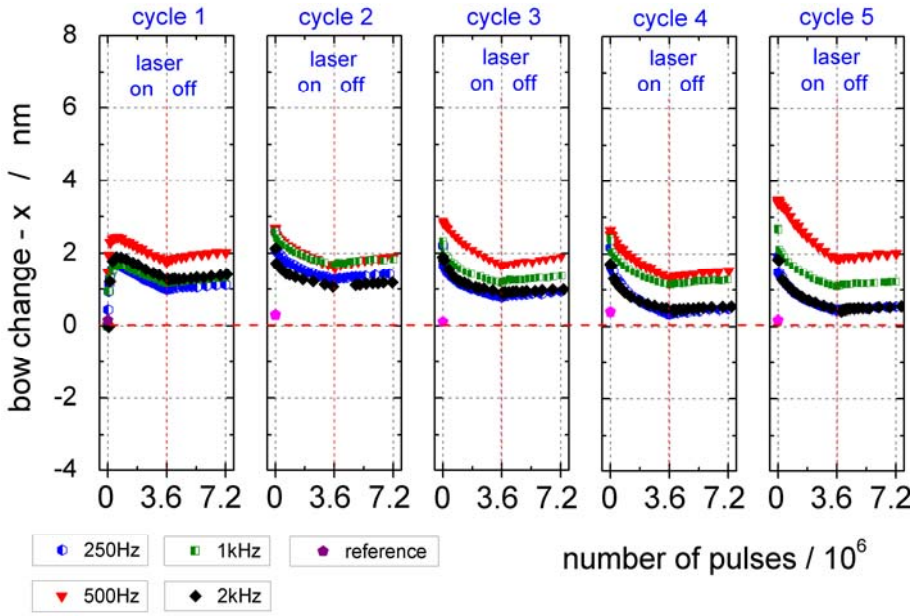

Fig. 52: Dependency of the bow change -x from different repetition rates (250Hz, 500Hz, 1 kHz, 2 kHz) within a series of five irradiation cycles with 3.6*10^6 pulses each

The bow change in y-direction is presented in fig. 53 below. Unlike to the x-direction there is a clear effect of the repetition rate visible. A dependence on the repetition rate is observed during the first and during later irradiation cycles (cycle 2 - 5).

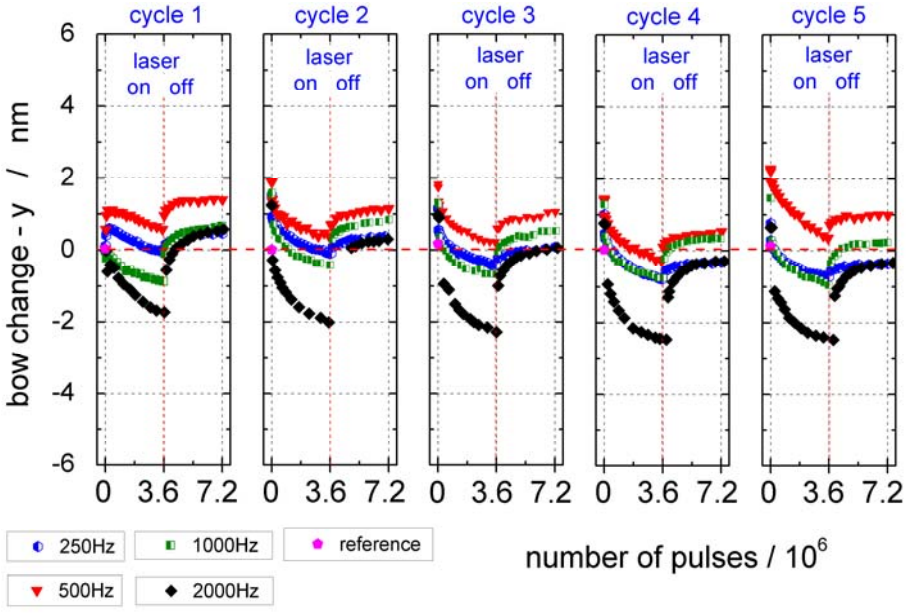

Fig. 53: Dependency of the bow change -y from different repetition rates (250Hz, 500Hz, 1kHz, 2kHz) within a series of five irradiation cycles with 5*3.6 10^6 pulses

During the first cycle the bow initially changes positively at 250Hz and 500Hz and then changes in opposite direction. Whereas at 1kHz and 2kHz the bow changes in negative direction right from the beginning. Such a phenomenon was already presented in the last chapter, where it was observed at different energy densities (see p. 63). It is assumed that the change of the mirror bow in either positive or negative direction is caused by two different effects. The negative development seems to be effected by the mirror temperature which is higher at higher repetition rates (see chapter 3.4.3, p. 80).

Within the following irradiation cycles (2 – 5) the mirrors show a clear dependence of the negative bow change on the repetition rate. However this dependence is not recognized at first glance. For this reason the bow change in y-direction is again depicted, now slightly different in another figure (fig. 54) below. For better comparability of the specific repetition rates now the initial value of each irradiation cycle is set to zero and the different repetition rates within each cycle can be compared easily. It is clearly noticed that higher repetition rates result in a higher negative bow change.

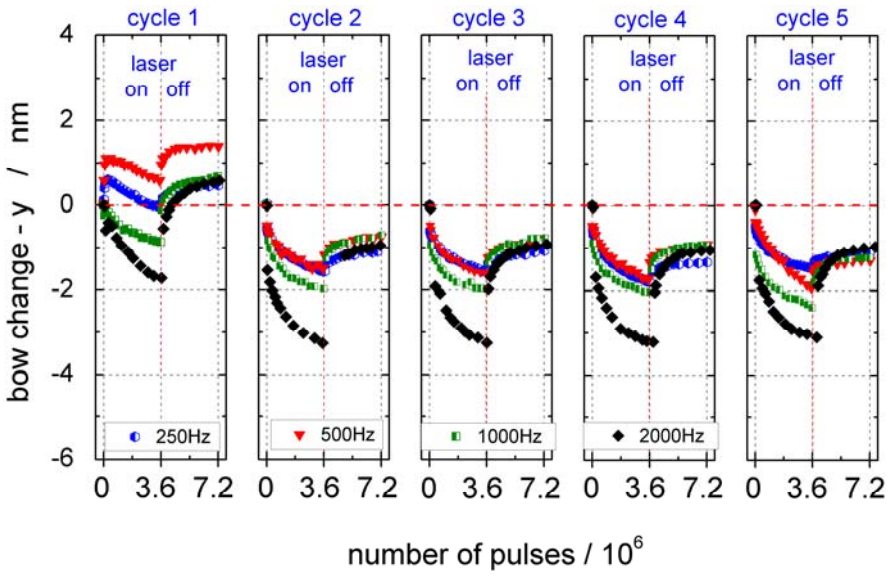

Fig. 54: Dependency of the bow change -y from different repetition rates. For a better comparability of the specific repetition rates, the initial value of each irradiation cycle is set to zero.

At 250Hz and 500Hz the negative bow change is (-)1.5nm. At 1kHz it is (-)2nm and at 2kHz it is (-3)nm. When the irradiation is stopped the mirrors bend in opposite direction towards their initial shape. This process seems to be independent from the applied repetition rate. Independent from the repetition rate the mirrors end up at the same bow data.

Conclusion

It became apparent, that within the investigated domain (250Hz – 2kHz) there is a clear dependence of the bow change on the laser repetition rate. The higher the repetition rate the higher the negative bow change during the irradiation. The bow change of (-)1.5nm at 250Hz was almost doubled at 2kHz. It is assumed that this tendency arises from an increasing mirror temperature. This statement is supported by investigations regarding the laser induced heating of the mirrors. It turned out that the average mirror temperature rises about 15K at 250Hz und almost 30K at 2kHz (see p. 80). Additionally the measurements showed that the laser induced temperature rise is about the same at 250Hz and at 500Hz. This, in turn matches the fact that the negative bow change at 250Hz and 500Hz is about the same as well. However the dependency on the repetition rate was just observed along the mirror's y-axis. It is assumed that the mirror's 2-post design generally causes a bigger bowing along the y-axis when the energy density is in the mJ/cm^2 domain. This phenomenon was already observed during the investigations regarding the applied energy density (see p 63f.).

3.3.3 Dependence of the bow change on the ambient atmosphere

The following section describes the effect of different ambient atmospheres (N_2 and air) on the detected bow change. The irradiation in the N_2 environment corresponds to the standard atmosphere like in all former experiments. Here a constant N_2 flow of 1 litre per minute was piped into the irradiation chamber. The N_2 atmosphere included a residual percentage of O_2 less or equal than 1%. During the irradiation in air there was no gas flow at all. The applied irradiation parameters are presented in table 9. For the present experiment different positions on one sample were irradiated either in air and N_2 and then compared to each other. Hence the sample conditions were completely the same.

energy density	laser repetition rate	number of pulses	ambient atmosphere
10mJ/cm^2	**1000Hz**	**5 * 3,6 10^6**	**air/ N_2 ($O_2 \leq 1\%$)**

Table 9: Overview about the applied irradiation parameters

The experiment is carried out by applying the standard procedure. A sample is irradiated during a series of five irradiation cycles at a specific set of irradiation parameters. Figure 55 below shows the bow change in x-direction for a sample irradiated in air and nitrogen. The characteristic positive bow change at the beginning of the first cycle is somewhat higher for the nitrogen atmosphere. The adjacent turnaround, the development in negative direction and the relaxation occurs similar for both cases. Within the following cycles (2 – 5) there is the typical negative bow development during the irradiation followed by a partial relaxation in positive direction afterwards. After the entire series of 18*10^6 pulses there is no tendency visible whereto the bow might develop in case of a further exposure.

The bow change in y-direction is presented in fig. 56. Again there is a difference in the bow development during the first cycle. There is a negative bow change right from the beginning of about 2nm in air and about 1nm in N_2.

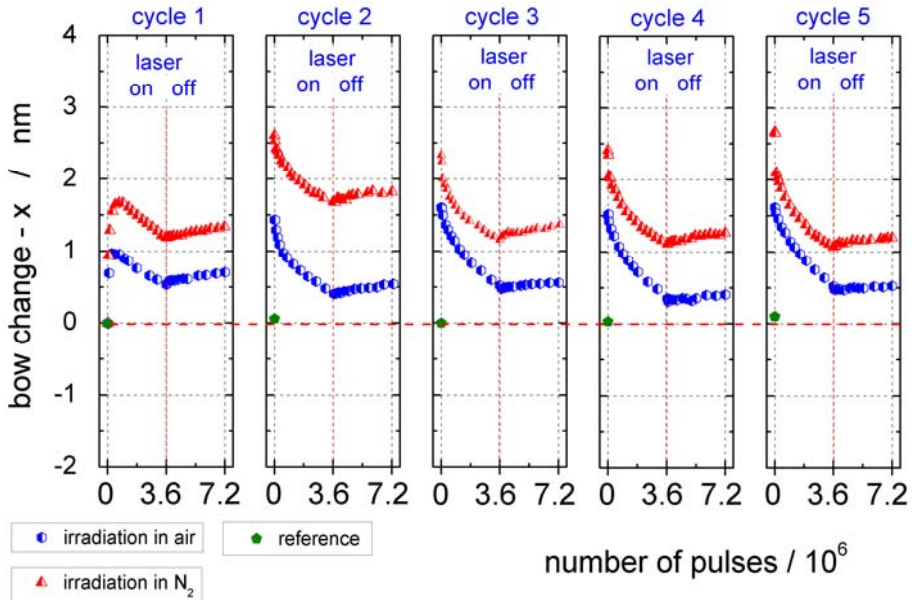

Fig. 55: Dependency of the bow change -x from the ambient atmosphere (air and N_2) within a series of five irradiation cycles with $3.6*10^6$ pulses each

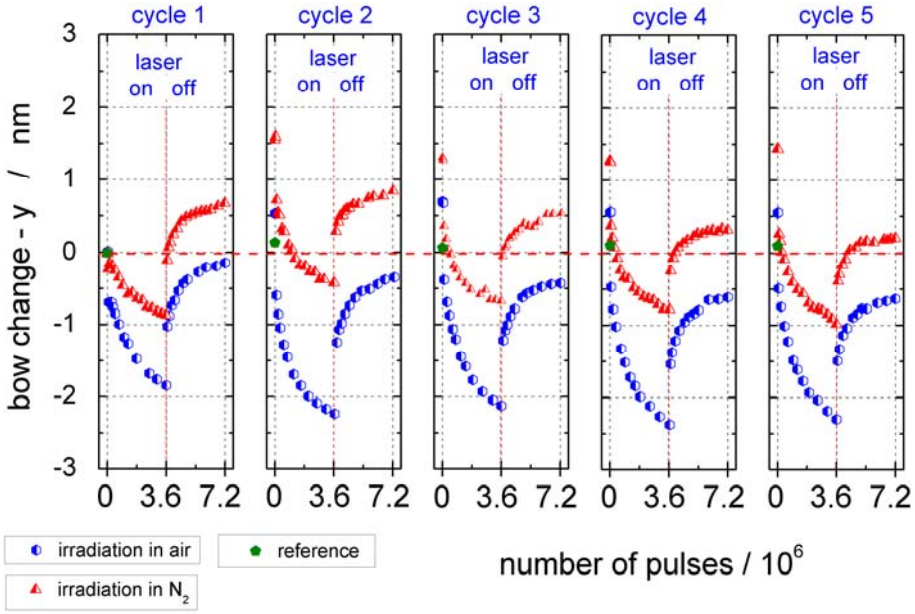

Fig. 56: Dependency of the bow change -y from the ambient atmosphere (air and N_2) within a series of five irradiation cycles with $3.6*10^6$ pulses each

For a better comparability of each particular irradiation cycle, the curves are again depicted in fig. 57, now with the initial value of each irradiation cycle set to zero. It is found that the neg-

ative bow change during all of the following cycles (2 – 5) is somewhat bigger in air (-3nm) than in N_2 (≈ -2nm). The reason might be a better heat transport by the gas flow in case of the N_2 atmosphere. The relaxation subsequent to the exposure occurs similar in both cases.

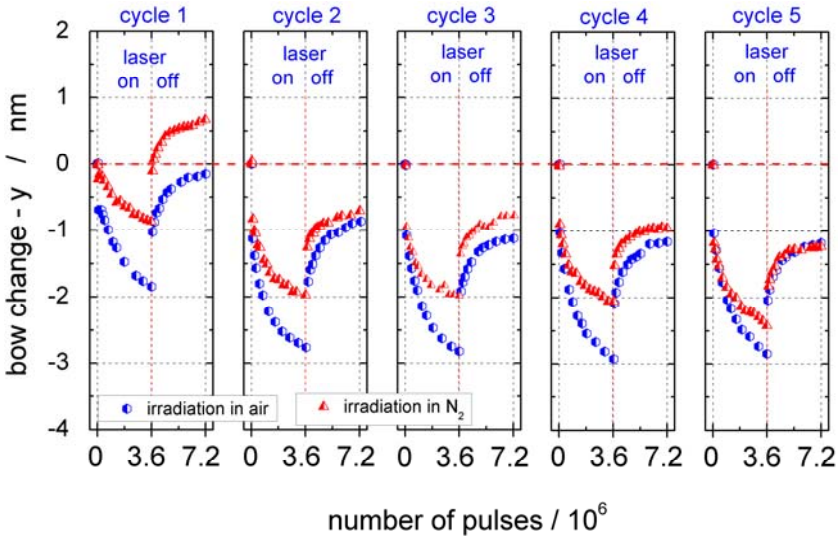

Fig. 57: Dependency of the bow change -y from the ambient atmosphere air and N_2); for better comparability the initial value of each irradiation cycle is set to zero

Conclusion

The irradiation in air and N_2 atmosphere did not result in a significant difference in the detected bow change. The bow change-x is more or less identical for both cases. The bow change-y is slightly bigger in air. The difference is in principle rather small, but the phenomenon was reproduced on different samples. The remaining portion of O_2 (≤ 1%) in the N_2 atmosphere is in all likelihood orders of magnitudes too high to see significant results coming from the absence of O_2.

3.3.4 Dependence of the bow change on the applied pulse number

The following chapter describes the effect of a rising pulse number on the detected bow change. For this purpose, samples were exposed to $250*10^6$ pulses (at $10mJ/cm^2$) compared to $18*10^6$ during previous experiments. The applied irradiation parameters are presented in table 10.

energy density	laser repetition rate	number of pulses	ambient atmosphere
$10mJ/cm^2$	**1000Hz**	**$250 * 10^6$**	**N_2**

Table 10: Overview about the applied irradiation parameters

Contrary to the previous experimental procedure, samples are now exposed continuously except for short interruptions for laser gas exchange once in a while. The detected bow change in x- and y-direction is presented in fig. 58. The curves show several longer interruptions. These interruptions occur at night where the measurement of the bow was not carried out, but the exposure itself was ongoing.

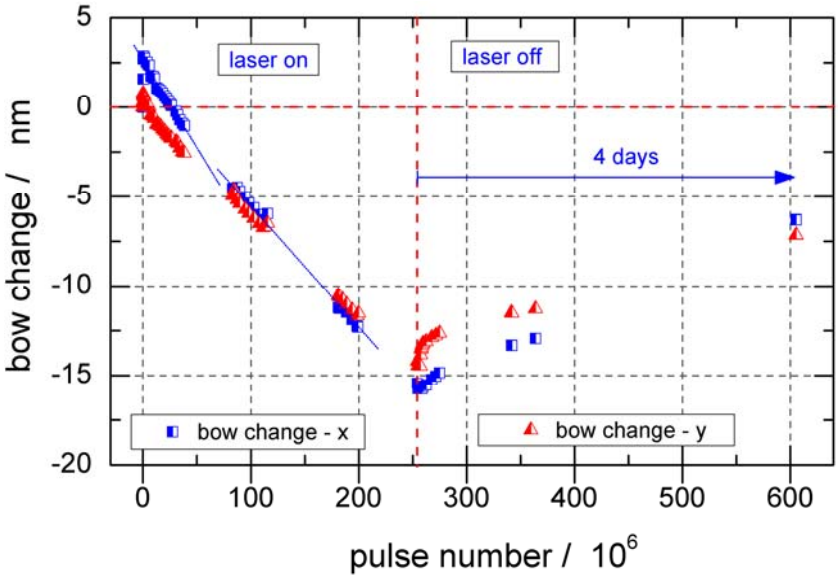

Fig. 58: Development of the bow change during a long-term exposure of $250*10^6$ pulses

During the first pulses there is the characteristic bow change in positive direction with 3nm in x and 1nm in y. Then, the bow development turns around and now steadily changes in negative direction until the exposure is stopped. A rising pulse number goes along with a slight flattening of the slope, as indicated by the blue lines. But an end of the development is not in sight. Within the $250*10^6$ pulses, which corresponds to a duration of three days, the change sums up to (-)15nm. When the exposure is stopped one observes the characteristic relaxation in positive direction. At the beginning the rate is somewhat higher in the mirror's y-direction which is probably caused by the "2 posts–effect". After a few hours the rate equals and is ongoing for several days. After four days the past exposure measurement was stopped. At this time, the initial bow change was relaxed by about 50%.

Conclusion

The long-term exposure brings to light different new aspects and extends the understanding of the mirror performance under laser light. There is e.g. the primary positive development of the bow, which has actually no relevance in the long run. Besides, a temperature increase or decrease as the physical mechanism behind the bow change can just be a driving force within a few minutes after the laser is turned on or off (see p.77). After some minutes, when mirrors and underlying layers should have reached equilibrium, other mechanisms like creep of the mirror plate must be considered as the physical mechanism.

3.4 Measurement of the mirror temperature during a laser exposure

3.4.1 Experimental setup

The following chapter describes the measurement of the laser induced temperature rise of the aluminium based micro mirrors. The experiment is based on the detection of the temperature dependent ohmic resistance of an electric conductor. For this purpose, several mirrors are connected to an ohmic resistor (fig. 59a) and a four-terminal sensing is applied to detect the change of the temperature dependent resistance of the irradiated mirrors (fig. 59b). The sample preparation is presented in detail in [58].

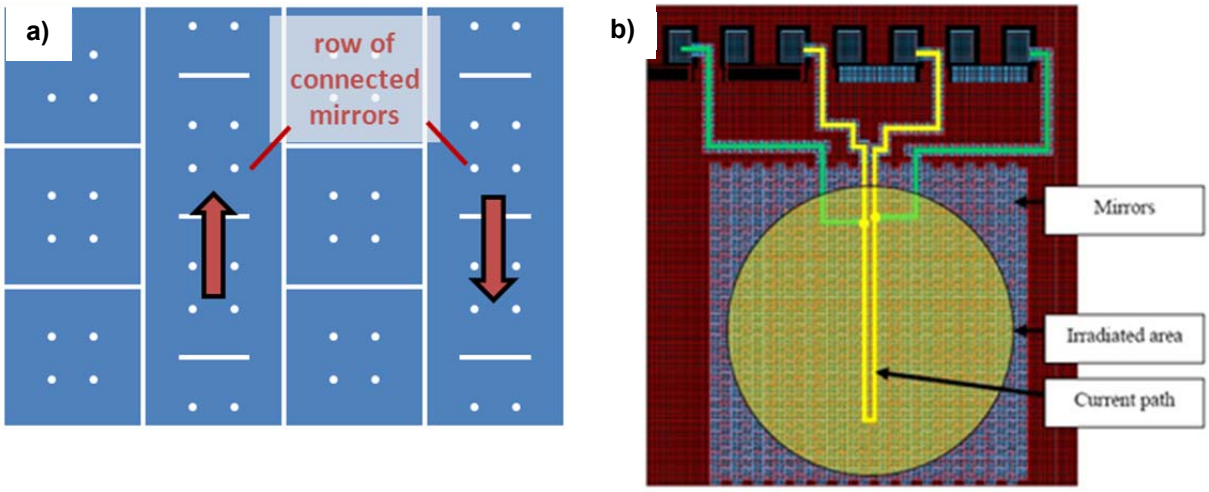

Fig. 59: Experimental setup for the temperature measurement with a) mirrors connected to an ohmic resistor and b) layout of the four-terminal sensing [58]

In advance to the real temperature measurement the electric conductor (electrically connected mirrors) has to be calibrated in order to determine the resistance – temperature curve. This is done by heating up the sample in an oven and determining the ohmic resistance at certain temperature levels. The mirrors, used for the temperature measurements, have a slightly different design compared to the standard mirrors used in the thesis. They consist of a four-layer stack of Al_2O_3/ Al/ Al_2O_3 /Al with a total stack height of 350nm. Figure 60 shows the resistance–temperature curve. At room temperature the connected mirrors show a resistance of about 85Ω that increases almost linearly to 102Ω at 90°C. As the result of the resistance-temperature calibration one obtains the linear fit function, see table 11.

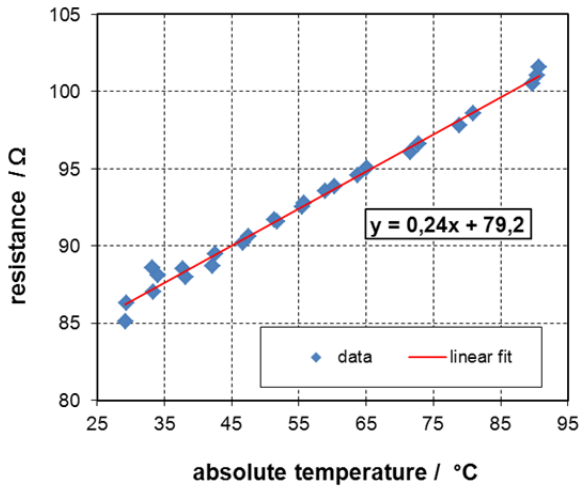

Fig. 60: Calibration curve of the temperature dependent resistance

linear fit function
R(T) = 0.24*T + 79.2Ω

Table 11: Linear fit function as the result of the resistance–temperature calibration

The four-terminal sensing is carried out by applying a constant current along the yellow path and detecting the voltage between the green contacts, see fig. 59b. The voltage detection is done with a storage oscilloscope that enables the detection of quick events e.g. the temperature rise induced by a single nanosecond laser pulse. The mirror temperature is then determined with the fit function of the resistance–temperature curve which is converted into equ. 18.

$$\boldsymbol{T = \frac{(U_T - U_0)}{I * m}} \qquad \textbf{(18)}$$

T=temperature, U_0=detected voltage at room temperature, U_T=temperature dependent voltage, I=constant current, m=slope of the fit function

An important detail regarding the entire experiment is that the sample was not cooled. It means that there was no defined heat sink.

3.4.2 Average mirror temperature at varying energy levels

Within the present chapter the temperature change induced by a pulse train (steady exposure) with different energy densities is determined. The term “average temperature” means that a single data point of the below presented curves is generated by averaging the mirror tempera-

ture within a cycle of several thousand laser pulses. Hence, this measurement does not show the temperature change in the course of a specific pulse. The single pulse response of the mirror temperature is presented later on in chapter 3.4.4 (p.82). During the experiment the sample was irradiated for one hour at a certain energy level. Between two different levels the irradiation was stopped for 30minutes. The irradiation parameters are summarized in table 12.

energy density	laser repetition rate	number of pulses	ambient atmosphere
5mJ/cm^2 – 30mJ/cm^2	1000Hz	3.6 *10^6	N_2 ($O_2 \leq 1\%$)

Table 12: Overview of the applied irradiation parameters

The average mirror temperature for energy densities of 5mJ/cm^2 10mJ/cm^2, 20mJ/cm^2 and 30mJ/cm^2 is shown in fig. 61a and b. For all applied energy levels there is a volatile increase of the temperature within the first seconds which then slows down. Depending on the applied level the increase sums up to about 5K, 12K, 26K and 38K respectively within a half hour of irradiation (fig. 61a). As expected, the temperature decreases rapidly after the laser is switched off. The temperature rise as a function of the applied energy density is presented in fig. 61b. Here the final temperature after an irradiation of one hour is depicted.

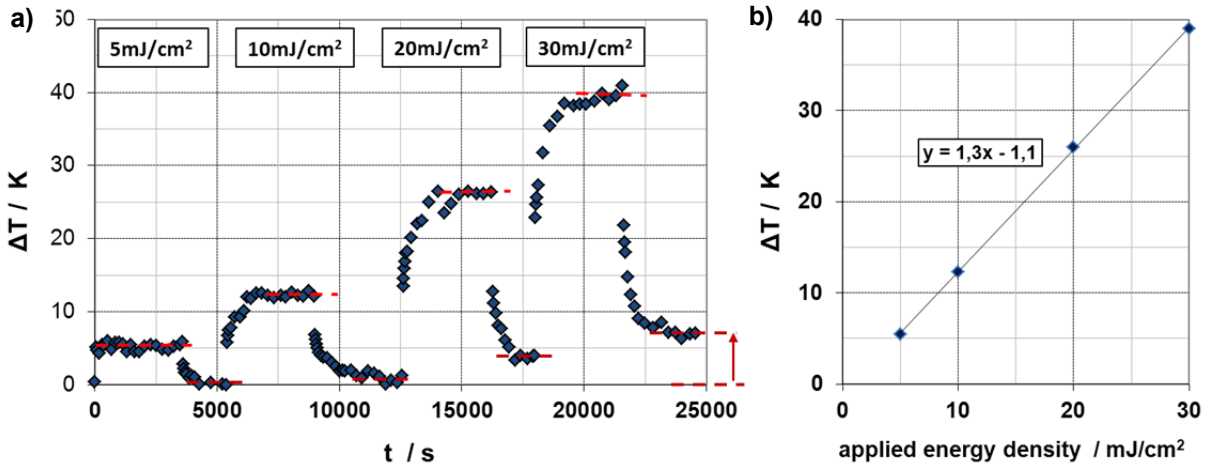

Fig. 61: Laser induced temperature rise during a "pulse train" as a function of time at different energy levels b) … as a function of the applied energy density

However, the experiment poses two questions. The first question is: Why does the "off level" not completely returns to its initial value. After the whole series, the off level ends up at +7K (see the red arrow in fig. 61). Of course this does not correspond to the real mirror temperature but is probably caused by a permanent modification of the ohmic resistance of the irradiated circuitry. This phenomenon is represented in detail in fig. 62. The above used device has run through several cycles of irradiation and calibration. The "room temperature level" of the ohmic resistance, detected previously to an irradiation or calibration, rises from 40Ω to almost 100 Ω within a few days. A possible explanation for this modification might be a laser induced oxidation of the conducting layer of the irradiated mirrors. To avoid the problem within the experiment, the calibration of the resistance-temperature curve was repeated for each irradiation cycle.

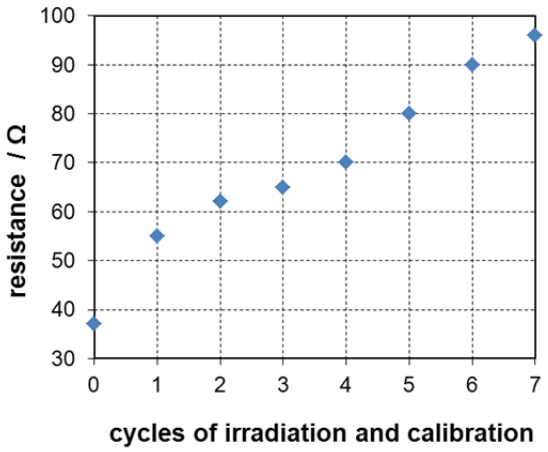

Fig. 62: "Room temperature level" of the ohmic resistance, detected previously to each irradiation and calibration cycle

The second question is: Why does it last more than 15min. to heat up the mirrors to thermal equilibrium? Considering the low thermal mass of a single mirror and its almost free standing position in space one would expect it to reach equilibrium much earlier. The hypothesis is that the mirror temperature cannot be discussed isolated from the temperature development of the substrate underneath.

For a comparison of both the temperature change in the CMOS plane is determined with an integrated detector based on the temperature dependent potential drop of a p-n junction. However, both temperature sensors are realized in different device types. Consequently the comparative measurements were not done in parallel, but one after another. For the experiment the samples are continuously irradiated for one hour at 10mJ/cm^2 and 1kHz, see fig. 63. The general outcome is as follows: The substrate temperature increases rather uniform about 5K with-

in 15min. and remains several degrees below the mirror level. The rise of the mirror temperature is volatile within the first seconds, then slows down and goes similar to the substrate.

The substrate has a “huge” thermal mass compared to the mirrors. Additionally there is a restricted heat flow between mirrors and substrate (see fig. 21, p. 27). Both factors might damp the rise of the substrate temperature and explain the different temperature levels. The term substrate is unfortunately not well defined in this context. The substrate probably includes more material than just the CMOS plane. Since there was no defined heat sink coupled to the SLM, the whole SLM housing was heated up and increased the thermal mass of the “substrate” to an unknown level.

It seems likely that the development and the final level of the temperature in the mirror plane, after the volatile increase at the beginning, is determined by the substrate temperature. Thus, the increase of the mirror temperature from 7K to 12K would arise from the increasing “offset” of the substrate temperature underneath.

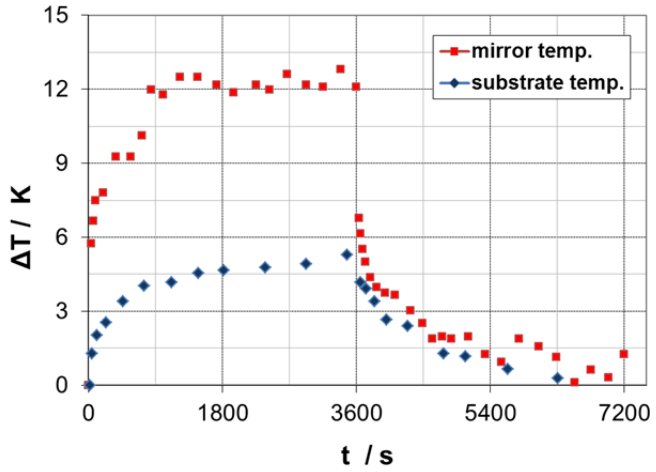

Fig. 63: a) Laser induced temperature rise of substrate and mirror plane at 10mJ/cm^2 and 1kHz

Conclusion

As expected there is a strong dependence of the average mirror temperature on the applied energy density. The irradiation at 5mJ/cm^2 resulted in a rise of 5K, at 30mJ/cm^2 of 39K. Depending on the applied energy level it surprisingly lasts up to several minutes until the mirrors seem to have reached thermal equilibrium. It is assumed that the heating of the underlying substrate occurs much slower. After its volatile rise at the beginning, the further increase of the mirror temperature goes along with the slower heating of the substrate underneath.

3.4.3 Average mirror temperature at varying repetition rates

The following section describes the laser induced temperature change during at different laser repetition rates. The sample is irradiated continuously for half an hour at a particular repetition rate. Then the laser is stopped. After a break of 15 minutes the irradiation is continued with the next repetition rate. The experimental conditions are summarized in table 13.

energy density	laser repetition rate	number of pulses	ambient atmosphere
10mJ/cm^2	**250Hz – 2kHz**	**1.8 *10^6**	**N_2 ($O_2 \leq 1\%$)**

Table 13: Overview of the applied irradiation parameters

The average mirror temperature as a function of time and the applied laser repetition rate (250Hz, 500Hz, 1kHz and 2kHz) is presented in fig. 64a. An irradiation at 250Hz and 500Hz results in a rise of 15K and 16K respectively. At 1kHz and 2kHz the temperature rises about 21K and 28K respectively. After the final run the temperature remains 5K above the initial value. This phenomenon was already observed in the last chapter, where the temperature rise at different energy densities was determined (see p.77). The temperature rise as a function of the applied repetition rate after a continuous irradiation of 30 minutes is presented in fig. 64b.

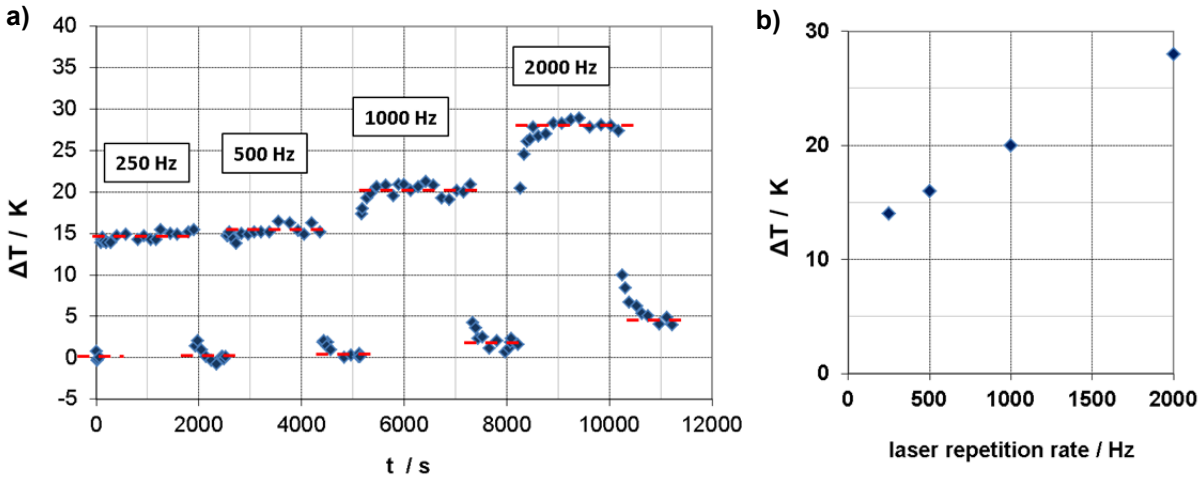

Fig. 64: a) Laser induced temperature rise as a function of time at different laser repetition rates (250Hz, 500Hz, 1kHz, 2kHz), b) … as a function of the applied repetition rate

Conclusion

Within the investigated domain the average mirror temperature shows a clear effect on the applied laser repetition rate. However, the difference between 250Hz and 500Hz is rather small and just amounts to 1K-2K. But this statement is supported by former investigations where the bow change was detected as a function of the applied laser repetition rate. In this case, the bow change at 250Hz and 500Hz was also similar (see p. 66f.).

3.4.4 Temperature change induced by a single laser pulse

The following section presents the change of the mirror temperature in the course of a single laser pulse of varying energy levels. The irradiation parameters are summarized in table 14. For the experiment, the samples were irradiated with pulses with a pulse length τ_p=16ns (FWHM) and energy levels of 0.1mJ/cm^2, 1mJ/cm^2, 10mJ/cm^2, 20mJ/cm^2 and 30mJ/cm^2. The temperature rise induced by single laser pulses of varying energy levels as a function of time is presented in fig. 65a. Note that the depicted curves represent an average of 64 events to reduce the measurement noise. The arrival of the pulse on the sample is not exactly known. Test have shown, that the pulse was arriving a few microseconds before the trigger-out signal of the laser.

energy density	laser repetition rate	number of pulses	ambient atmosphere
0.1mJ/cm^2 – 30mJ/cm^2	**single pulse**	**single pulse**	**N_2 ($O_2 \leq 1\%$)**

Table 14: Overview about the applied irradiation parameters

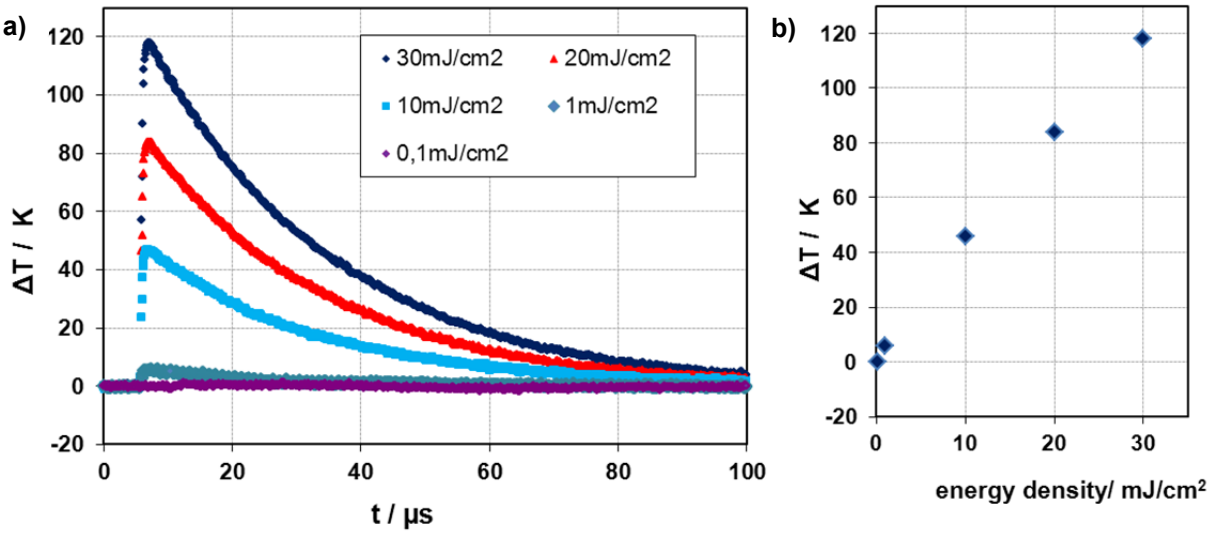

Fig. 65: a) Temperature rise induced by single laser pulses of varying energy densities as a function of time, b) temperature rise as a function of the applied energy density

At the lowest energy level of 0.1mJ/cm^2 the mirror temperature shows actually no response to the incoming pulse. For rising pulse energies a sudden increase of the mirror temperature within microseconds is observed. A 10mJ/cm^2 pulse causes a rise of 46K. The maximum energy level of 30mJ/cm^2 causes a rise of 117K. In fig. 65b the temperature rise as a function of the applied pulse energy is depicted.

To get a detailed impression of the time response, the rise and falling time in the course of a single 10mJ/cm^2 pulse is presented in fig 66. The rise time from the 10% to the 90% level is shown in fig. 66a and equals t_r = 0.6 µs. The falling time from ΔT_{max} to the ΔT_{max} * e^{-1} level equals τ = 27µs (fig. 66b).

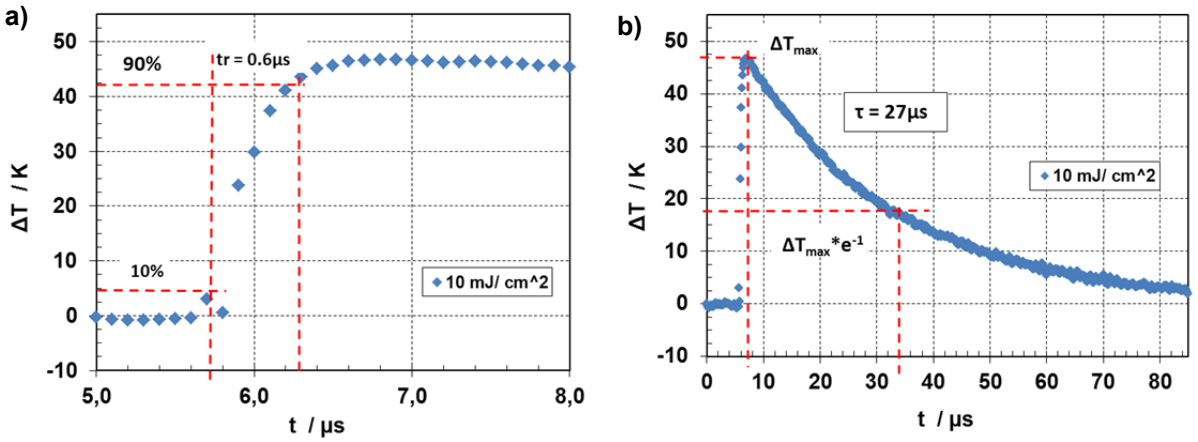

Fig. 66: a) Temperature rise time from the 10% to the 90% level induced by a single pulse at 10mJ/cm^2, b) falling time from ΔT_{max} to the ΔT_{max} * e^{-1} level

Comparison with calculated quantities

In chapter 1.5 (p.26 ff.) rise and falling of the mirror temperature following a single laser pulse were determined. A pulse of 10mJ/cm^2 was estimated to cause a rise of the mirror temperature of 26K, which is 20K below the measured rise of 47K. However for simplification reasons the model just assumed a single-layer aluminium mirror. But the mirror used in the temperature measurements consists of a 4-layer stack of Al_2O_3 and Al. Heating and heat transfer in the real mirror should be slightly different. Additionally there are further error sources. Inhomogeneity of the laser beam profile and an uncertainty regarding the mirror's absorptivity result in an uncertainty of the applied energy density of at least 30%. In this context, the agreement of experiment and calculation seems to be acceptable.

The falling time from ΔT_{max} to the $\Delta T_{max} * e^{-1}$ level was estimated to be 19µs and shows a good agreement to the measurement of 27µs.

Possible error sources

The pulsed resolved measurements have shown that the rise of temperature and ohmic resistance in the sample happens within 1µs. But the settling time of the used current source is defined as ≤ 500µs. From this it has to be assumed that the current source is not able to control the current appropriately. In this context appropriately would mean to compensate the changing resistance of the irradiated mirrors within 0.1µs or quicker. The question is whether a variation in the "constant current" was exceeding a level where it had a significant effect on the detected temperature-driven voltage signal. In case, it would have resulted in a detected temperature rise smaller than the real temperature rise. In this case the real peak values of the 10mJ/cm^2, 20mJ/cm^2 and 30mJ/cm^2 curves would probably not have been detected at all and the trailing edges of the curves should be very close to each other. But fig 65a, b show an almost linear dependence of the detected peak values on the applied pulse energy. And the result of the calculated peak value was (with a certain uncertainty) in the same order of magnitude than the detected one. For this reason it is assumed that the detected peak values exhibit the correct order of magnitude.

Conclusion

The pulse-resolved measurements have shown that the mirror temperature rises within some hundred nanoseconds and amounts to values many times higher than the average temperature rise. The maximum applied pulse energy of 30mJ/cm^2 resulted in a peak of 120K compared to the average rise of just 40K. The temperature decrease also happens very quickly with a falling time below 30µs. The difference between both quantities (peak vs. average) makes it difficult to estimate the mirror performance during a laser irradiation. Such considerations usually work with the cw-equivalent of the pulsed laser and assume average temperature values.

3.5 A pure thermally induced bow change by heating the sample

Previous experiments have already suggested that the bow change is, at least partly, induced by the development of the mirror temperature. So it was obvious to turn the tables, directly to heat a sample and to detect the bow. For this purpose, a SLM is heated from the backside via a peltier element, see fig. 67a. As a reference the CMOS temperature in the substrate is measured. The mirror temperature itself was not detected at this time. But, due to experience within previous experiments it should be slightly lower than the CMOS level. The results are presented in fig. 67b) and show the induced bow change within a thermal cycling. The most important outcome is that there is a pure temperature-induced change of the mirror bow. And within the applied temperature range, the development of the bow is fully reversible. The situation is of course different from a laser exposure and data cannot just compared quantitatively with each other.

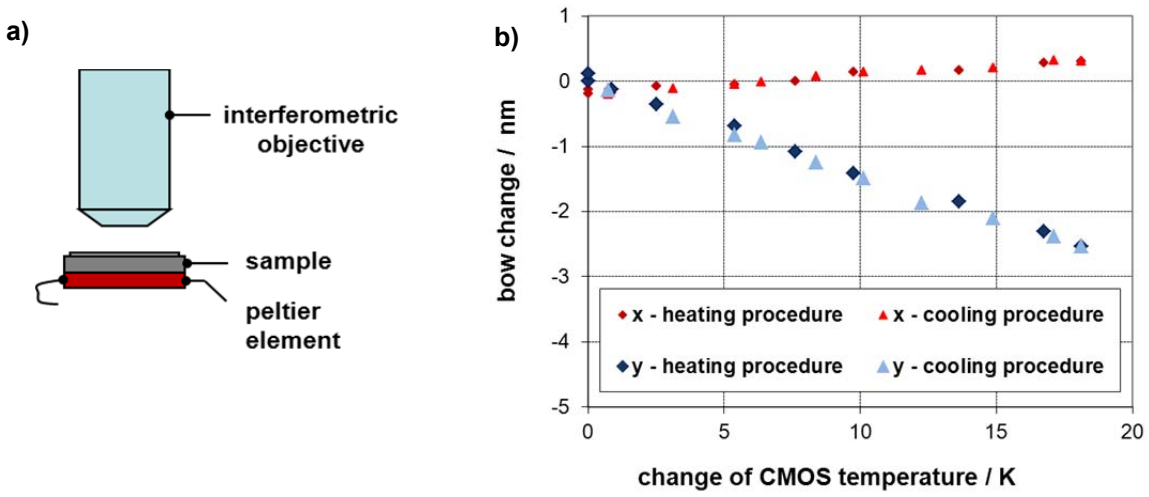

Fig. 67: a) Heating of an SLM from the backside via a peltier element, b) determination of a thermal induced bow change by heating the sample from the backside

There is one question being raised. Why do both mirror axis behave different? Former experiments have shown several times that the mirror's 2-post design can cause a non-symmetric bow change. The observed negative bow change along the y-axis corresponds to the expected result. The higher the temperature level the higher the negative bow change especially along the tilting axis. But there is also this slight positive change along the x-axis. Such a behaviour might arise from the changed direction of the heat transfer. Compared to the laser induced

heating, the heat from the peltier is transferred from the backside through the CMOS plane and probably also through the mirror plane. Along the x-axis the mirror now slightly bends positively. Along the y-axis the conditions are different. During heating the mirror cannot expand undisturbed since it is connected to the yoke layer via the two posts. The material of the underlying yoke layer has a coefficient of thermal expansion smaller than the mirror material. A warming of actuator and mirror can cause the observed negative bow change just along the tilting axis.

4 UV laser-induced degradation of the mirror material

Within the following chapter UV laser induced degradation of the aluminium based mirror material is determined. For this purpose irradiated mirrors and samples with an unstructured Al-x-Si layer are investigated by means of different micro- and nano-analytical techniques such as atomic force microscopy (AFM), reflectometry and transmission electron microscopy (TEM). The x in the alloy term shall indicate that one of the alloying components is defined as confidential.

4.1 Analysis of surface roughness with AFM

The current analysis investigates a possible effect of the laser exposure on the surface roughness of the mirror material. For this purpose, samples were irradiated with a set of laser parameters, shown below in table 15. The roughness is determined locally by analysing an area of $1\mu m^2$ per sample and position with AFM. In fig. 68a below a typical AFM scan is presented. It contains real surface data in x, y and z and is used for roughness analysis. The AFM was operated in non-contact mode and constant amplitude. In fig. 68b the phase signal at same operation mode is depicted (phase imaging). It allows a high-contrast depiction of the grain boundaries and is used for analysing the average grain size.

energy density	laser repetition rate	number of pulses	ambient atmosphere
$10mJ/cm^2$	**1kHz**	**$100 * 10^6$**	**N_2 ($O_2 \leq 1\%$)**

Table 15: Overview about the applied irradiation parameters

Sample - A: unstructured Al-x-Si layer on silicon substrate

As the first sample an unstructured layer of Al-x-Si deposited on a layer of silicon oxide on top of a silicon wafer is analysed. The deposited layer is of the same thickness than the mirror plate. Such a simplified sample enables the analysis of the mirror material without having different limitations in case of free standing single mirrors like mechanical stability. Nevertheless changed experimental conditions need to be considered. The simplified sample exhibits a thermal mass which is orders of magnitude higher than single micro mirrors and allows

the undisturbed heat transfer into unirradiated areas. It is assumed that both peak and average temperature is significantly lower than in case of free standing mirrors.

The measured data for the unstructured layer is presented in table 16 and contains the arithmetic average (Ra), the root mean square (Rq) and the maximum value (Rmax). None of these quantities shows a significant change of the surface roughness caused by the irradiation.

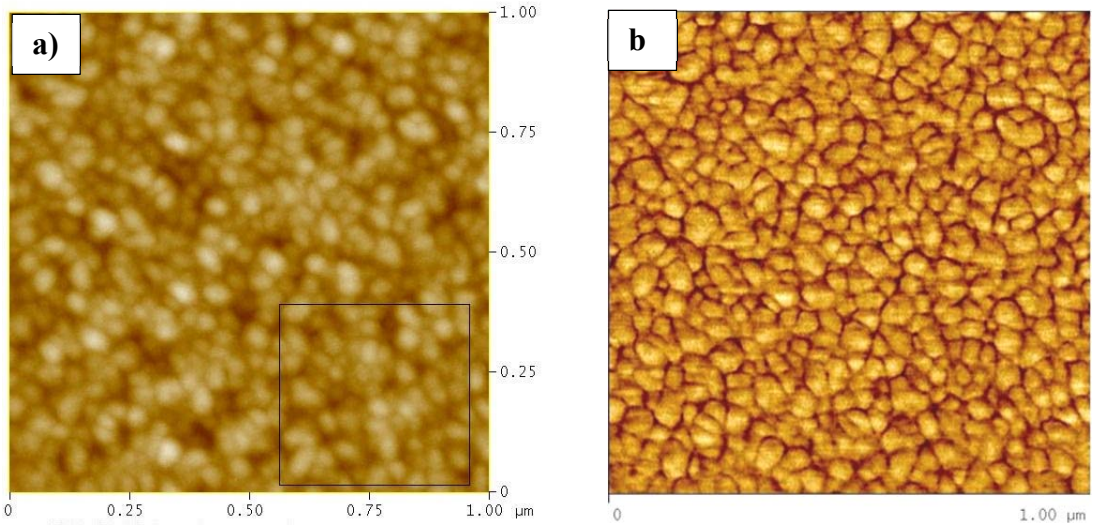

Fig. 68 Determination of local surface topography with AFM (area = 1µm*1µm):
a) non-contact mode with constant amplitude, used for the determination of surface roughness,
b) phase signal in the same operation mode (phase imaging), used for determination of average grain size

	non irradiated	irradiated
	roughness/ nm	
sample 1	Rmax: 14.5 Rq: 2.0 Ra: 1.6	Rmax: 14.3 Rq: 2.0 Ra: 1.6
sample 2	Rmax: 16.0 Rq: 1.9 Ra: 1.5	Rmax: 15.0 Rq: 2.0 Ra: 1.6
sample 3	Rmax: 14.5 Rq: 1.9 Ra: 1.5	Rmax: 14.0 Rq: 1.9 Ra: 1.5

Table 16: Results of roughness measurement using AFM of an unstructered Al-x-Si layer on silicon before and after a laser exposure

Sample - B: real (freestanding) micro mirrors

In a second step real free standing mirrors are analysed the same way. The obtained results are presented below in table 17. There is a small but reproducible tendency towards an increase of the surface roughness. Rq and Ra increases about 0.2nm - 0.3nm, Rmax increases up to 6nm. The difference in the roughness development compared to the unstructured sample might be arisen from the different temperature levels which both sample types run through during the exposure.

	non - irradiated		irradiated	
	roughness/ nm	grain size/nm	roughness/ nm	grain size/nm
sample 1 pos. 1	Rmax: 15.3 Rq: 2.2 Ra: 1.8	x = 40 y = 41	Rmax: 21.0 Rq: 2.4 Ra: 1.9	x = 34 y = 44
sample 1 pos. 2	Rmax: 16.6 Rq: 2.4 Ra: 1.9	x = 40 y = 40	Rmax: 22.4 Rq: 2.4 Ra: 1.9	x = 33 y =46
sample 2 pos. 1	Rmax: 17.6 Rq: 2.3 Ra: 1.9	x = 39 y = 37	Rmax: 22.9 Rq: 2.6 Ra: 2.1	x = 34 y = 43
sample 2 pos. 2	Rmax: 20.8 Rq: 2.4 Ra: 1.9	x = 36 y = 40	Rmax: 21.6 Rq: 2.6 Ra: 2.1	x = 37 y = 53

Table 17: Aerial surface roughness measurement on real free standing mirrors using AFM, before and after a laser exposure

Grain size analysis

Two of the samples (B - real mirrors) were additionally used to determine the average grain size. For this purpose the AFM phase signal (shown in fig. 68b above) was analysed. The analysis was performed by sub-dividing the AFM scan area into 10*10 boxes and counting the number of grain boundaries in each box both along the x- and y-direction. The results are presented in table 17. Before the irradiation the samples showed an average grain size between 37nm – 41nm along x and y. After the irradiation it turned out that the grains became slightly smaller (5nm – 6nm) along the x-axis and slightly bigger (3nm – 6nm) along the y-axis.

Conclusion

Two different types of sample were analysed with AFM. In case of the unstructured Al-x-Si layer on SiO no significant change of the roughness was detected. The irradiation of real (freestanding) micro mirrors resulted in an increase of Rq and Ra about 0.3nm and of Rmax about several nanometers. The different behaviour of both sample types might arise from the laser induced temperature rise, which both sample types run through during the exposure.

Furthermore, the irradiated mirrors showed a slight decrease of the grain size along the x-axis and a slight increase along the y-axis. The notation x and y agrees with the definition in p. 31, which means that the grains get bigger along the mirror's tilting axis. This observation agrees in turn with the former observation that the bow change is also bigger along the mirror's tilting axis at higher energy levels (see p. 63f.). The rising grain size might be a consequence of this.

4.2 Analysis of reflectance by reflectometry

The following section investigates the UV laser induced effect on the material's reflectance of an unstructured Al-x-Si sample. The sample and the irradiation parameters are of the same type as it is described above. The results are presented in fig. 69a with the incident wavelength in x and the resulting reflectance in y. The reflectance was determined with the "Nanospec 8000x" in perpendicular incidence. The unirradiated state is depicted in blue, the irradiated in red. Both states are evaluated by three different samples positions. Within the depicted wavelength range the unirradiated samples show a maximum reflectance of 0.85 at 350nm and a minimum reflectance of 0.75 at 200nm. The irradiated samples shows a slightly increased reflectance for λ > 260nm. For wavelengths < 245nm they show a clearly decreased reflectance with the minimum of 0.63 at 200nm. Around 248nm (irradiating wavelength) the reflectance remains more or less unchanged.

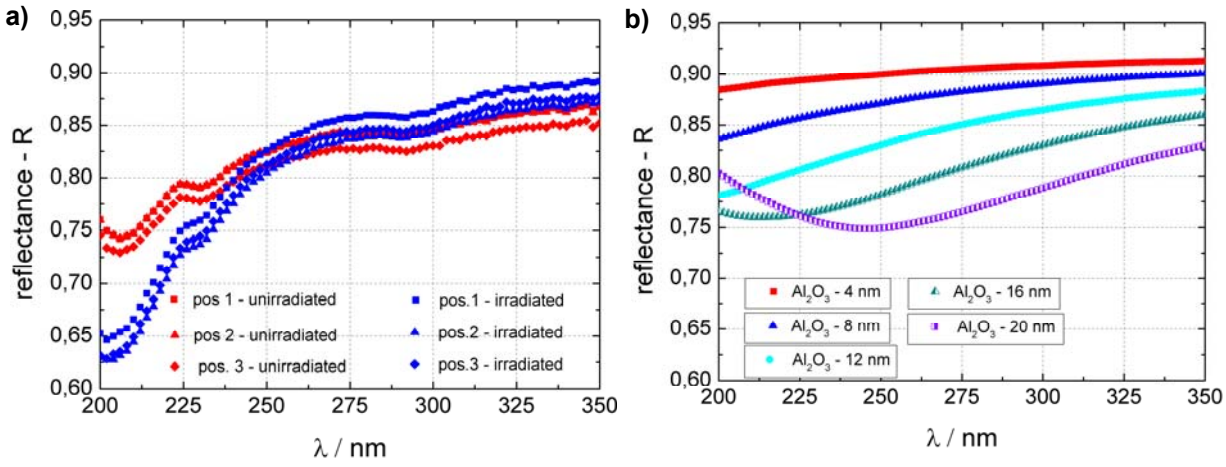

Fig. 69 a) Laser induced degradation of the reflectance of an unstructured sample, b) simulation of the effect of an increasing oxide layer (Al_2O_3) on UV-reflectance

Possible mechanisms to cause a change of the reflectance

In general different mechanisms come into consideration. The most obvious reasons are a change of the surface roughness and a laser induced oxidation. An increase of the surface roughness would probably result in a broadend angular intensity distribution of the reflected signal. Boundary areas of the reflected light could miss the detector and result in a decrease of

the detected intensity or reflectance respectively. But previous investigations have not shown significant changes in surface roughness wherewith it seem not to be responsible.

Another obvious reason is a laser induced oxidation on top of the sample surface. Such an additional oxide layer could act as an absorber and also as an interference layer. Due to its low absorption coefficient of about 10^{-1} cm^{-1} in the UV region [59] the resulting absorption by passing a layer of some nanometer is not significant. But with a refractive index of about 1.8 in the UV region [38] an oxide layer of some ten nanometer would soon form an artificial interference coating. To evaluate the effect of an increasing oxide layer a simulation with varying oxide thicknesses is carried out (see fig. 69b above). The simulated sample consists of a Si substrate, an aluminium layer of 700nm and a layer of Al_2O_3 on top. The thickness of the oxide layer is varied from $4nm \leq z \leq 20nm$ with an assumed surface roughness of 2nm (rms). The applied material constants come from [38]. The minimum layer of 4nm represents an unirradiated sample covered with a natural oxide. The maximum assumed thickness of 20nm is a real measured quantity and was determined by TEM analyses of an irradiated mirror plate (see p. 99).

The general outcome of the simulation is that a rising thickness of Al_2O_3 up to 18nm reduces the reflectance within the considered wavelength range. For z = 20nm there is a minimum at 245nm. An effect of the rising oxide layer on the reflectance seems to exist. But the simulation only partially agrees with the observed changes at the irradiated samples. Its informative value is limited.

4.3 Analysis of the mirror plate with TEM

The following chapter discusses degradation analysis of the mirror material by Transmission electron microscopy (TEM). The aim of this analysis is to investigate the laser induced effect on grain structure, interfacial layer and distribution of alloying components within the mirror plate. For the current analysis two irradiated and two non-irradiated reference samples were investigated at the Fraunhofer Institute for Ceramic Technologies and Systems (IKTS) and at Helmholtz-Zentrum Dresden-Rossendorf (HZDR). The sample irradiation was carried out with the set of laser parameters summarized below.

energy density	laser repetition rate	number of pulses	ambient atmosphere
10mJ/cm^2	**1kHz**	**100 * 10^6**	**N_2 ($O_2 \leq 1\%$)**

Table 18: Overview about the applied irradiation parameters

4.3.1 Sample preparation by focused ion beam (FIB)

TEM analysis requires a very thin, electron transparent sample. The required sample thickness depends on the aimed resolution and the material's density. For high resolution TEM the sample needs to be thinned to the range of 100nm and below. This complex preparation procedure of the specimen is done by focused ion beam (FIB) techniques. Such a FIB instrument looks and operates much like a scanning electron microscope (SEM). Both instruments rely on a focused beam to create a specimen image; an ion beam in case of the FIB and an electron beam in case of the SEM. The procedure consists of the following two process steps/ techniques:

- 1 deposition of a protection layer via ion beam assisted chemical vapour deposition and
- 2 laying bare and thinning of the specimen via ion beam sputtering

The ion beam is realized with Ga ions, coming from a liquid metal ion source (LMIS) [60]. The first step, the deposition of metal, is used in both SEM and TEM specimen preparation techniques to protect the top surface of interest from spurious sputtering. See fig. 70a), where

a protection bar is deposited across the mirror surface. Therefore a needle is brought to within 100µm–200µm of the target surface. Than a suitable gas (e.g. $W(CO)_6$) is injected from the needle and adsorbs onto the target surface. The Ga^+ beam is rastered along the desired specimen region and decomposes the gas. A deposited layer of metal is left behind (e.g. W) while the by-product (e.g. CO) is removed through the vacuum system. Other conductors (e.g. Pt, Al, Cu and C) and insulators (e.g. SiO_2) can also be used as deposition materials. In the current case Pt is deposited as the protection layer.

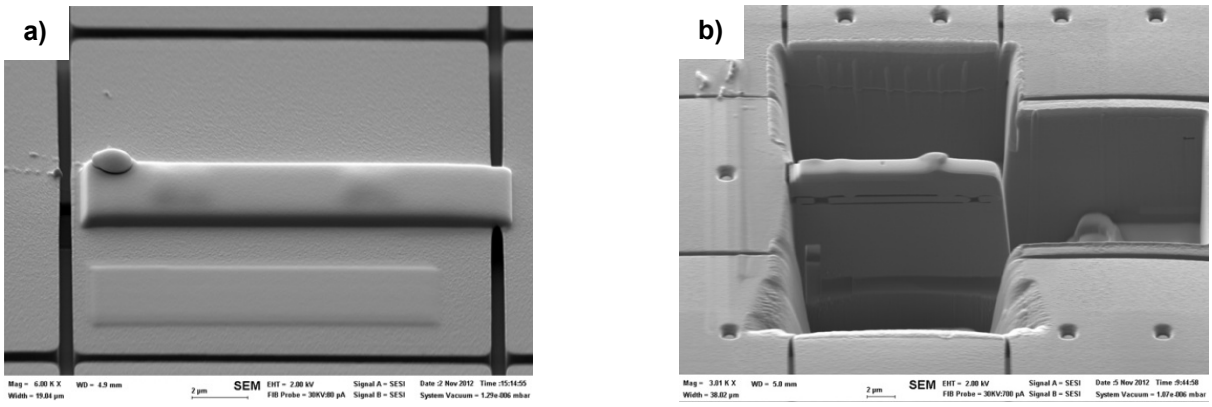

Fig.70: Preparation of the mirror by Focused Ion beam techniques (FIB): a) deposition of a bar (protection layer), b) laying bare and thinning of the specimen with the ion beam

In step #2 the ion beam is accelerated towards the targeted area around the protection bar (fig. 70b). Ga ions enter the sample and create a cascade of events resulting in the ejection of sputtered particles, which may be ions or neutral atoms. The result is a thin lamella in the range of a micron which is still connected to the sample on one side. The sputtering mechanism also results in Ga^+ implantation into the sample which needs to be considered during the sample analysis. The preparation of the homogeneously thinned slice itself is done by the so called "lift-out" technique, see [60].

Fig 71 below shows an overview of the TEM lamella with the protection layer on top, the mirror plate, the mirror post and the torsional springs underneath.

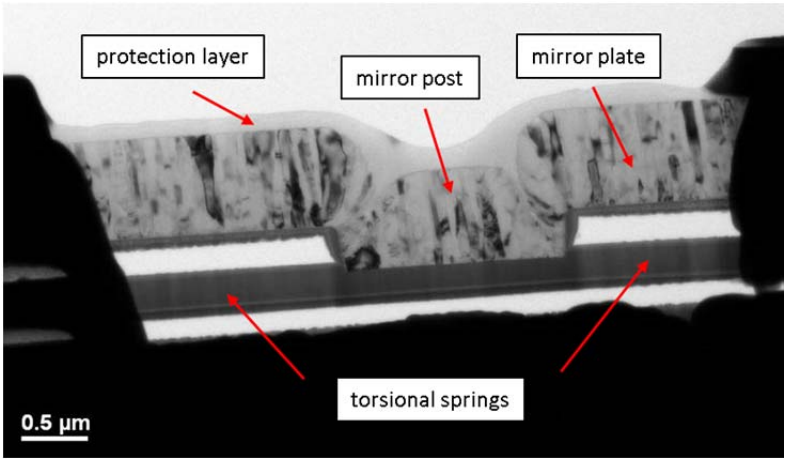

Fig.71: Overview of the TEM lamella with the protection layer on top, mirror plate, mirror post and torsional springs

4.3.2 Analysis of the grain structure

Grain structure before a laser exposure

The following sections discusses the grain structure before and after a laser irradiation. The non-irradiated samples show columnar crystals with a diameter of about 50nm ± 20nm and a rather uniform grain growth. Within the first 100nm above the nucleation zone there is a zone of growing grain size until the dominating grains reach the final thickness. Subsequently the grain size remains more or less constant along the metal film, see fig.72a and b below.

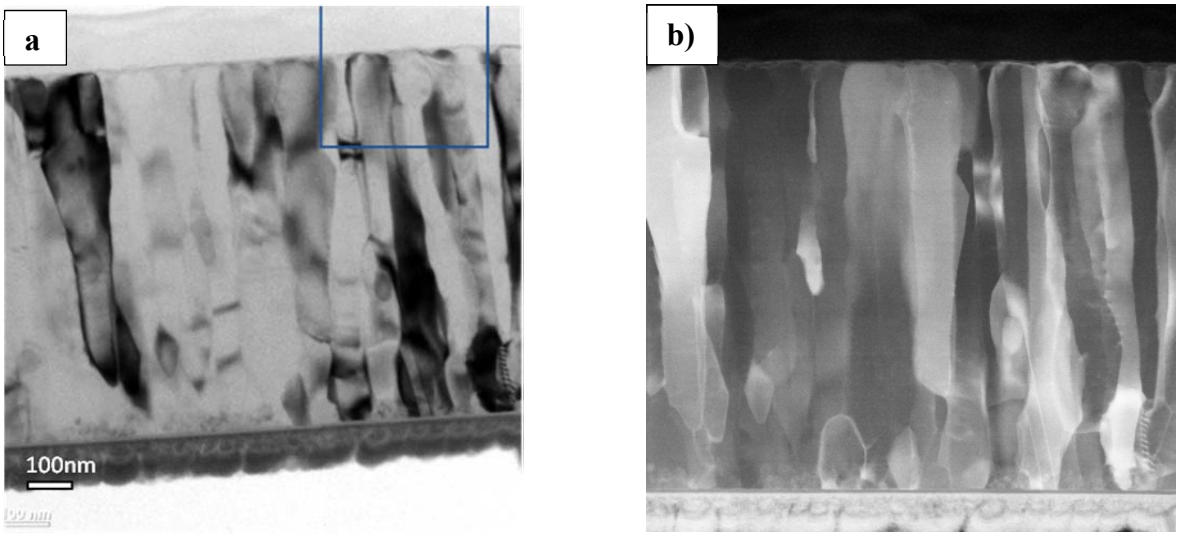

Fig. 72: Grain structure before a laser irradiation a) bright field image, b) dark field image

Contrast formation

The contrast formation of amorphous samples comes from variation in the sample thickness (absorption contrast) and variations in the materials density (atomic number contrast). For crystalline samples there is an additional contrast formation by diffraction of the electron beam on the atomic lattice. All these three factors are summarized as scattering-absorption contrast. Fig. 72a) is taken by applying the bright field modulus (BF). Here, the focused electron beam hits the sample perpendicular and just the less diffracted and less scattered part of the beam reaches the detector and contributes to the image. Fig. 72b) is taken with dark field modulus (DF) where the intensively diffracted and scattered portions contribute to the image. The contrast formation between different grains in case of this crystalline aluminium alloy mainly originates from diffraction on lattice planes.

The following two pictures (fig. 73a, b) show the lower end of the cross section with the lower boundary layer, the nucleation zone and the zone of growing grain size. Below the boundary layer there is a zone of amorphous material. This material was probably redeposited during the sputtering process (sample preparation).

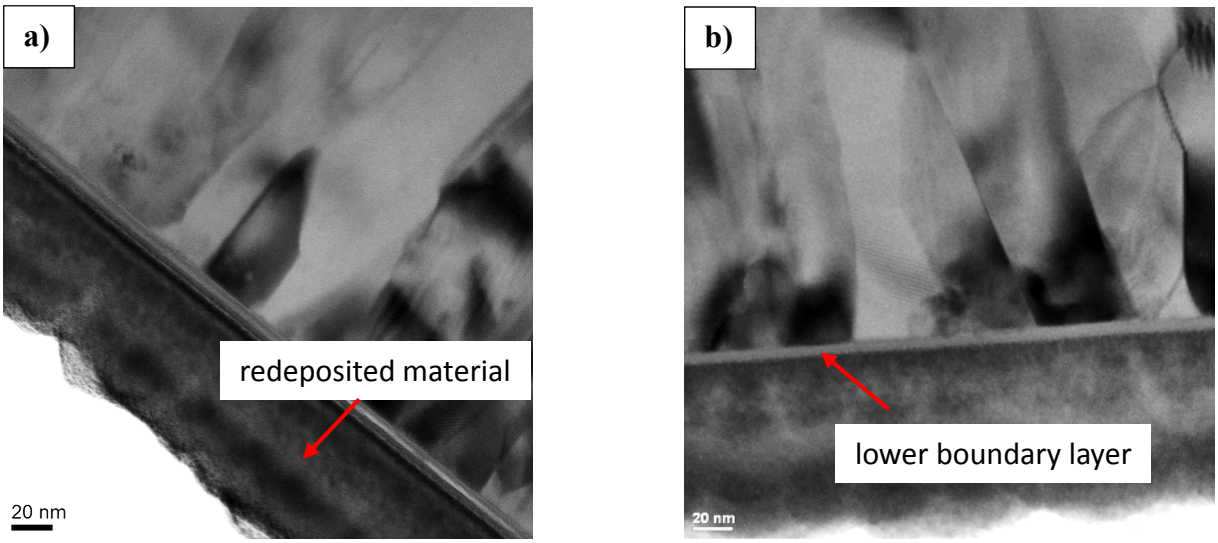

Fig. 73: Detailed image of the lower end of the mirror cross section with the nucleation zone, lower boundary layer and a layer of an amorphous material redeposited during sample preparation

Compared to the homogeneous grain structure of the mirror plate in itself the intersection between mirror plate and mirror post shows a rather inhomogeneous crystal growth. On closer

inspection one even recognizes a void between both sections, which takes half of the mirror thickness (fig. 74). This void might be a point of attack for additional corrosion by H_2O and O_2.

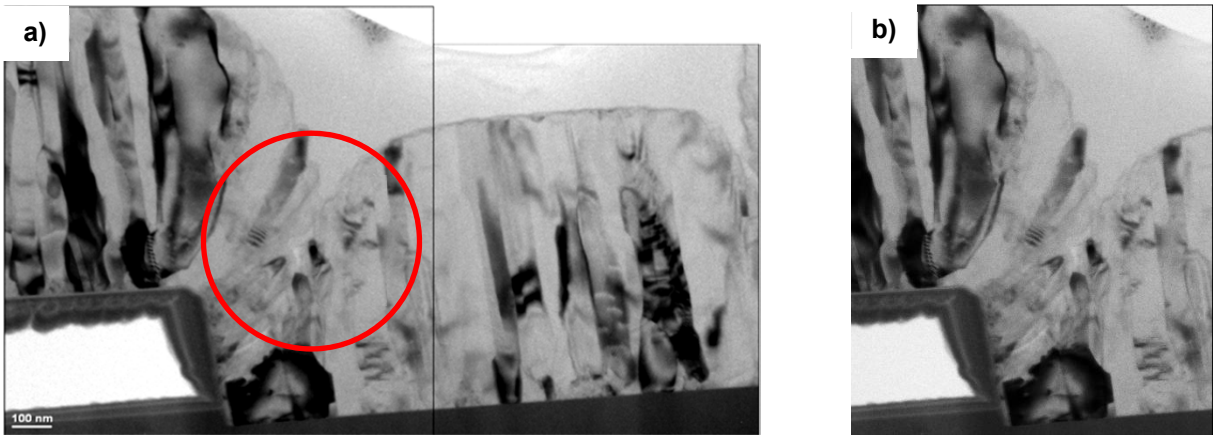

Fig. 74: Inhomogeneous grain growth within the intersection from mirror plate to post

Grain structure after the laser exposure

After the exposure the crystals do not show an obvious change in their structure. Fig. 75 below shows the grain structure in BF (a) and DF (b) modulus. The grains still show their former homogeneous formation. The grain size seems not to have changed dramatically but now appears slightly smaller.

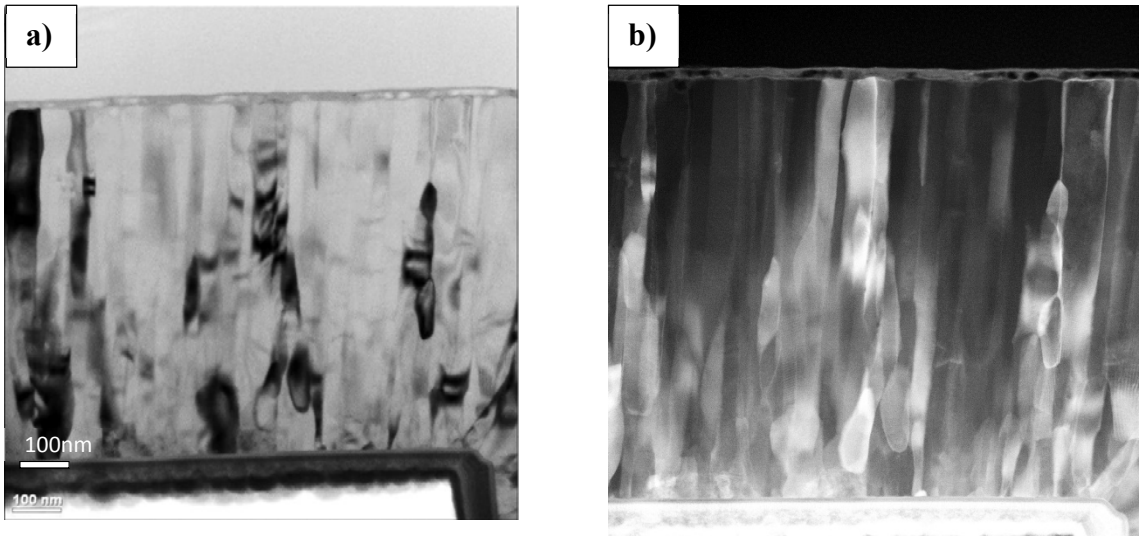

Fig. 75: Grain structure after the laser irradiation: a) bright field image, b) dark field image

Any serious statistically conclusions about the grain size cannot be made by these pictures. But this impression would agree with the AFM measurements. There the phase image has shown that the grains became slightly smaller (5nm – 6nm) along the x-axis and slightly bigger (3nm – 6nm) along the y-axis (see p. 89). Further phenomena like recrystallisation are not noticed.

4.3.3 Analysis of the boundary layer

All metallic surfaces (except the precious metals) show a naturally grown oxide layer on top when getting in contact with the atmospheric oxygen. The aluminium samples in the present case additionally have a protection layer (Pt) on top and the oxide also might exhibit Ga+ coming from the sample preparation (see p. 94f.). The following section will discuss the so called boundary layer, which includes the layer between the crystalline aluminium and the amorphous protection layer (Pt) before and after a laser exposure.

Boundary layer – non irradiated

The non-irradiated boundary layer has a thickness of a few nanometers (≈ 5nm) which matches to the thickness of a naturally grown aluminium oxide. Fig.76a shows the upper part of the lamella with crystalline aluminium grains and the amorphous boundary layer in BF modulus. Fig. 76b shows a detail in high resolution TEM (HR TEM) and makes the aluminium lattice planes visible.

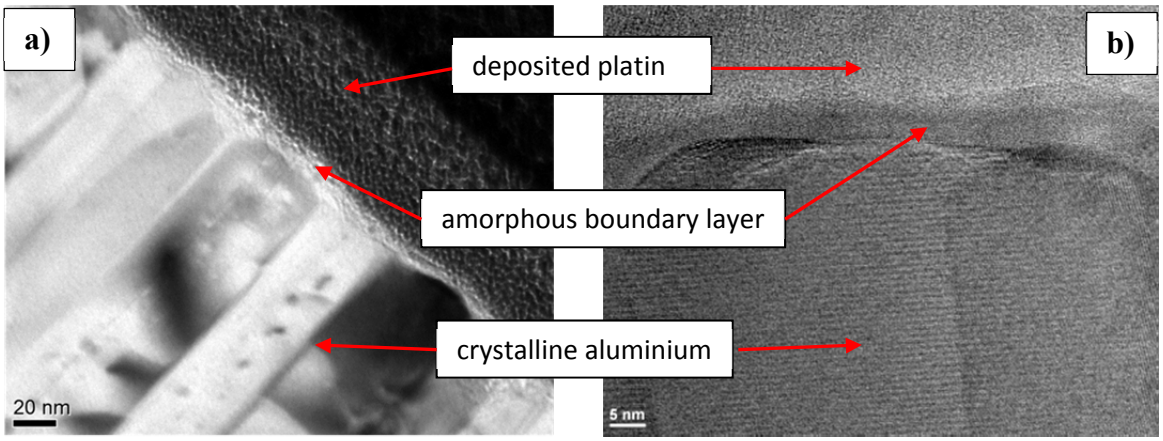

Fig. 76: Upper part of the lamella with aluminium grains and boundary layer – non irradiated:
a) TEM in BF modulus, b) aluminium lattice planes and amorphous boundary layer in high resolution

Boundary layer – irradiated

After the irradiation the thickness of the upper boundary layer has increased significantly. The post exposure thickness is in the range of 15nm to 20nm. This height slightly varies along the sample according to the mirror roughness (see fig 77a, b). Such a significant growth is not observed at the lower boundary layer. Its thickness remained more or less unchanged or rose insignificantly (see fig. 77c, and 75a, b). Consequently the irradiated mirrors exhibit obvious differences between their upper and lower boundary layer.

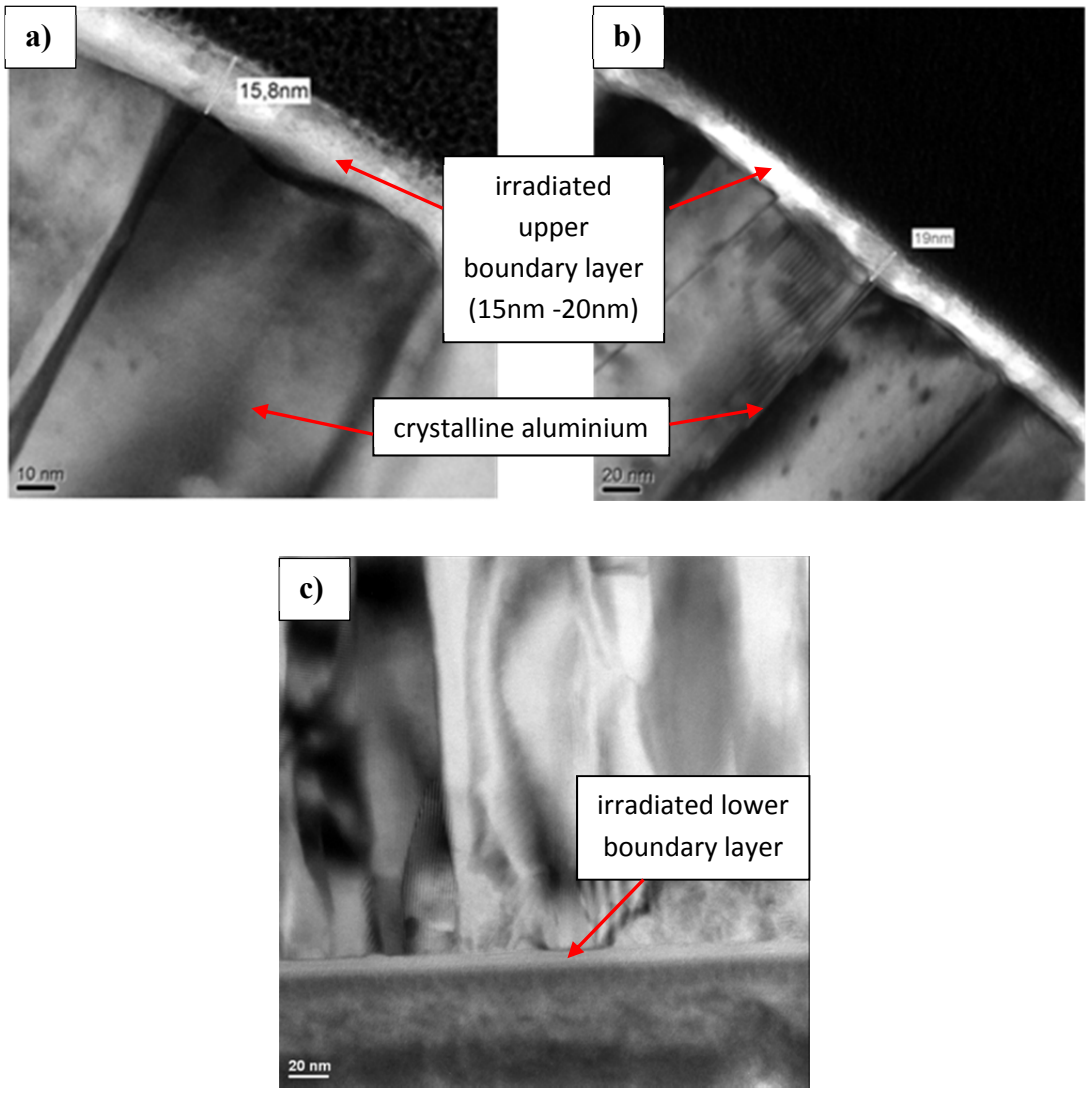

Fig. 77: Boundary layer after the irradiation: a), b) upper boundary layer with a thickness of 15nm to 20nm, c) lower boundary layer, without a significant rise in the layer thickness

Possible effect of sample preparation on boundary layer

The boundary/ oxide layer is in general, not free of an impact, coming from the sample preparation. The preparation definitely includes the introduction of platinum into the boundary layer. But to keep the effect small the platinum deposition was carried out in two steps with a first (softer) e-beam assisted and a second (more efficient) ion beam assisted procedure. Furthermore, all samples (irradiated and reference mirrors) have run through the same procedure. Consequently it can be assumed that the observed growth is a real laser driven effect.

Roughness, pores and crystalline inclusions

Another irradiation induced effect is the numerous formation of pores and crystalline inclusions within the grown boundary layer. Fig. 78a shows the lamella with many pores, marked by red arrows. Fig. 78b shows the porous layer in detail. Again this effect is only observed at the upper boundary layer.

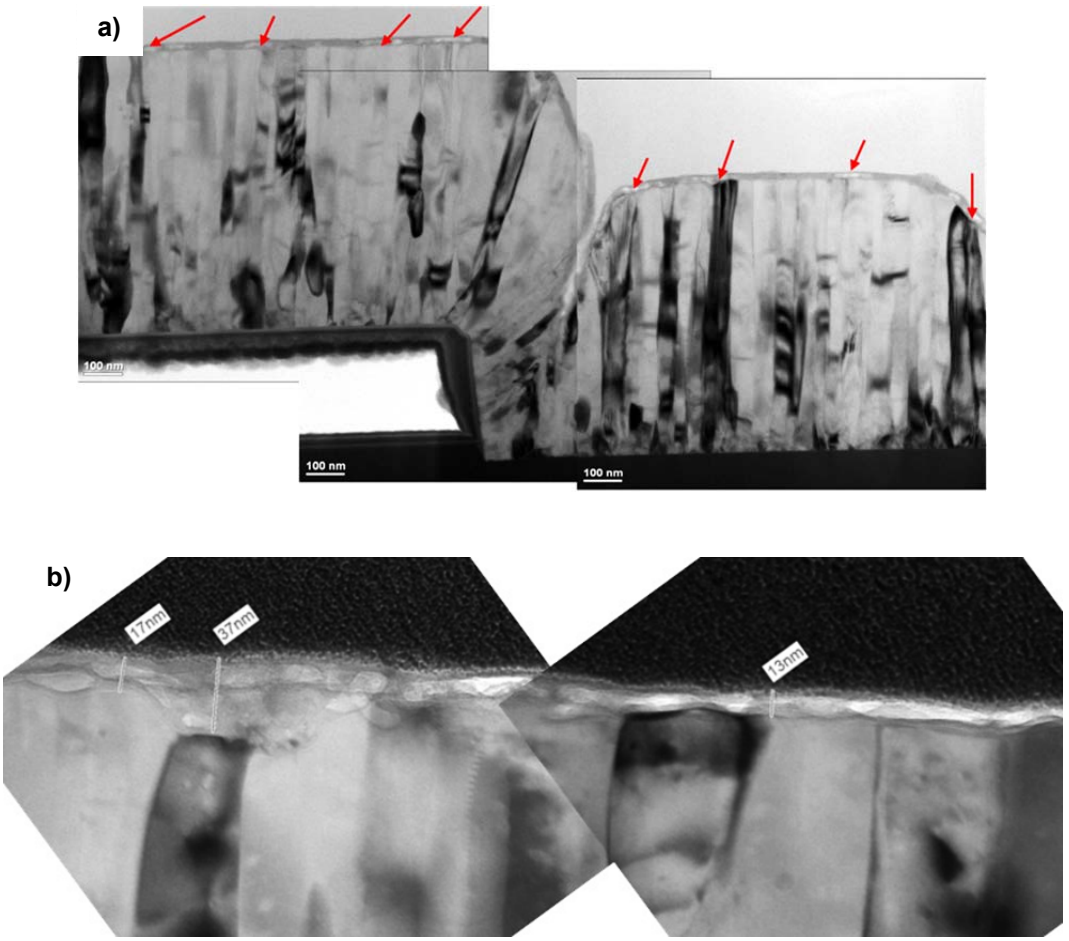

Fig. 78: a) Irradiation induced formation of pores within the boundary layer (marked with red arrows), b) detailed image of the porous oxide layer

Fig. 79 below shows pores and crystalline inclusions in high resolution. In BF modulus the pores appear somewhat brighter than the surrounding material (a). This means the pores are either really empty or filled with a material which is less absorptive or less dens to the electron beam. With the atomic number of 6 (aluminium = 13, oxygen = 8) carbon would be imaginable as such a material. The lattice planes of such a crystalline inclusion are imaged in fig. 79b.

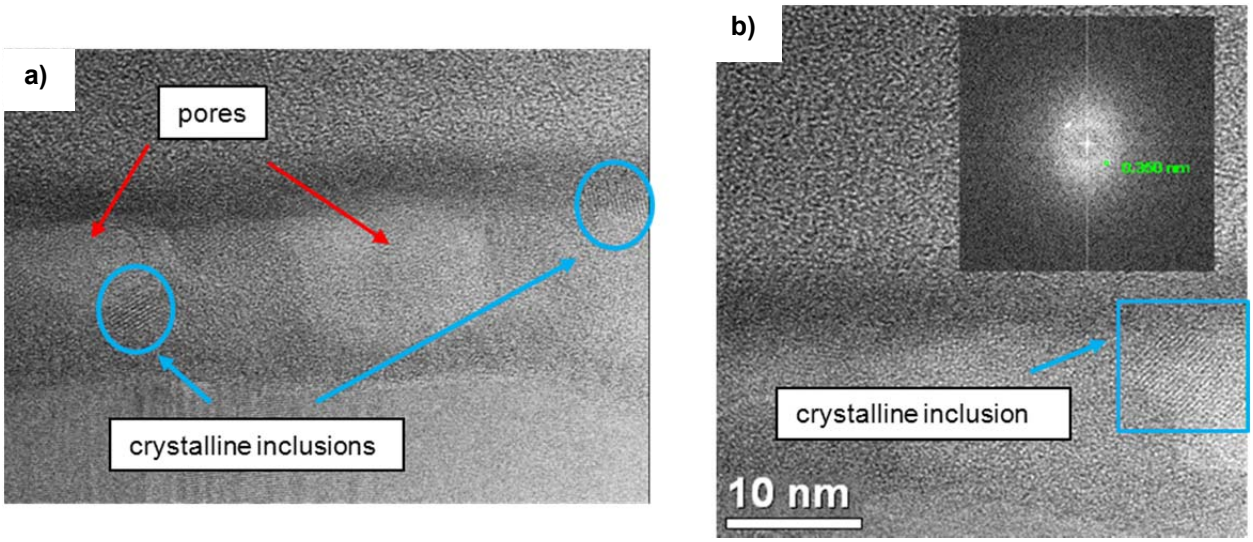

Fig. 79: a) Pores and crystalline inclusions within the grown boundary layer, b) distances of adjacent lattice planes of crystalline inclusions = 0.35nm

The distance of adjacent lattice planes of a crystalline material can be used to identify the material or compound respectively. Such a measurement was performed in fig. 79b and resulted in a distance of 0.35nm. This value excludes aluminium as the crystalline material but allows a group of possible compounds. From this group the compounds Al_2O_3 and AlF_3 are the most likely ones see table 19. The formation of AlF_3 is quite conceivable since fluor is known to be typical contaminants of MEMS surfaces.

	space group	a	c	d012
Al_2O_3:	167	0.4758nm	1.2991nm	0.3479nm
AlF_3:	148	0.4928nm	1.2445nm	0.3517nm

Table 19: Properties of crystal structure of Al_2O_3 and AlF_3 including the space group unit cell and orthogonal distance d of adjacent lattice plane for a certain miller index [62, 63]

4.3.4 (Space-resolved) element analysis

The following section describes the analysis of the irradiated TEM lamella via Energy-dispersive X-ray spectroscopy (EDX). EDX is a technique for elemental or chemical characterisation of a specimen and belongs to the group of X-ray spectroscopy. Atoms inside the specimen, which are excited by a homogeneous electron beam, emit X-rays with a material specific energy, the characteristic radiation. The peaks in the obtained spectrum give information about the element distribution within the analysed sample volume. The detection limit of the used system for a certain element is in the range of 2at% -3at%. The characterization was unfortunately only carried out at the irradiated samples, so that there is no comparison of the state before and after the irradiation. Two different analyses were carried out. The first analysis investigates the upper boundary layer and compares it with the metallic aluminium alloy underneath (see fig. 80a and fig. 81). The second analysis compares the alloy at different regions within the lamella (see fig. 80b, fig. 82). Fig. 80 below shows the location of the investigated regions within the lamella for both analyses.

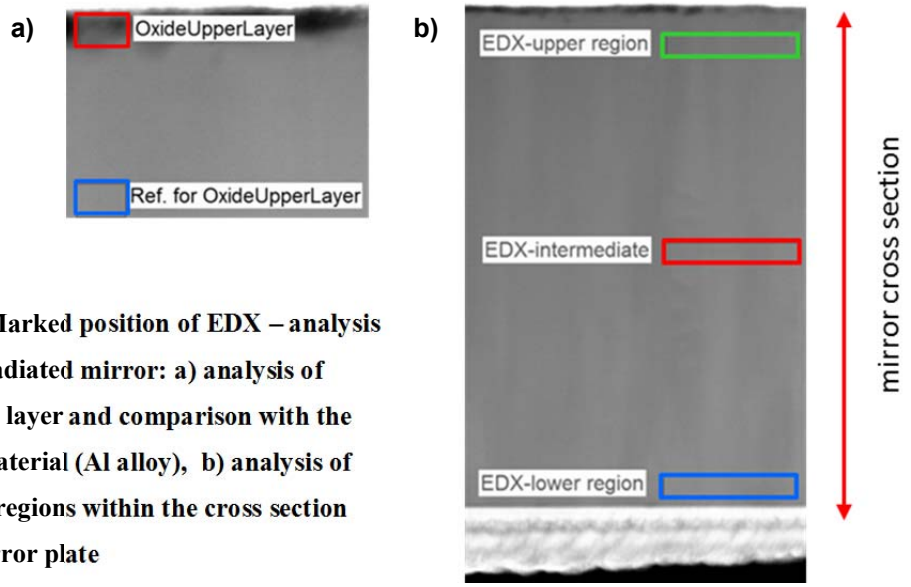

Fig.80: Marked position of EDX – analysis of the irradiated mirror: a) analysis of boundary layer and comparison with the mirror material (Al alloy), b) analysis of different regions within the cross section of the mirror plate

EDX analysis of boundary layer and comparison with the metallic mirror material

The elemental analysis of the upper boundary (oxide) layer is shown in fig. 81 with the red graph. The graph shows the element specific counts on the y- and the corresponding photon energy on the x-axis. There are three peaks which do not belong to the sample but originate

from the sample holder. It is Cu at 8keV and Pt at 2.1keV and 9.4keV. The boundary layer shows the highest peaks for aluminium and oxygen whereby it can be identified as aluminium oxide. Furthermore there is silicon and small quantities of magnesium, fluorine and carbon.

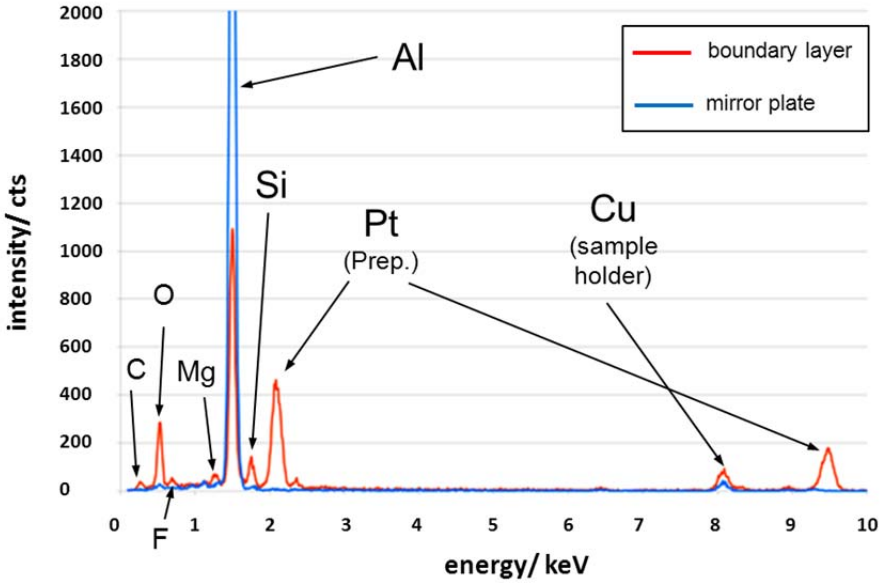

Fig. 81: EDX analysis of the boundary layer and comparison with the mirror material (Al alloy)

Silicon and magnesium as the alloying components are also components of the oxide. Carbon contamination is a general problem of MEMS and optical surfaces. Rests of fluorine probably come from an etching process where a sacrificial layer from underneath the mirrors is removed.

The elemental distribution of the metallic aluminium alloy as a reference to the oxide layer is shown by the blue graph. As expected there is a massive peak for aluminium with the top exceeding the range of the y-scale. There is no peak for the alloying components. A possible reason is a lower amount of the alloying components within the metallic layer than within the oxide.

Concentration of the alloying components within the mirror plate

Within the second EDX analysis different regions of the metallic layer (upper, intermediate and lower region of the lamella) are compared with each other. The aim is to investigate possible inhomogeneous distributions of the alloying components. From former investigations it is known that silicon shows a higher concentration within the lower area of the mirror. The analysis is presented in fig. 82 below. The relevant peaks are Al, Si and O. The upper (green)

and intermediate (red) region show almost no differences in the elemental distribution. However, the lower region (blue) shows significantly more Si (≈ 350 counts compared to 100 counts above). Since there is just an EDX analysis of the irradiated sample it is not for sure whether this is a laser induced effect.

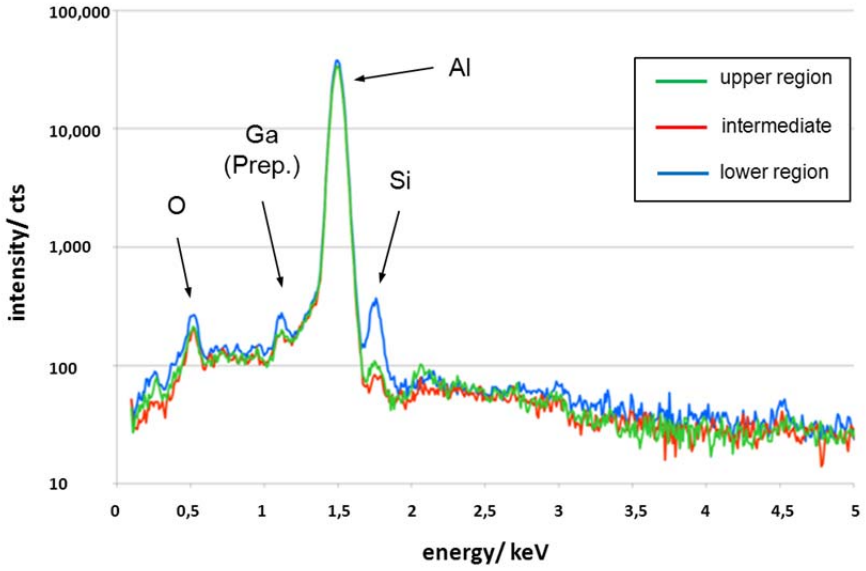

Fig. 82: EDX analysis of the irradiated mirror, comparing different regions of the TEM lamella

An additional EDX analysis is presented in fig. 83 below. This analysis of a non-irradiated mirror was done at IPMS with REM-EDX. The analysis compares the mirror front (green) and back side (red) and also shows a bigger Si peak at the mirror back side/ lower part of the mirror plate. Hence the result of the TEM-EDX (fig.82) which also detected a higher concentration of Si close to the mirror back side, was reproduced and is a real effect.

Conclusions

The irradiation seems not to have changed the structure or size of the metallic grains dramatically. Before and after the irradiation the samples show columnar crystals and a rather uniform grain growth. After the irradiation the grain size appears somewhat smaller but any serious statistically conclusions cannot be made by these TEM pictures.

The non-irradiated amorphous boundary layer has a thickness of a few nanometers (≈5nm) and is assumed to correspond to a naturally grown oxide (apart from possible effects of the

sample preparation). After the irradiation the thickness of the upper boundary layer has risen to 15nm-20nm. Such a significant growth is not observed at the lower boundary layer. Consequently the irradiated mirrors exhibit obvious differences between their upper and lower boundary layer. Another irradiation induced effect is the numerous formation of pores and crystalline inclusions within the grown boundary layer. This effect is again only observed at the upper boundary layer.

The comparing EDX analysis of upper boundary layer and the crystalline mirror material resulted in the identification of the boundary layer as aluminium oxide. Within the crystalline material the aluminium peak overshadows the entire EDX signal. Obvious peaks of the alloying components were not resolved. Also possible is that the concentration of the alloying components (relative to aluminium) is higher in the boundary layer than in the crystalline area. The EDX analysis of different zones within the crystalline material detected a higher concentration of Si close to the mirror back side. Another REM-EDX analysis of a non-irradiated mirror reproduced this result and showed that this inhomogeneity of the Si distribution seems not to be an irradiation induced effect.

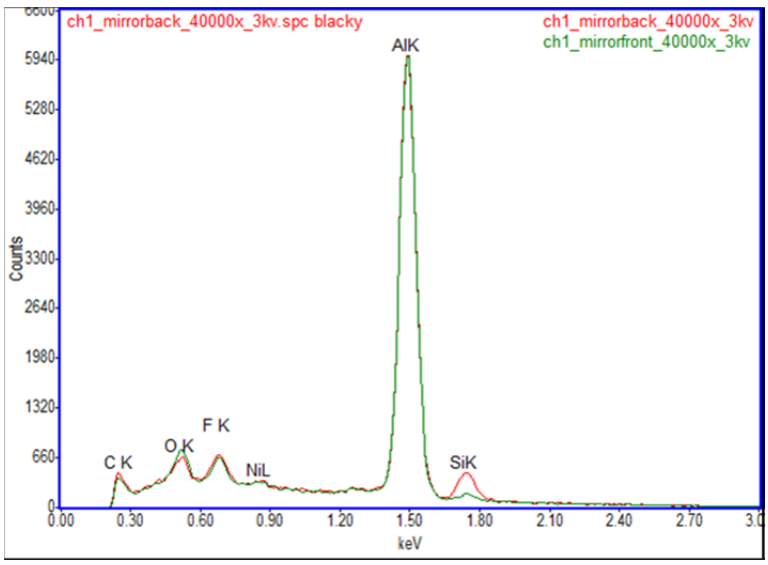

Fig. 83: EDX analysis of mirror front (green) and backside (red) of an unirradiated mirror, showing a bigger Si-peak at the backside signal [73]

5 Discussion

5.1 Fundamentally observed behaviour on irradiated micro mirrors

5.1.1 Change of the mirror bow during a laser exposure

A general conclusion of the irradiation experiments is that a minimum energy density of $10\mu J/cm^2$ (at a repetition rate of 1kHz) is required to detect any laser induced change of the micro mirror bow (see p. 58, 60). In principal a bow change in both directions (positive and negative) is possible and just depends on the applied irradiation parameters (see the definition on p. 31). This statement is of course limited to the specific combination of investigated MEMS/ mirror and laser.

At least three different physical mechanisms were identified as the origin for the particular bow development at the particular irradiation conditions. Depending on the applied energy level one can roughly distinguish between a rather positive tendency (concave) for the lower energy levels ($\leq 1mJ/cm^2$) (see p. 60) and a rather negative tendency (convex) for the higher energy levels ($> 1mJ/cm^2$, see p. 63f.). Another parameter on the direction of the bow development is the deposited energy (dose).

When a sample or a certain position on a sample is irradiated for the first time it shows a complete different behaviour than during following exposures. This difference can regard the direction and the quantity of the bow change.

Furthermore, it was observed that the bow change is not equal in both axis of the single mirror, see fig 84 below (or see p.60f., 63f., 67, 72.). There is a bigger bow change along the mirror's tilting axis (y-axis). The 2-post design is assumed to be the origin of this difference. The laser induced heating results in an expansion of the mirror plate which occurs undisturbed in the mirror's x-direction. In the y-direction there are the two posts with a certain temperature gradient between top (mirror) and bottom (yoke). The expansion of the material between the posts results in an introduction of an additional negative bow change just in the y-direction. This effect is particular visible during the first pulses of an exposure and directly after the exposure is stopped, where the change of the mirror temperature goes on the quickest. This difference in the bow development vanishes after a while. During the long-term exposure

with > 100*10^6 pulses it turned out that the effect seems not to be significant in the long run anymore.

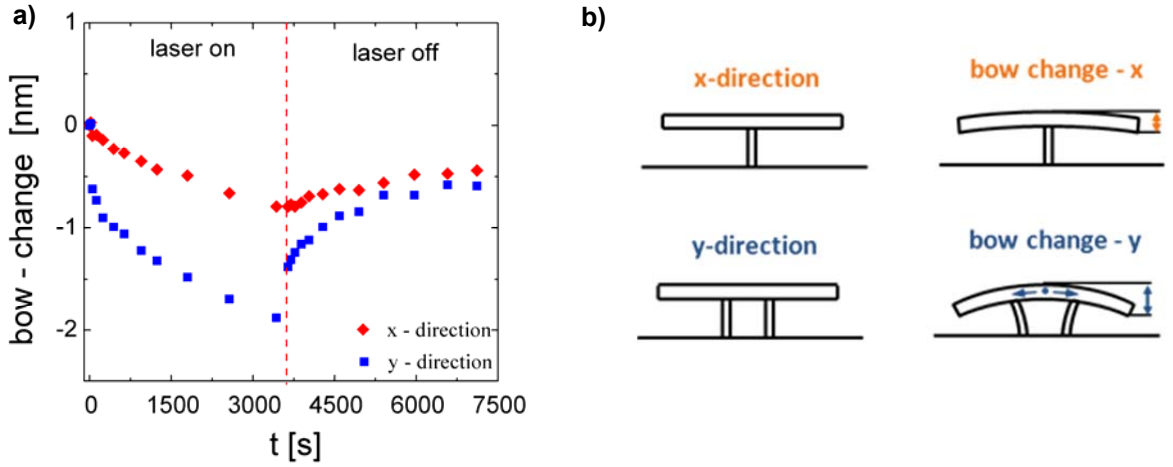

Fig. 84: Level of bow change depending on the mirror axis (at 10mJ/cm^2 and 1kHz): a) increased activity along the tilting axis, (y-axis), b) 2-post design is assumed to be the origin of the different performance

5.1.2 Change of the mirror bow after a laser exposure

After finishing the exposure there is again a change of the mirror bow in answer to the again altered circumstances. The general tendency of the past exposure bow change is in positive direction. One can distinguish two types of the past exposure bow change. For "lower" energy levels (≤ 1mJ/cm^2) there is a "continuative tendency" (see p. 60f.). Here, the past exposure development shows the same direction as the bow change during the exposure itself. However, "higher" energy levels, which go along with a distinct negative bow change during the exposure, show a relaxation of the bow afterwards, which means in the opposite direction (p. 63f.). The relaxation curve is similar to the charging curve of a capacitor, rapid in the beginning and then slowing down. The relaxation can last very long (even several days) compared to an irradiation sequence of just an hour (see p. 73).

5.2 Effect of the specific irradiation parameters on the bow change

5.2.1 Bow change as a function of energy density and the deposited energy

As mentioned above, the laser induced change of the mirror bow can theoretically occur in positive as well as in negative direction (see definition on p. 31). The parameters which dominate the direction are the energy density and the deposited energy. For a serious consideration both types need to be discussed separately.

Positive bow change during the first pulses

For all investigated energy levels the mirrors show a positive bow development during the "first laser pulses". The higher the energy level the quicker the bow change (see fig. 85a, b below and p. 58f.). After the rapid rise of the bow at the beginning the mirrors behave completely different, depending on the applied energy density. For the low energy levels (≤ 1mJ/cm^2) the rate of change now slows down (fig. 85a). For the high energy levels (> 1mJ/cm^2) the initial positive development turns around and changes into the negative direction. The higher the energy level the quicker the turnaround occurs (fig. 85b). It seems that during the first pulses the mirrors run through a unique conditioning process which is sensitive to the deposited energy.

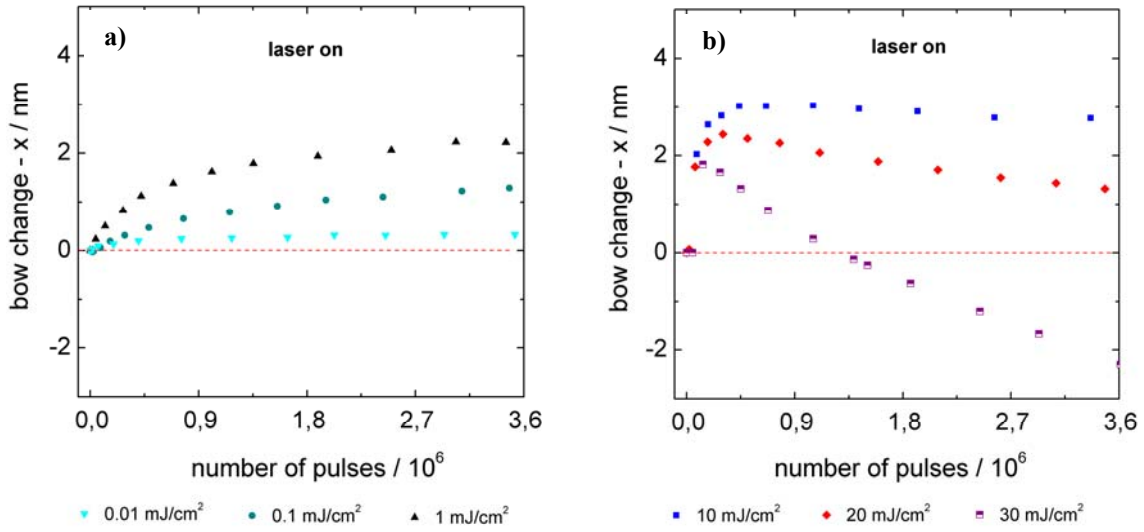

Fig. 85: Positive bow change during the "first" laser pulses as a function of the pulse number a) for lower energy levels (≤ 1mJ/cm^2), b) for high energy levels (> 1mJ/cm^2)

For a review of this hypothesis the results from 85a, b are depicted as a function of the deposited energy in fig. 86 (initially presented in p. 62). All curves show a similar development within a dose of $5*10^3 J/cm^2$. The further increase of the dose up to $10^4 J/cm^2$ has almost no effect on the bow. Only for the highest energy levels the coming turnaround gets visible.
It is assumed that the positive bow change is a permanent modification of the material properties which seems to happen within the first $5*10^3 J/cm^2$. After that this process seems to slow down (low energy levels) or is replaced by another mechanism (high energy levels). The discussion of the specific mechanism is done on p. 113ff.

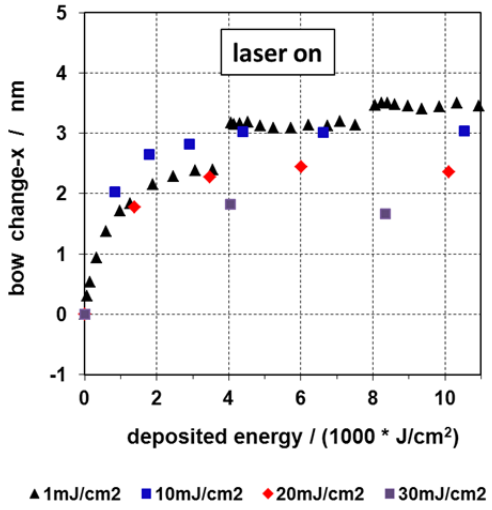

Fig. 86) Positive bow change during the "first" laser pulses as a function of the deposited energy

Turnaround and negative bow change

As described above, at high energy levels (>1mJ/cm^2) the mirrors show initially a positive development as well. But this tendency ends after a deposited dose $\geq 5*10^3 J/cm^2$. Then the development turns around and from now on the bow changes in negative direction as long as the sample is irradiated (see page 63f. and fig. 85b above). For each following irradiation cycle the bow changes in negative direction right from the beginning.

The questions is: Where does the turnaround and the following negative bow change at higher energy levels come from?

What we see is probably the superposition of two different effects. Up to 1mJ/cm^2 the "mirror conditioning process" is dominating and mirrors bend positively. But for 10mJ/cm^2 and high-

er levels the laser induced temperature rise becomes significant and introduces a second effect resulting in a bow change in the negative direction. The formation of this temperature–driven effect is discussed separately on p.116ff.

Relaxation of the bow change:

The energy level does not just effect the bow change during the exposure but also the post exposure development. As long as a certain energy level of about10mJ/cm^2 - 20mJ/cm^2 and a certain pulse number of a "few million" pulses is not exceeded, the occurred negative bow change relaxes more or less completely within 24 hours (see p.63f. and fig 87 below). Generally, this is not a relevant time scale, but it turned out that up to such an energy level the starting bow values of all irradiation cycles (days) where at the same level and resulted in an almost horizontal tendency of the graph in the long run. Remember that between each irradiation cycle there was a break of one day.

When the applied energy level gets larger than 20mJ/cm^2 the negative bow change within one irradiation cycle accumulates to 10nm. At the same time the relative relaxation of the previous cycle becomes smaller. In the long run of several irradiation cycles the development now shows a permanent negative tendency. It is assumed that the increasing and lasting distortion of the mirrors exceeds the material's yield strength, resulting in creep and a plastic deformation.

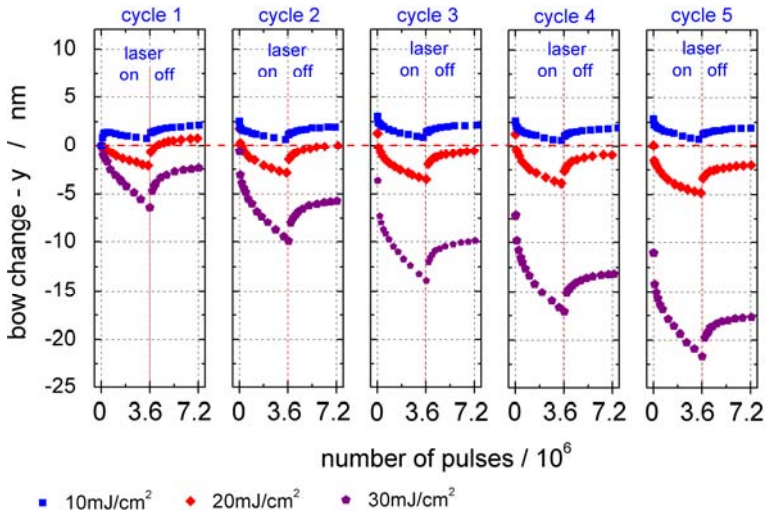

Fig. 87: Bow change and relaxation at high energy levels (≥ 10mJ/cm^2), initially presented on p. 64f.

5.2.2 Bow change as a function of further irradiation parameters

Bow change as a function of the laser repetition rate

The irradiation experiments showed that there is a clear dependency of the bow change from the applied laser repetition rate (see p. 66ff.). At a constant energy level of 10mJ/cm^2 an increasing repetition rate results in an increasing negative bow change. The bow change of -1.5nm at 250Hz is almost doubled at 2kHz. It is assumed that this tendency is originated by the rising mirror temperature, which results in an increasing bimorph effect. Remember the temperature measurements at different repetition rates, where mirrors showed an average temperature rise of 15K at 250Hz and of almost 30K for 2kHz (see p. 80).

However, within the investigated set of parameters, this dependence was just observed along the mirror's tilting axis. How can this be? One reason might be the investigated band width of repetition rates. It is about one order of magnitude and rather small compared to the band width of investigated energy levels. The expectable effect was limited right from the beginning. Another fact is that the temperature driven negative bow change is amplified by the 2-post design along the mirror's tilting axis and the dependence appears clearer.

Bow change as a function of the ambient atmosphere

The irradiation experiments in air and N_2 showed that there was not a fundamental dependency on applied atmosphere. The bow change-x is more or less identical for both cases. The bow change-y (along the tilting axis) is slightly less intense in the case of N_2. But the past exposure relaxation ends up at same values again.

A possible reason for the difference might be the better heat transfer by the N_2 gas flow. During the irradiation in air there was no gas flow at all, which might have increased the mirror temperature slightly.

Bow change as a function of the applied pulse number

The long-term irradiations with up to 250*10^6 pulses brought to light different new aspects compared to the previous rather short-term experiments. There is e.g. the different development of the mirror bow in x and y, which vanishes after a few million pulses (see p. 73). There is indeed the positive bow change at the beginning, which is slightly more intense in x,

but this difference is being evened out within $50*10^6$pulses. After the characteristic turnaround of the bow change development it steadily continues in negative direction until the exposure is stopped. With a rising pulse number the slope flattens slightly, but an end of the development is not in sight. In this connection it turns out, that for the high energy levels the primary positive development has actually no relevance in the long run.

Furthermore it is noticed, that temperature rise and fall as the physical mechanism behind the negative bow change can just be a driving force within the first minutes after the laser is turned on or off. After some minutes, when the mirrors and underlying layers should have reached thermal equilibrium, other mechanisms must be considered as the physical mechanism.

5.3 Physical mechanism for a particular bow change

The following section discusses possible physical mechanisms which might cause the observed bow change in the one or other direction.

5.3.1 Positive bow change

Hypothesis

When a group of mirrors is irradiated for the first time they run through a unique conditioning process and cause the typical permanently positive bow change.

Discussion of different approaches

- Removal of (organic) contamination
- Microstructural changes in the mirror material (e.g. grain growth, recrystallization, phase transition or segregation of alloying components)
- Oxidation

Optical surfaces and MEMS surfaces are often contaminated with organic residuals. The exposure with UV laser light can include the removal of such residuals. There are even publications about surface cleaning based on an UV exposure [74]. However in case of the current MEMS mirrors a significant contamination with organic residuals is not expected. The devices pass a final oxygen plasma for the controlled removal of remaining photoresist. From this it is not assumed that there is a laser induced cleaning process ongoing that might cause the observed permanent change of the mirror bow.

Another approach to corroborate the hypothesis is that the first deposited dose of $5*10^3 J/cm^2$ causes different microstructural changes in the mirror material (e.g. grain growth, recrystallization, phase transition or segregations of alloying components). Effects like recrystallization, phase transition or segregations have not been observed at the TEM analyses (see p. 95ff.). But the AFM analysis has detected a slight laser induced change of the grain size (see. p. 89). However this change was directional and showed a decrease along the x-axis and an increase along the y-axis. But the positive bow change occurs in both mirror direction, albeit with a

different intensity. Nevertheless it is not assumed that the directional variation of the grain size is the reason.

The final approach is the laser induced formation of an additional oxide layer on top of the upper mirror surface. The TEM analyses has shown such a formation of a 20nm oxide layer only for the upper mirror surface (see p. 99). The oxidation seems to be the most likely reason. It is assumed that the grown oxide layer exhibits a stress level which causes the typical positive bow change (fig. 88 below).

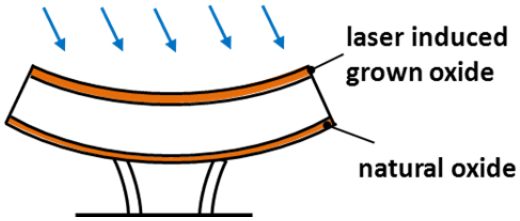

Fig. 88: Formation of the laser induced oxide layer on top causing the positive bow change

How does this assumption agrees to the irradiation experiments which were comparing the laser induced bow change in air and in N_2 atmosphere? There it was observed that the primary positive bow change (in x) was slightly decreased in air (see p. 71f.). The observed differences between the irradiation in air and in N_2 were in general rather small. The remaining portion of O_2 ($\leq$ 1%) in the N_2-atmosphere is in all likelihood orders of magnitudes too high to see significant results coming from the absence of O_2. But much more important is the fact that these air/ N_2-experiemnts were carried out at 10mJ/cm^2 and hence belong to the high energy level. But the positive bow change is observed most distinctive at the low energy levels (see p. 58f. or fig. 89b below) Generally the positive bow change is also observed at higher energy levels, but there it is superimposed by the tendency of the temperature driven negative bow change. Hence the observed behaviour at the air/ N_2 experiments does not exclude the grown oxide layer as the responsible mechanism.

In [64] the thermal oxidation of Al alloys is discussed including the oxidation dynamic at different temperatures. Such an oxidation rate versus time curve typically shows a logarithmic increase at the very beginning and becomes linear later on, see fig. 89a. A similar dynamic is also found at the curves in fig. 89b which describe the bow change at the lower energy levels during the first million pulses.

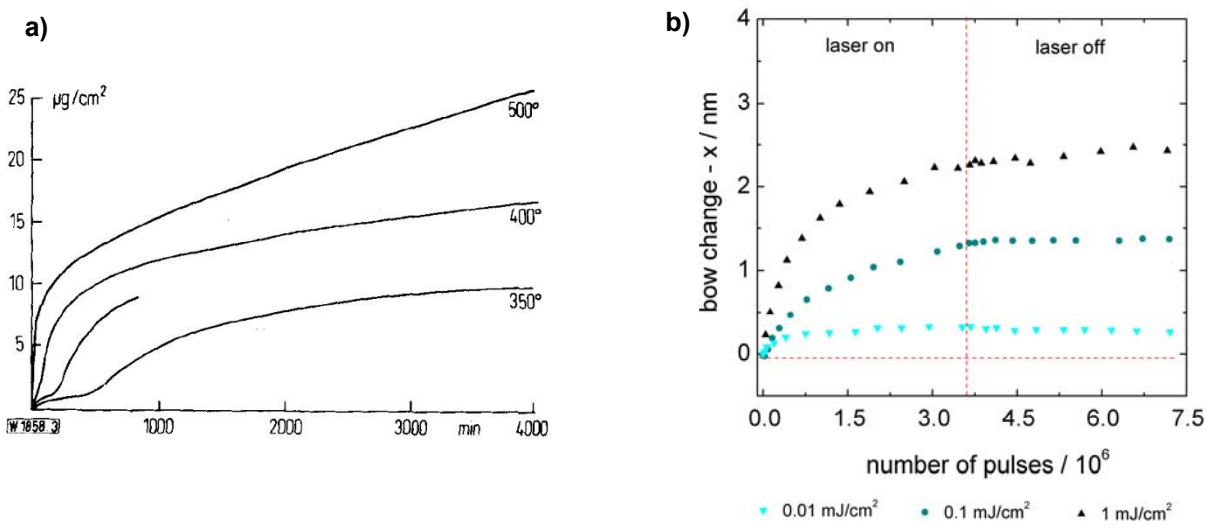

Fig. 89: a) Thermal oxidation of Al alloys in oxygen at different temperatures showing the weight time curve [64], b) detected bow change at lower energy levels during the first million pulses (initially presented on p. 58)

Finally it needs to be mentioned that thermal oxidation of aluminium and various Al-alloys is widely discussed in the literature. But papers about laser induced oxidation are rare, especially when it is about the particular oxidation mechanism.

5.3.2 Negative bow change

The following chapter discusses in detail the negative bow change and possible mechanisms behind it.

Hypothesis

The negative bow change, which is only observed at the so called high energy densities (>1mJ/cm^2), is a temperature driven bimorph effect. In this context bimorph aims at a thermal activation of the detected actuation (a temperature change causes one layer to expand more than the other). The crux is to find a mechanism which causes such a bimorph within a mirror which is actually defined as a single-layer.

Discussion

As described in chapter 3.4, the mirror temperature rises significantly when the SLM is irradiated at energy densities above 1mJ/cm^2 (see p.77 and 82). For this reason a correlation between the increased mirror temperature and the negative bow change, which is only observed at the high energy levels, is very obvious.

The hypothesis is furthermore leaned on different observations:

- The higher the applied energy density the higher the resulting mirror temperature (see p. 77 and p. 82).
- The higher the laser repetition rate the higher the resulting negative bow change and average mirror temperature (see p. 66ff. and p. 80).
- When an irradiation in the high energy density regime is stopped, the mirrors (partially) relax and bend towards their initial shape (see. p. 63f.).
- Back side heating of the SLM (only thermally) causes a negative bow change along the y-axis, which is completely reversible when the SLM is cooled down (see p. 85).

Another aspect is the temporally correlation between temperature rise and bow change. Such a correlation is visualised in fig. 90 below. It shows the bow change (blue) and temperature change (red) during and after an irradiation at 10mJ/cm^2 and 1kHz. The rapid bow change during the first pulses goes along with a rapid increase of the mirror temperature. Therefore it

is assumed that during the first pulses, where the mirror temperature rises rapidly, the temperature development is the dominating reason of the negative bow change.

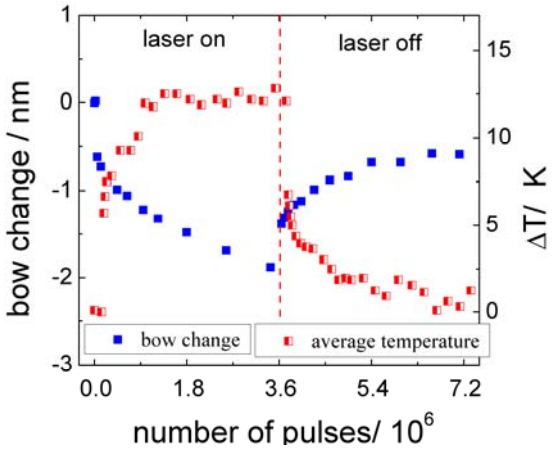

Fig. 90: **Comparison of average mirror temperature and bow change during an irradiation cycle at 10mJ/cm^2 and 1kHz**

But this mechanism cannot be responsible in the long run. When the irradiated mirrors reach thermal equilibrium another mechanism must be responsible for the ongoing bow development.

From this context arise two important questions:

a) What is the source of the bimorph effect in the present case, where the mirror is actually defined as a single-layer?

b) What is the source for the ongoing bow change after the mirrors have reached thermal equilibrium?

Possible mechanisms to cause a bimorph effect

Within the next section different mechanisms are discussed, which theoretically can cause a bimorph in a single-layer mirror (see also fig. 91 below).

- Varying microstructural properties within the upper or lower half of the mirror plate (e.g. grain size) (fig. 91a)
- Varying thickness of the upper and the lower oxide layer (fig. 91b)
- An inhomogeneous distribution of the alloying components (fig 91c)
- A temperature gradient between mirror top and bottom (fig. 91d)

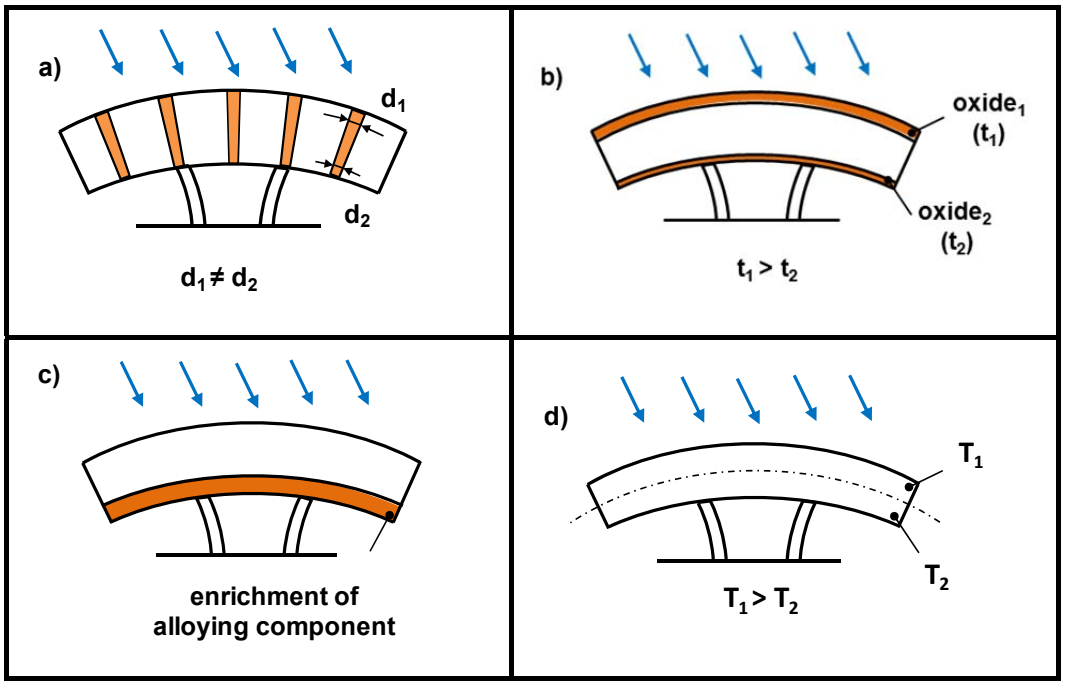

Fig. 91: Possible mechanisms to cause a bimorph effect in case of a single layer mirror: a) varying microstructural properties, b) varying oxide thicknesses, c) local enrichment of alloying components, d) temperature gradient between top and bottom

Bimorph induced by microstructural properties

The first approach is that varying microstructural properties within the upper and lower half of the mirror plate would induce a bimorph system (fig. 91a). Here the focus is set on the size and arrangement of the crystallites or grains respectively which might induce a varying coefficient of expansion in both halves of the mirror plate.

The result of the TEM analyses was that non-irradiated as well as irradiated samples showed columnar crystals and a rather uniform grain growth. Within the first 100nm above the nucleation zone there is a zone of growing grain size until the dominating grains reach the final thickness. Above the nucleation zone the grain size remains more or less constant (see p. 95f.). The AFM analysis has shown that there is a slight bidirectional change in the grain size. But this change does not affect the homogeneous columnar arrangement of the grains.

Apart from the nucleation zone within the first 100nm of the mirror layer there is no sign for a serious effect which might create a bimorph.

Bimorph induced by grown oxide layer on mirror top

The second approach considers the different thickness of upper and lower oxide layer (fig. 91b). The TEM analysis has shown a laser induced oxide layer on top of the mirror of about

20nm. Such a rise was definitely not observed for the lower oxide layer (see p. 99). The idea is that the laser induced heating of the stack (Al_xO_y/ Al-x-Si/ Al_xO_y) causes a bimorph due to the mismatch in the thermal expansion of both oxide layers. Table 20 below shows coefficients of expansion for different materials. The coefficient of expansion of Al_2O_3 is about three times smaller than of Al. When a mirror with a thicker oxide layer on top is heated it should not bend negatively (convex). One rather expects the opposite direction. Consequently the present mismatch in layer thickness (with a thicker top layer) should not be responsible for the negative bow change.

However it has to be mentioned that the numbers from table 20 assume the specific material as bulk. They do not consider any microstructural properties like differing properties of thin films or numerous pores within the layer. The real coefficient of expansion of the grown oxide layer is not exactly known.

material	**coefficient of expansion at 25°C/ (10^{-6}m*m^{-1}*K^{-1})**
Al_2O_3	8
Al	23,8
Si	2.6

Table 20: Thermal coefficients of expansion of different materials and alloys [65], [75]

Bimorph induced by inhomogeneous distribution of alloying components

The next approach discusses an inhomogeneous distribution of the alloying components within the mirror plate (fig. 91c). The mirror plate consists of a sputtered layer of an Al alloy (Al-x-Si). Investigations with TEM-EDX and REM_EDX have detected that the mirrors show an enrichment of Si close to the lower boundary surface (see p.103f.). The enrichment has already been observed before the exposure and a laser driven enhancement could not have been demonstrated. But nevertheless, an effect on the temperature driven bow change seems to be possible. Fig. 92 below depicts the coefficient of expansion of an Al-Si alloy (at 20°C - 100°C) as a function of the amount of Si. From this results a linear dependence of the materials expansion coefficient from the amount of Si. Also consider table 20 above. Si shows an expansion coefficient ten times smaller than Al. Therefore the formation of a bimorph with

the correct sign (bigger expansion of the top layer), coming from the Si enrichment within the lower half of the mirror, seems to be obvious.

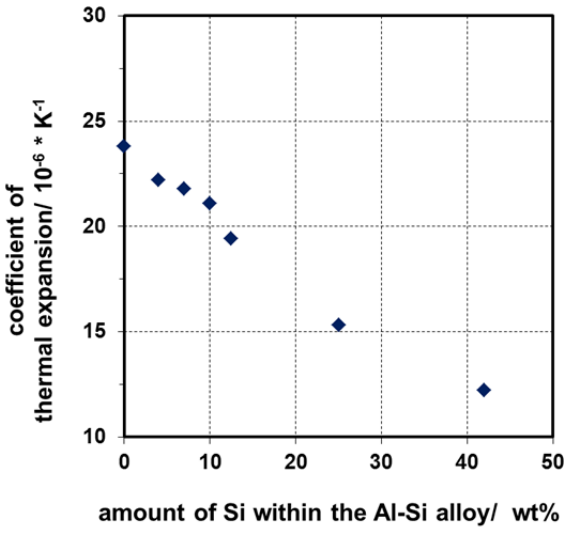

Fig. 92: Thermal coefficient of expansion for an Al-Si alloy as a function of Si [75]

Bimorph induced by a thermal gradient between mirror top and bottom

The last approach discusses a temperature gradient between mirror top and bottom inducing a bimorph effect. In a single layer material such a gradient (with the top hotter than the bottom) could cause the observed negative bow change, see fig. 91d. A thermal gradient between two sides of a thermal conductor (mirror top and bottom) depends amongst others on the applied heat flow and the thermal resistance of the specific heat guiding element (see equ. 19 below).

$$\Delta T = R_{th} * \Phi \qquad (19) \quad [65] \qquad\qquad R_{th} = \frac{l}{\lambda * A} \qquad (19\text{-}1) \quad [65]$$

ΔT = temperature gradient between upper and lower mirror surface, Φ = heat flow, R_{th} = thermal resistance, l = mirror thickness, A = cross section of a mirror, λ = thermal conductivity

But before this equation can be applied it has to be decided about the modulus of the heat introduction.

- Constant heat flow -> consideration of the cw-equivalent of the pulsed laser
- Peak flow -> consideration of the laser's peak power

First a constant heat flow induced by the cw-equivalent of the pulsed laser is assumed. With equ. 19 and 19-1 and the input parameters from table 21:

-> the thermal resistance of a single mirror plate = $13.3\ \frac{K}{W}$

-> the heat flow/ mirror = $4.8 * 10^{-6}$W

-> the resulting permanent temperature gradient = $6.4 * 10^{-5}$K.

h	mirror thickness	700nm
λ (Al, bulk)	thermal conductivity	$220\ \frac{W}{m*K}$
A_{th}	mirror cross section	$2.4*10^{-10}m^2$
E	laser energy density	$10mJ/cm^2$
f	laser repetition rate	1kHz
A	mirror absorption	0.2

Table 21: Determination of the thermal gradient during the irradiation

The resulting mirror curvature is determined with the approach of Mehner [18][17], which discusses the curling of a two layer cantilever beam during a temperature change. But in our case the different expansion from upper and lower half of the plate is originated by a thermal gradient instead of different thermal expansion coefficients. The resulting mirror curvature as a function on the thermal gradient between upper and lower half of the mirror is determined with equ. 20.

$$\boldsymbol{K = (\varepsilon_u - \varepsilon_l) * \frac{3}{4\,t}} \qquad \textbf{(20)} \quad \textbf{[18]}$$

with $\varepsilon_u = \alpha * T_u \; and \; \varepsilon_l = \alpha * T_l$ **(20-1)**

$$\boldsymbol{b = 2 * r * sin^2\left(\frac{x * 45°}{\pi * r}\right)} \qquad \textbf{(21)}$$

with $r = \frac{1}{K}$ **(21-1)**

[17] [18 – p. 115]

K = mirror curvature, ε_i = lateral strain, T_u, T_l = temperature of upper and lower mirror section, t = half mirror thickness, b = mirror bow, r = radius of curvature, x = mirror size

Applying the expansion coefficient of bulk aluminium (table 20) and the permanent temperature gradient from above,

-> resulting mirror curvature = $1.5*10^{-3}\frac{1}{m}$

-> resulting mirror bow equals = $4.8*10^{-14}$m (see equ. 21)

The resulting mirror bow is orders of magnitude smaller than the resolution limit of the used interferometer. Hence the approach that considers a constant heat flow (cw-equivalent of the laser power) causing an adequate thermal gradient between mirror top and bottom cannot be correct.

Determination of a thermal gradient by considering the laser peak power

Since the approach of the constant heat flow was without a result now the effect of single pulses and the lasers peak power is considered. The assumption is that due to the pulsed irradiation the mirror does not show a static temperature level at all. With each pulse the mirror temperature rises and drops significantly. Fig. 93 below illustrates clearly the different temperature conditions when average and peak temperature are compared with each other at same irradiation conditions. Please note that the time scale is microseconds in the one case (blue) and seconds in the other case (red). Note that both curves were detected during different measurements and do not have any temporally link to each other.

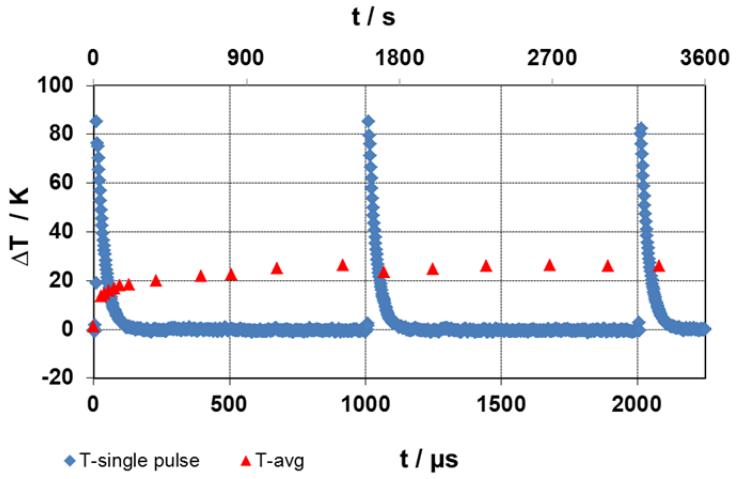

Fig. 93: Comparison of the peak and average mirror temperature rise at 20mJ/cm² and 1000Hz in different time scales

While an irradiation at 20mJ/cm^2 and 1kHz results in a rise of the peak temperature about 85K, the average mirror temperature just rises about 22K. The consequence from this assumption would be that there is no static or constant bending of the mirror plate at all. It rather indicates that the mirror oscillates with the laser repetition rate.

Now since the effect of single pulses shall be considered, there are two mechanisms that induce a thermal gradient between mirror top and bottom and result in a bimorph.

- Thermal resistance and heat flow (equ. 19 and 19-1)
- Propagation time of the heat wave through the mirror

For the consideration of a thermal gradient coming from the mirror's thermal resistance, a constant heat flow during the laser pulse is assumed. Other irradiation conditions are the same as during the "cw-equivalent heat flow approach" (see table 21 above). The resulting quantities are as follows:

-> heat flow/ mirror / pulse	= 0.3W	
-> thermal resistance of the mirror	= 13.3 $\frac{K}{W}$	**(equ. 19-1)**
-> resulting thermal gradient during the pulse	= 4K	**(equ. 19)**
-> resulting radius of curvature	= -5.7mm	**(equ. 20, equ. 21-1)**
-> resulting mirror bow	= -5.6nm	**(equ. 21)**

A resulting mirror bow of -6.5nm at an assumed energy density of 10mJ/cm^2 is in the same order of magnitude than detected values during the experiments and seems to be a realistic number, see p. 63f..

Thermal gradient coming from the heat wave propagation time

The second mechanism which possibly induces a thermal gradient between mirror top and bottom in the single pulse domain is the heat wave propagation time through the mirror. A propagating heat wave in a solid resembles a propagating compression or sound wave. The maximum propagation speed is the speed of sound in a particular material, which is about $6400\frac{m}{s}$ at 20°C for a longitudinal wave in rolled aluminium [66]. Nevertheless the speed of sound is just the theoretical minimum for coherent wave propagation. A significant energy transport happens at lower speed. Equ. 22 gives the propagation length of a heat wave during a certain time span [39][18].

$$l_{th} = \sqrt{\kappa_{th}\,\tau_p} \qquad \textbf{(22)} \qquad \textbf{[39]}^{19}$$

l_{th}= propagation length, κ_{th}= thermal diffusivity, τ_p = laser pulse width

h	mirror thickness	750nm
κ_{th}	thermal diffusivity	$9.5*10^{-5}\ \frac{m^2}{s}$
τ_p	laser pulse length	16ns

Table 22: Input parameters for determination of thermal gradient at laser peak power

With the input parameters from table 22 and assuming a homogeneous intensity distribution within the pulse, the propagation length of the heat wave during the time span of a single laser pulse equals 1.2µm From this the propagation time through a mirror of 750nm is estimated to be in the order of 10ns.

From propagation time to the resulting thermal gradient

There is not a direct link between the estimated propagation time of the heat wave and the resulting thermal gradient. Assuming a homogeneous heat input, the propagation along z can be described as a one dimensional process with z = f(t), showing an exponential decay. The exact knowledge of the temporally development is not necessary. For a rough estimation we just consider the moment were the heat wave passed half the mirror thickness. Since the propagation time is determined with 10ns, the half way moment should be passed within a few

[18] [39 – p.42]
[19] [39 – p.42]

nanoseconds. The pulse resolved temperature measurements have shown a temperature rise of 45K following a 10mJ/cm^2 pulse (see p.82). According to this value the thermal gradient at the half way moment between upper and lower half of the mirror is 2*45K. But the assumption of 90K as the thermal gradient may also be not correct. At such short time scales of a few nanoseconds, the eigenfrequency of the mirror plate and the coupling efficiency into the oscillating system need to be considered as well.

For this purpose the eigenfrequency of an oscillating mirror plate (at its fundamental mode) is estimated. Two approaches were applied to get a simplified model of the mirror:

a) mirror replaced by a free-standing plate (see equ.. 23, 23-1)
b) mirror half replaced by a cantilever (see equ. 24)

$$f_{m,n} = \frac{\omega_{m,n}}{2\pi} = \frac{\pi}{2} * \left[\left(\frac{m}{a}\right)^2 + \left(\frac{n}{b}\right)^2\right] * \sqrt{\frac{B}{\rho * h}} \qquad \textbf{(23)} \quad \textbf{[67]}$$

with $$B = \frac{E * h^3}{12 * (1-\mu^2)} \qquad \textbf{(23-1)}$$

$f_{m,n}$ = eigenfrequency of the free-standing oscillating plate, B = bending stiffness for an undamped plate

$$\varpi_k = k^2 \pi^2 \sqrt{\frac{E * I}{\rho * A * L^4}} \quad \textbf{with } k = 1, 2 \ldots \textbf{(24)} \qquad I = \frac{b * h^3}{12} \qquad \textbf{(24-1)} \quad \textbf{[76]}$$

ω_k = eigen angular frequency of the cantilever, k = eigenfunction (mode), E = Young's modulus, I = area moment of inertia, ρ = density, A = cross section, L = length of the cantilever = half mirror edge length

Depending on the applied approach (oscillating plate or cantilever) the resulting eigenfrequency at its fundamental mode is between 5MHz and 15MHz. The results arise from equ. 23, 24 and by the input parameters in table 23 below. The inverse of the eigenfrequency $\frac{1}{f}$ is between 65ns and 200ns, which is about an order of magnitude higher than the estimated heat wave propagation time and the laser pulse width (p.124).

m	eigenfunction/ mode in x	1	
n	eigenfunction/ mode in y	1	
a	edge length in x	15.5	[µm]
b	edge length in y	15.5	[µm]
h	plate height	750	[nm]
ρ	material density	2700	[kg/m^3]
E	Young's modulus - Al	7 *10^{10}	[N/m^2]
µ	Poisson's number - Al	0.34	

Table 23: Mirror dimensions and material constants of aluminium

An exact estimation about the coupling efficiency (excitation of the mirror plate to oscillate by a short-term thermal gradient) can just be done by a simulation of the a actuator/ driving force-system. But according to the determined magnitude of the mirror eigenfrequency it is assumed that the majority of the propulsion (short-term thermal gradient) is coupled into the mirror plate and contributes to the excitation (bowing). As a consequence a thermal gradient between mirror top and bottom is assumed to be present for a few nanoseconds. Off course the assumption of a particular thermal gradient is actually not valid. Since the thermal gradient (coming from the heat wave propagation) is not a static situation but a function of time. But nevertheless for an estimation of the order of magnitude of the resulting bow change such an assumption is helpful.

-> assumed thermal gradient during the pulse = 90K
-> resulting radius of curvature = -0.23mm **(equ. 20, equ. 21-1)**
-> resulting mirror bow = -129nm **(equ. 21)**

A bow change of -120nm at an assumed energy density of 10mJ/cm^2 is more than an order of magnitude larger than the measured values. Nevertheless the final discussion of the oscillating mirror model on the following page will show that such a magnitude agrees with the model.

Conclusion to physical mechanisms inducing a bimorph

The last chapter was discussing different mechanisms which might cause a bimorph (as the driving force for the negative bow change) in a single-layer mirror. The first approach was

about varying microstructural properties within the upper and lower half of the mirror plate. Apart from the nucleation zone within the first 100nm of the mirror layer there is no sign for a serious effect which might create a bimorph.

The second approach was about the different thickness of upper and lower oxide layer. From the TEM analysis it is known that the mirror top shows a laser induced oxide layer about 20nm. But when an aluminium mirror with a thicker oxide layer on top is heated it should not bend negatively (convex). Depending on the coefficient of expansion of Al and Al_2O_3 one rather expects the opposite direction. Consequently the present mismatch in layer thickness (with a thicker top layer) should not be responsible for the negative bow change.

The next approach discussed an inhomogeneous distribution of the alloying components within the mirror plate. From TEM-EDX and REM-EDX it is known that the mirrors show an enrichment of Si close to the lower boundary surface. Due to the difference in the expansion coefficients of Al and Si the formation of a bimorph with the correct sign (bigger expansion of the top layer), seems to be obvious.

The last approach was about a temperature gradient between mirror top and bottom inducing a bimorph effect. In a first attempt the cw-equivalent of the (pulsed) laser power was applied. But this approach resulted in a bow change orders of magnitude smaller than the resolution limit of the interferometer. In a second attempt the laser peak power was considered. This approach considered a thermal gradient mostly coming from the heat wave propagation time (≈10ns) through the mirror. It was shown that a negative bow change in the range of -129nm could be arisen. However such a value would be more than a magnitude above the measured values at given energy level. Nevertheless the final discussion of the oscillating mirror model (following page) will show that such a magnitude agrees with author's idea of real bow changing during pulsed irradiation.

Conclusion to the negative bow change

The aim of the previous chapter was the detailed discussion of the negative bow change and possible mechanisms behind it. The argumentation started with the hypothesis that the negative bow change is a temperature driven bimorph effect. Two mechanisms were found which are assumed to induce a bimorph in a single-layer mirror. The first mechanism was a Si enrichment close to the lower boundary surface of the mirror. A serious quantification of the resulting bow change was not possible in this case.

The second mechanism was a thermal gradient between mirror top and bottom. In a first attempt the cw-equivalent of the (pulsed) laser power was applied. But this approach was without a result. It turned out that a serious discussion of laser induced temperature rise and negative bowing requires the consideration of single laser pulses and the laser peak power. In the single pulse regime a thermal gradient, which appears during the heat wave propagation through the mirror plate, seems to be the most significant propulsion of the negative bow change.

However the approach of the varying mirror temperature includes the consequence that the mirror bow is varying (oscillating) as well. Consequently it is assumed that during an irradiation at high energy densities, the mirror bow oscillates with the laser repetition rate. The "oscillating mirror model" includes certain consequences. The presence of the thermal gradient is limited to a few nanoseconds during and following the pulse. This results in a duty cycle in the range of $1*10^{-5}$ at a laser repetition rate of 1kHz. On the other hand there is the procedure of data acquisition (single data point of the bow curve), which lasts several hundred milliseconds. From this arises a very important fact. The obtained interferometric data do not show the real bow change but the mean of the bow development during a series of several hundred laser pulses.

The peak of the "real bow change" is unknown. The estimation in the last section resulted in the range of about -130nm at an energy level of $10mJ/cm^2$. The measurements at the same energy level detected an accumulating bow change of a few nanometer within a duration of several million pulses. A comparison of both regimes is difficult. In the one case we are talking about a single pulse effect in the other case we are talking about an accumulating effect. But nevertheless the difference the order of both quantities supports the hypothesis of the oscillating mirror bow.

Finally it has to be emphasized that the link between the presence of the assumed thermal gradient and the course of the detected negative bow change is not settled conclusively. A mirror that would behave like an ideally elastic solid should relax immediately when the pro-

pulsion (thermal gradient) has vanished. In such a case the real mirror bowing would also occur just for a few nanoseconds. But it is rather likely that bowing and relaxation occurs with a certain delay. Generally it is assumed that anelastic (delayed elastic deformation) and creep (delayed plastic deformation) contribute to the observed bow change. Otherwise an ongoing bow change and relaxation procedure which last hours or longer cannot be explained.

6 Summary

Design of the measuring station

The first part of the thesis was the design of an appropriate measuring station. The fundamental requirements on the measuring principle were the in situ characterisation of the micro mirror topography with a resolution in the single digit nanometre regime during a laser exposure. After the evaluation of different measuring principles a measuring station was designed, which combines a phase-shift interferometer, an optical microscope and the laser irradiation at 248nm. Finally the interferometer performance and measurement error were characterized in detail.

Bow change as a function of the laser pulse energy

The effect of varying pulse energies on the mirror bow change was investigated in a wide range of 10^{-5}J/cm^2 to 10^{-2}J/cm^2. A general conclusion is that minimum pulse energy of 10^{-5}J/cm^2 at a repetition rate of 1kHz is required to detect any laser induced change in the mirror curvature. Such a bow change can occurs in positive as well as in negative direction. The parameters which dominate the direction are the laser pulse energy and the deposited energy. In principle two characteristic behaviours can be distinguished:

- Positive bow change at pulse energies up to 10^{-3}J/cm^2 (at 1kHz) or a deposited energy of 10^4J/cm^2
- Negative bow change at pulse energies larger than 10^{-3}J/cm^2 (at 1kHz)

An irradiation at pulse energies up to 10^{-3}J/cm^2 (at 1kHz) results in a permanent bow change in the range of λ/ 100 in positive direction. Such a positive bow change accumulates within a deposited energy of $5*10^3$J/cm^2 and does not show any relaxation. It is even ongoing for a certain time after the irradiation is stopped. At pulse energies larger than 10^{-3}J/cm^2 the positive bow change was observed as well until a deposited energy of about 10^4J/cm^2. Then the bow development turned around and was changing in opposite (negative) direction until the irradiation was stopped. It is assumed that the positive bow arises from the growth of an additional oxide layer on top of the upper mirror surface. The formation of a 20nm oxide layer was detected with TEM analysis and identified only for the upper mirror surface. It is assumed that the grown oxide layer exhibits a stress level which causes the typical positive bow change.

An irradiation at pulse energies larger than 10^{-3}J/cm^2 causes a negative bow change which accumulates to λ/ 10 within some ten million laser pulses. The detected bow change rises with the applied energy level and the applied pulse number. Even during a long-term irradiation of 250*10^6 pulses there was no end of the bowing conceivable. When the irradiation is stopped the former bow change partially relaxes towards the initial value. The relaxation happens rapidly at the beginning and then slows down. It was shown that relaxation is ongoing for several hours or even days. Regarding the mechanism behind the negative bow change the hypothesis was proposed that it would arise from a temperature driven bimorph effect within the mirror plate. Several facts which support this assumption were listed on p. 116. Resulting from the degradation analysis two mechanisms were found which theoretically could induce a relevant bimorph in a single-layer mirror. The first mechanism was a Si enrichment close to the lower boundary surface of the mirror. The second mechanism was a thermal gradient between mirror top and bottom, which mostly appears during the laser induced heat wave propagation through the mirror plate. The thermal gradient is assumed to be the more significant propulsion for the observed bow change. However the approach of the varying mirror temperature includes the consequence that the mirror bow is varying (oscillating) as well. Consequently it is assumed that during an irradiation at pulse energies larger than 10^{-3}J/cm^2 the mirror bow oscillates with the laser repetition rate. The "oscillating mirror model" includes certain consequences. The presence of the thermal gradient should be limited to a few nanoseconds during and following a single pulse. On the other hand there is the procedure of the interferometric data acquisition, which lasts several hundred milliseconds. From this arises a very important fact. Assuming the model is correct, the obtained interferometric data do not show the real bow change but the mean of the bow during a series of several hundred laser pulses. Hence the peak of the "real bow change" following a single pulse is more or less unknown. But a rough estimation in the discussions section resulted in an order of -130nm following a pulse of 10mJ/cm^2.

Finally it has to be emphasized that the link between the presence of the assumed thermal gradient and the course of the detected negative bow change is not settled conclusively. A mirror that would behave like an ideally elastic solid should relax immediately when the propulsion (thermal gradient) has vanished. In such a case the real mirror bowing would also occur just for a few nanoseconds. But it is rather likely that the negative bow change and relaxation occurs with a certain delay. Generally it is assumed that anelastic (delayed elastic deformation) and creep (delayed plastic deformation) also contribute to the observed bow

change. Otherwise an ongoing negative bow change and relaxation procedure which last hours or longer cannot be explained.

Bow change as a function of further irradiation parameters

The irradiation experiments with varying laser repetition rates have also shown an obvious effect on the bow change. At a constant energy level of 10mJ/cm^2 an increasing repetition rate causes an increasing negative bow change. The detected bow change at 250Hz (accumulated within 3.6*10^6 pulses) was almost doubled at 2kHz. It is assumed that this tendency is originated by the rising mirror temperature, which results in an increasing bimorph effect. This assumption is supported by temperature measurements, which showed a rise of the average mirror temperature of 15K at 250Hz and of 30K at 2kHz. However, within the investigated set of parameters, this dependence was only observed along the mirror's tilting axis. But from former irradiation test it is known that the mirror's 2-post design typically causes a bigger negative bow change along the tilting axis at pulse energies larger 1mJ/cm^2.

The irradiation tests in air and N_2 atmosphere did not result in a significant difference in the detected bow change. The bow change-x is more or less identical for both cases. The bow change-y was slightly bigger in air.

Measurement of mirror temperature during a laser irradiation

The measurement of the average mirror temperature has shown an obvious dependence on the applied laser pulse energy and repetition rate. An irradiation at 5mJ/cm^2 resulted in a rise of 5K, at 30mJ/cm^2 of 40K. But the time constant of the detected temperature rise seemed to be unusually. Depending on the applied energy level, the temperature rise was ongoing up to several minutes. It is assumed that the heating of the underlying layers occurs slower due to the thermal resistance between mirror and substrate plane. The variation of the repetition rate resulted in a rise of the mirror temperature of 15K at 250Hz and of 30K at 2kHz.

The pulse-resolved temperature measurements have shown that the temperature rise following a single pulse happens within some hundred nanoseconds and amounts to values many times higher than the detected average temperature rise. A pulse of 30mJ/cm^2 caused peak of 120K compared to the detected average rise of 40K. The temperature decrease also happens very quickly with a falling time below 30µs. The difference between both quantities (peak vs. average) makes it difficult to estimate the mirror performance during a laser irradiation. In the

discussion section it was demonstrated that the simplified assumption of an average mirror temperature cannot explain the detected negative bow change at pulse energies in the mJ/cm^2 regime.

Laser induced material degradation

Another aspect of the thesis was the analysis of laser induced material degradation. For this purpose samples were analysed by means of different devices and analytical techniques. The analysis of irradiated mirrors with AFM has detected a slight increase of the mirror roughness. Detected values of Rq and Ra showed an increase of 10%, detected Rmax values of 20%. The AFM measurements additionally detected a slight variation of the mirror grain size. The grains have changed their size directional and showed a decrease of 10% along the x-axis and an increase of 10% along the y-axis (tilting axis). This result agrees in turn with the observation that the bow change is bigger along the mirror's tilting axis at higher energy levels. The rising grain size might be a consequence of this.

The analysis of irradiated samples using reflectometry detected a loss of reflectance for wavelengths smaller 245nm. The loss was about 15% at 200nm, which was the lower end of the investigated spectral bandwidth. At 248nm (irradiating wavelength) the reflectance remained more or less unchanged.

Analysis of the mirror with TEM

Two irradiated and two reference mirrors were investigated with TEM. The focus was set on the mirror grains (size, arrangement, shape), the mirror boundary layer and the distribution of the alloying components.

The irradiation seemed not to have changed the structure or size of the metallic grains dramatically. Reference and irradiated samples showed equally arranged columnar crystals with a diameter of about 50nm ± 20nm and a uniform grain growth. The grains of the irradiated samples appeared somewhat smaller, which would agree to the results from the AFM analysis. However a serious statistical analysis could not have been obtained from the TEM pictures.

The non-irradiated samples showed an amorphous boundary layer with a thickness of a few nanometres (≈5nm). Apart from possible effects by the sample preparation, this layer might represent the naturally grown oxide. After the irradiation the thickness of the upper boundary layer has risen to 15nm-20nm. Such a significant growth was not observed at the lower

boundary layer. Another irradiation induced effect is the numerous formation of pores and crystalline inclusions within the grown boundary layer. Again this effect was only observed at the upper layer.

Finally EDX analysis was used for a local identification of elements within the lamella. A comparing EDX analysis of upper boundary layer and the crystalline mirror material resulted in the identification of the grown boundary layer as aluminium oxide. Within the crystalline material the aluminium peak overshadows the entire EDX signal. Obvious peaks of the alloying components were not resolved. The EDX analysis of different zones within the crystalline material detected a higher concentration of Si close to the lower mirror surface. Another REM-EDX analysis of a non-irradiated mirror has reproduced this result and showed that this inhomogeneity of the Si distribution is not an irradiation induced effect.

7 Outlook

Time resolved interferometry

The discussion has ended with the assumption that the mirrors would undergo an oscillating bow change following each single laser pulse. But this assumption could finally not have been proven yet. For a deeper understanding of the circumstances the implementation of an interferometric setup that allows the bow detection on a millisecond time scale would be necessary. Hence the real bow change between single laser pulses could be characterized. Such a measurement could in principle be realized either with a very quick detector or just with a stroboscopic illumination.

Optimization of the mirror design for „high“ energy level applications

All samples which were irradiated during this thesis have never been designed for such intense demands. Especially the applied energy level was orders of magnitudes higher than the initially intended application. SLMs which are used for real applications in the regime of some mJ/cm^2 should be optimized for such an energy level. The selection of an irradiation robust material and the modification of the mirror thickness are possible regulating screws. Fig. 94 below shows a mirror design where first optimization approaches have been implemented (red) in comparison to the used “standard” mirrors (blue).

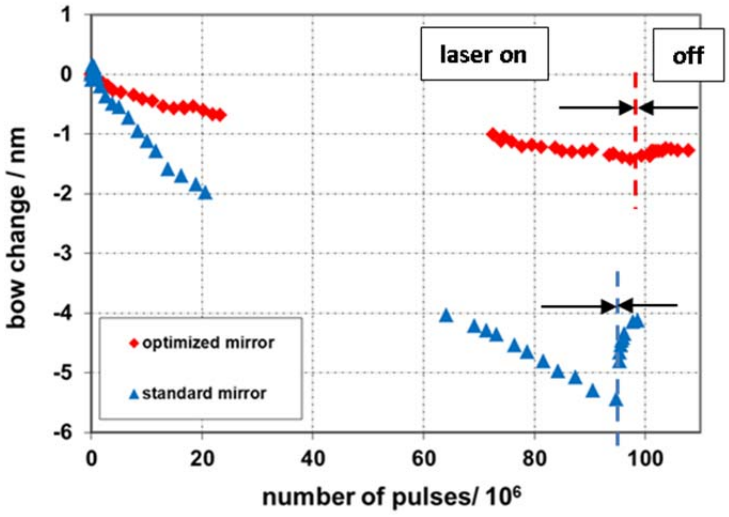

Fig. 94: Comparison of a “standard” mirror (blue) and a mirror design including first optimizations for the “high” energy regime (red)

Both samples were irradiated at 10mJ/cm^2 and about 100 * 10^6 pulses. The resulting bow change of the standard mirror is several times bigger than of the optimized one. The enhancement of the mirror design was not part of the present thesis.

References

[1] Motamedi, M. E.: “MOEMS” Bellingham : SPIE, (2005)

[2] Lakner, H. et al.: ”Design and Fabrication of Micromirror Arrays for UV- Lithography”, In: MOEMS and Miniaturized Systems II, Proc. of SPIE Vol. 4561, (2001)

[3] Dauderstädt, U. et al.:“ Advances in SLM Development for Microlithography”, In: MOEMS and Miniaturized Systems VIII, Proc. of SPIE Vol. 7208, (2009)

[4] Krellmann, Mathias et al.: „Bending of Aluminum Alloy Beams depending on Irradiance and Repetition Rate of UV Laser Radiation”, In: Reliability, Packaging, Testing, and Characterization of MEMS/MOEMS V, Proc. of SPIE Vol. 6111, (2006)

[5] Lauria, J et al.: ”SLM device for 193nm lithographic applications”, In: Microelectronic Engineering, Vol. 86 Issue 4-6, (2009)

[6] Schenk, H.: ”Siliziumbasierte mikrooptische Modulatoren”, Cottbus, Brandenburgische Technische Universität, Fakultät für Mathematik, Naturwissenschaften und Informatik, Habilitationsschrift, (2007)

[7] Dudley, D, Duncan, W., Slaughter, J.: “Emerging Digital Micromirror Device (DMD) Applications”, In: MOEMS Display and Imaging Systems, Proceedings of SPIE Vol. 4985, (2003)

[8] Hornbeck, L. J.: „Current Status and Future Applications for DMD^{TM} -Based Projection Displays”, Texas Instruments, White Paper, www.dlp.com, (2007)

[9] TEXAS INSTRUMENTS 2012
URL: http://www.dlp.com/technology/how-dlp-works/default.aspx (2012)

[10] Gehner, A., Wildenhain, M., Lakner, H.:“ Micromirror arrays for wave-front correction”, In: MOEMS and Miniaturized Systems, Proc. of SPIE Vol. 4178, (2000)

[11] Gehner A. et al.: „MEMS analog light processing − an enabling technology for adaptive optical phase control“, In: MEMS/MOEMS Components and Their Applications III, Proc. of SPIE Vol. 6113, (2006)

[12] Schmidt, J.U., Friedrichs, M., Gehner, A..: „Amorphous TiAl films for micromirror arrays with stable analog deflection integrated on complementary metal oxide semiconductors”, In: J. Micro/Nanolith. MEMS MOEMS 7(2), (2008)

[13] Dauderstädt, U. et al.: „Application of Spatial Light Modulators for Microlithography”, In: MOEMS Display and Imaging Systems II, Proc. of SPIE Vol. 5348, (2004)

[14] Wagner, M. et al.: “Hochauflösende Flächenlichtmodulatoren auf Basis von Mikrospiegelmatrizen”, In: MikroSystemTechnik Kongress 2007, Dresden, VDE-Verlag (2007)

[15] Sandstrom, T. et al.: „OML: Optical Maskless Lithography for Economic Design Prototyping and Small-Volume Production“, In: Optical Microlithography XVII, Proc. of SPIE, Vol. 5377, (2004)

[16] Friedrichs, M., Schmidt, J. U., Dürr, P., Bakke, T.: „One Megapixel SLM with high optical fill factor and low creep actuators”, In: Optical MEMS and Their Applications 2006 IEEE/ LEOS, (2006)

[17] Hecht, Eugen: „Optik“. München: Oldenbourg Wissenschaftsverlag GmbH, (2001)

[18] Mehner, Jan: “Entwurf in der Mikrosystemtechnik”, Chemnitz, Technische Universität Chemnitz, Fakultät für Elektrotechnik und Informationstechnik, Habilitation, (1999)

[19] Shea, H. R.: “Radiation sensitivity of microelectromechanical system devices”, In: J. Micro/Nanolith. MEMS MOEMS Vol. 8(3), (2009)

[20] Shea, H. R.: “Effects of Radiation on MEMS”, In: Reliability, Packaging, Testing, and Characterization of MEMS/MOEMS and Nanodevices X, Proc. of SPIE Vol. 7928 (2011)

[21] Hartzell, A., L., da Silva, M.G., Shea, “H.R.: MEMS Reliability” New York : Springer Science + Business Media, (2011)

[22] Xue, X. et al.: “Effects of Laser Irradiation on the Surface Topology of Surface-Micromachined Polysilicon Structures”, In: 2004 SEM International Congress & Exposition on Experimental & Applied Mechanics (2004)

[23] Forest, C. R. et al.: “Static and Dynamic Optical Metrology of Micro-Mirror Thermal Deformation“, In: NSTI-Nanotech: Technical Proceedings, Vol. 2 (2004)

[24] Phinney, L. et al.: “Damage of MEMS Thermal Actuators Heated by Laser Irradiation”, In: Reliability, Packaging, Testing, and Characterization of MEMS/MOEMS IV, Proc. of SPIE Vol. 5716 (2005)

[25] Phinney, L., Blum Spahn, O. and Wong, C. C.: “Experimental and Computational Study on Laser Heating of Surface Micromachined Cantilevers”, In: Reliability, Packaging, Testing, and Characterization of MEMS/MOEMS V, Proc. of SPIE Vol. 6111, (2006)

[26] Phinney, L., Serrano, J.R.: “Influence of target design on the damage threshold for optically powered MEMS thermal actuators”, In: Sensors and Actuators A 134 (2007)

[27] Blum Spahn, O. et al.: „Impact of High Optical Power on Optical MEMS”, In: 2008 IEEE/LEOS International Conference on Optical MEMS and Nanophotonics, (2008)

[28] Serrano, J., Phinney, L. M.: “Effects of layers and vias on continuous-wave laser heating and damage of surface-micromachined structures”, In: J. Micro/Nanolith. MEMS MOEMS 8(4) (2009)

[29] Burns, D.M., Bright, V.M.: ” Optical power induced damage to microelectromechanical mirrors”, In: Sensors and Actuators A 70 (1998)

[30] Agarwal, A. et al.: “Laser Power Monitoring Using MEMS Micromirror Technology”, In: IEEE 37th Annual International Reliability Physics Symposium, San Diego, California, (1999)

[31] Sandner, T. et al.: “Highly reflective coatings for micromechanical mirror arrays operating in the DUV and VUV spectral range”, In: MOEMS Display and Imaging Systems III, Proc. of SPIE Vol. 5721 (2005)

[32] Sandner, T. et al.: „Highly Reflective Thin Film Coatings for High Power Applications of Micro Scanning Mirrors in the NIR-VIS-UV Spectral Region”, In: Advances in Optical Thin Films II, Proc. of SPIE Vol. 5963, (2005)

[33] Mai, A., et al.: “In situ determination of laser induced degradation of micro-mirror arrays”, In: 2011 International Students and Young Scientists Workshop „Photonics and Microsystems” (Cottbus 2011), IEEE (2011)

[34] Dauderstädt, U. et al.: “Charging effects in Spatial Light Modulators based on Micromirrors”, In: Reliability, Packaging, Testing, and Characterization of MEMS/MOEMS VI, Proc. of SPIE Vol. 6463 (2007)

[35] Dauderstädt, U. et al.: „Charging effects in micromirror spatial light modulators”, In: J. Micro/Nanolith. MEMS MOEMS Vol. 7(2), (2008)

[36] Niedrig, H.: „Bergmann • Schaefer Lehrbuch der Experimentalphysik – Band 3 Optik” Berlin : de Gruyter, (1993)

[37] Born, M.: “Optik”, Berlin : Springer Verlag (1985)

[38] Palik, E.: “Handbook of Optical Constants of Solids”, Academic Press (1985)

[39] Prokhorov, A.M.: “Laser Heating of Metals”, Bristol : Adam Hilger imprint (1990)

[40] Leach, R.: “Optical Measurement of Surface Topography”, Heidelberg : Springer-Verlag, (2011)

[41] Creath, K.: “Phase-Measurement Interferometry Techniques”, In: Progress in Optics, 26, (1988)

[42] Carré, P.: “Installation et utilisation du comparateur photoélectrique et interférentiel du Bureau International des Poids et Mesures”, In: Metrologia Vol. 2, No. 1, (1966)

[43] Malacara, D., Servin, M., Malacara, Z.: ”Interferogram analysis for optical testing”, Boca Raton : Taylor & Francis Group, (2005)

[44] Hariharan, P.: “OPTICAL INTERFEROMETRY”, San Diego CA : Academic Press (2003)

[45] Schmit, J., Creath, K.: “Extended averaging technique for derivation of error-compensating algorithms in phase-shifting interferometry”, In: Appl. Opt., Vol. 34, No. 19, (1995)

[46] Norm ISO/FDIS 25178-2 2008. “Geometrical product specification (GPS) – Surface texture: Areal – Part 2: Terms, definitions and surface texture parameters”, (2008)

[47] Norm ISO/DIS 25178-3 2010. “Geometrical product specification (GPS) – Surface texture: Areal – Part 3: Specification operators”, (2010)

[48] Norm ISO 25178-6 2010. “Geometrical product specification (GPS) – Surface texture: Areal – Part 6: Classification of methods for measuring surface texture”, (2010)

[49] Norm ISO/DIS 25178-70 2011. “Geometrical product specification (GPS) – Surface texture: Areal – Part 70: Physical measurement standards”, (2011)

[50] Norm ISO/DIS 25178-603 2010. “Geometrical product specifications (GPS) - Surface texture: Areal - Part 603: Nominal characteristics of noncontact (phase-shifting interferometric microscopy) instruments”, (2010)

[51] Saleh, B.E.A., Teich, M.C.: „Fundamentals of Photonics“, New Jersey : John Wiley & Sons, Inc., (2007)

[52] Haferkorn, Heinz „Optik“, Weinheim : WILEY-VCH Verlag GmbH & Co. KGaA, (2003)

[53] ALLIED Vision Technologies GmbH: “CCD-4000UV – Datasheet“ - URL: http://www.vdsvossk.de/de/index.php (2012-04-17)

[54] Schröder, G., Treiber, H.: „Technische Optik“. Würzburg : VOGEL, (2002)

[55] Hariharan, P.: “Basics of Interferometry”, Burlington, MA : Academic Press, (2007)

[56] Creath, K.: “Phase-measurement interferometry: BEWARE these Errors”, In: Laser interferometry IV, Proc. of SPIE Vol. 1553, (1991)

[57] Norm ISO 25178-601 2010. “Geometrical product specifications (GPS) - Surface texture: Areal - Part 601: Nominal characteristics of contact (stylus) instruments.”, (2010)

[58] Wullinger, I. et al.: “Temperature measurement on MOEMS micromirror plates under illumination“, In: Reliability, Packaging, Testing, and Characterization of MEMS/MOEMS and Nanodevices IX, Proc. of SPIE Vol. 7592, 2010

[59] Innocenzi, M.E.et al.: „Room-temperature optical absorption in undoped α-$A1_2O_3$“, In: J. Appl. Phys. 67, 7542, (1990)

[60] Gianuzzi, L.A., Stevie, F.A.: “A review of focused ion beam milling techniques for TEM specimen preparation”, In: Micron Vol. 30, (1999)

[61] Shukalov, A.S. et al.: “Surface oxidation of dilute Al-Si alloys”, In: Journal of Electron Spectroscopy and Related Phenomena, 62, (1993)

[62] powder diffraction file: entry 46-1212 - aluminium oxide (Al_2O_3)

[63] powder diffraction file: entry 44-0231 – aluminium fluoride (AlF_3)

[64] Grauer, R., Schmoker, P.: „Die Oxidation von Aluminium-Magnesium-Legierungen in Sauerstoff bei erhöhter Temperatur“, In: Werkstoffe und Korrosion, 27. Jahrgang, Heft 11, (1976)

[65] Kuchling, H.: „Taschenbuch der Physik“, München : Fachbuchverlag LEIPZIG im Carl Hanser Verlag, (2001)

[66] Kohlrausch, F.: „Praktische Physik“, B.G. Teubner, Stuttgart, 1996

[67] Dietz, P.; Rolshofen, W.; Schäfer, G.: „Betrachtungen zum Schwingungsverhalten von Rechteckplatten“ Institut für Maschinenwesen, TU-Clausthal, Institutsmitteilung Nr. 32 (2007)

[68] Lee, H. J., Zhang, P., Bravman, J. C.: „Stress relaxation in free-standing aluminum beams“, In: Thin Solid Films 476, (2005)

[69] AI-Nimr, M.A.: “Heat Transfer Mechanisms During Short-Duration Laser Heating of Thin Metal Films”, International Journal of Thermophysics. Vol. 18, No. 5. (1997)

[70] Baehr , H. D., Stephan, K.: “Wärme- und Stoffübertragung“, Springer, (2010)

[71] Hippler, S., Tokovinin, A.: „Adaptive Optik Online “,
URL: http://www.mpia.de/homes/hippler/AOonline/ao_online.html (2013-10-22)

[72] Tyson, R.K.: “Introduction to Adaptive Optics”, SPIE, Bellingham (2000)

[73] Pufe, W.: “ Protokoll REM/EDX-Untersuchung“, IPMS internal report (2013)

[74] Park, Hee K. et al.: “A practical excimer laser-based cleaning tool for removal of surface contaminants”, Components, Packaging, and Manufacturing Technology, Part A, IEEE Transactions, Vol.: 17, Issue: 4, (1994)

[75] Hidnert, P.: “THERMAL EXPANSION OF ALUMINUM AND VARIOUS IMPORTANT ALUMINUM ALLOYS”, Scientific Papers of the Bureau of Standards, Vol. 19, p. 697-731 (1924)

[76] Wandinger, J.: “Elastodynamik 2”, Vorlesungsskript, HAW Landshut (2013)

Acknowledgement

Thanks go to all my colleagues who provided me with essential knowledge in metrology, analytical techniques and material science and had open minds for the frequent discussion of strange mirror effects.

Thanks go to department and group leader who made my thesis possible and provided me with helpful ideas and comments.

Thanks go to Prof. Dieter Schmeißer and Prof. Harald Schenk who have demonstrated general approaches and gave vulnerable comments on form and content.

Special thanks go to René Hübner and his colleagues from Helmholtz – Zentrum Dresden – Rossendorf. He performed the remarkable sample preparation and TEM analysis on different micro mirrors.

Special thanks go to my family and Dana!